Physik-Department

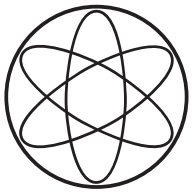

Magnetic Nanoparticles – Characterization and Modeling for Drug Targeting Applications

Dissertation
von

Alexandra Y. Heidsieck

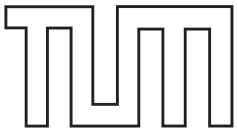

Technische Universität
München

Physik Department

Lehrstuhl für Biophysik E22
und
Zentralinstitut für Medizintechnik

Magnetic Nanoparticles – Characterization and Modeling for Drug Targeting Applications

Alexandra Y. Heidsieck

Vollständiger Abdruck der von der Fakultät für Physik der Technischen Universität München zur Erlangung des akademischen Grades eines

Doktors der Naturwissenschaften (Dr. rer. nat.)

genehmigten Dissertation.

Vorsitzender:		Univ.-Prof. Dr. Martin Zacharias
Prüfer der Dissertation:	1.	Univ.-Prof. Dr. Thorsten Hugel
	2.	Univ.-Prof. Dr. Franz Pfeiffer

Die Dissertation wurde am 04.09.2013 bei der Technischen Universität München eingereicht und durch die Fakultät für Physik am 11.11.2013 angenommen.

Abstract

Magnetic drug targeting is a technique where complexes of magnetic nanoparticles and an active substance are accumulated in a certain region in the body via an external magnetic field. The complexes are injected into the body, transported via the blood flow and subsequently retained and accumulated in the target region. For a successful approach, information about the local flow conditions, the required magnetic set-up as well as the particle properties is necessary. In this work, we investigate the characteristic attributes and behavior of magnetic nanoparticles. Taking local conditions and particle properties into account, we can estimate the accumulation of the complexes with the help of computational methods. We present a model for vascular targeting with a full three-dimensional analysis of the magnetic and fluidic forces and a subsequent evaluation of the resulting trajectories of the complexes. We examine the influence of modeling input parameters like flow velocity or the distribution of the size and magnetic moment of the nanoparticle complexes. Furthermore, we provide experimental data and compare the results gained by experiment and simulation. In summary, we are able to predict the amount of retained particles as well as their spatial distribution and find a good agreement between experiment and simulation.

Zusammenfassung

Die magnetische Anreicherung von Wirkstoffen oder das magnetische *drug targeting* ist eine Methode, bei welcher Komplexe bestehend aus magnetischen Nanopartikeln und einem gebundenen Wirkstoff durch äußere magnetische Felder gezielt in bestimmten Körperregionen angereichert werden. Die Komplexe werden in den Körper injiziert, durch den Blutfluss transportiert und anschließend im Zielgebiet festgehalten und angereichert. Hierfür ist detailiertes Wissen über lokale Flussbedingungen, benötigte magnetische Felder und Partikeleigenschaften notwendig. In dieser Arbeit werden die wesentlichen Verhaltensmerkmale von Nanopartikeln untersucht. Mit Hilfe der lokalen Randbedingungen und Partikeleigenschaften, sowie computergestützer Berechnungen, kann das Verhalten und die Anreicherung von Nanopartikel Komplexen für verschiedene Anwendungen vorhergesagt werden. Es wird ein Model für die Anreicherung in Gefäßen vorgestellt, welches magnetische und strömungsmechanische Kräfte dreidimensional in Betracht zieht und davon ausgehend die Bewegungsbahnen der Partikel analysiert. Darüber hinaus wird der Einfluss der Modellparameter, wie Flussgeschwindigkeit, Größenverteilung und magnetisches Moment der Partikel untersucht und Simulationsergebnisse werden mit experimentellen Daten verglichen. Sowohl die simulierte Menge, als auch die Verteilung der angereicherten Partikel können vorhergesagt werden und stimmen gut mit den experimentellen Ergebnissen überein.

Contents

1

Introduction

In the last decade, nanoparticles and their possible applications have attracted a great deal of attention. Nanoparticles and nanomaterials offer various possibilities in different scientific fields [1, 2], including environment [3–5] and agriculture [6], semiconductor [7, 8] and materials science [9, 10] as well as pharmaceutics [11] and biomedicine [12, 13]. The applications range from consumer products such as paints, sunscreens and cosmetics, over industrial usage as monitors, sensors, catalysts, seals, lubricants and conducting thin films to research applications as solar cells and drug carriers. In the field of biomedicine, nanoparticles are most often applied for therapeutic and diagnostic applications. Among the most promising applications in this field are magnetic separation, drug targeting and delivery, hyperthermia as well as the use as contrast agents.
Figure 1.1 shows an electron microscopy image of several nanoparticles. In general, nanoparticles have a size ranging from a few nanometers to approximately a tenth of a micrometer. Nanoparticles are smaller than cells and comparable in size to viruses, proteins, genes and DNA [13, 14]. An important property of nanoparticles is the ability of being coated with biological molecules. Thereby, they are able to interact with or bind to biological substances and effectively label the substance.
Nanoparticles come in several different variations. On the one hand, they can be distinguished due to their material as magnetic or non-magnetic. On the other hand, they can exist as individual nanoparticles separated from each other or as nanoparticle complexes where they aggregate with each other or with other materials. Additionally, they can be integrated in different sorts of carriers, like *magnetic microbubbles (MMBs)* [15] or cells [16–18]. Nanoparticles in a liquid can either exist as a ferrofluid, which is a stable, colloidal suspension of nanoparticles with a high particle density, or as a diluted suspension with a low particle density. A ferrofluid typically contains 10^{17} particles per milliliter and is opaque to visible light [19], while typical particle suspensions contain approximately 10^{11} particles per milliliter and are translucent. Due to the varying particle density, ferrofluids and suspensions with individual nanoparticles are often mathematically described and treated differently. While ferrofluids can be treated as fluid, particle suspensions are treated as colloidal suspensions or solids in a fluid.

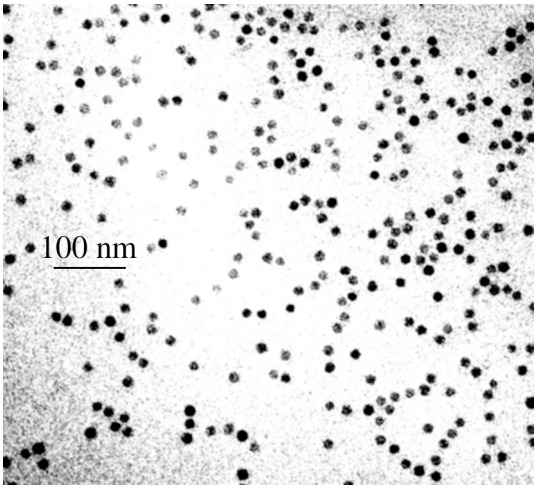

Figure 1.1: Electron microscopy image of magnetic nanoparticles*

Magnetic nanoparticles (MNPs) experience a force in an inhomogeneous magnetic field and are drawn towards the magnetic field source. Thereby, they can be diverted by an external magnetic field gradient. This behavior offers various applications including the immobilization and transport of magnetic nanoparticles or magnetically labeled substances, as used for e.g. *magnetic targeting* or *separation* [16, 20, 21]. The general idea of both applications is to magnetically label substances with nanoparticles and thereby immobilize them against a flow or to draw the magnetic objects out of the surrounding fluid with the help of an appropriate magnetic field.
For *in vitro* experiments, this approach is often advantageous to separate specific biological contents from their environment in order to use them for subsequent applications. To this purpose, *magnetic separation* employs the labeling of the desired biological substance with magnetic nanoparticles via adhesive surface coatings, e.g. dextran or phospholipids, or specific binding agents like antibodies [22]. Subsequently, the labeled substance is separated from the non-labeled surroundings by passing through a magnetic gradient field.
A more advanced application of this principle is the *magnetic targeting in* or *ex vivo*. This technique suggests the binding of magnetic nanoparticles to certain biological contents, e.g. migrating cancer cells, and the subsequent guidance out of the body via an external separation mechanism [23]. Vice versa, drugs and genetic material can be bound beforehand to nanoparticles and subsequently administered locally. This *in vivo* application is known as *magnetic drug targeting (MDT)*. Most therapeutic drugs are applied intravenously and have often severe systemic side effects. A localized treatment by magnetic drug targeting can facilitate a high accumulation of the drug or the genetic material at the targeted area. Thereby, high concentrations

*Electron microscopy image was provided by M. Hanzlik, Electron Microscopy, Department of Chemistry, Technische Universität München

of the respective substance can be established. Consequential, undesirable systemic side effects can be decreased or even prevented while simultaneously enhancing the efficacy [24, 25]. The targeting is accomplished by binding the magnetic nanoparticles to drugs, genetic material or cells and retaining them at a specific area via an external magnetic field. The particles themselves can be applied using several procedures, e.g. intravascular injection, near the target region and are subsequently transported by the blood flow. At the target region, they are retained and held in place by an external magnetic field [25–28].
Another property of magnetic nanoparticles is the possibility to respond resonantly to time-varying magnetic fields. Thereby, nanoparticles can be heated and utilized for *hyperthermia*. This approach is mostly used on cancer cells and there are products already approved for clinical usage, e.g. NanoTherm [mag]. The particles are injected near the target tissue, transported via blood flow and bound to the target cells. An external alternating magnetic field of sufficient strength and frequency is applied and causes the particles to heat up. This heat conducts into the surrounding tissue, achieving a temperature of approximately 44 °C inside the tissue and destroying the cells over time. Whereas general hyperthermia devices can also damage healthy tissue, the use of magnetic nanoparticles and a specific binding increases efficacy by heating primarily the targeted tissue [29, 30].
Apart from spacial manipulations of the nanoparticles, the relatively large magnetic moments of magnetic nanoparticles can be utilized as contrast agents. *Magnetic resonance imaging (MRI)* uses a large, homogeneous magnetic field to align the magnetization of specific nuclei (e.g. ^{1}H) in an object. Another electromagnetic field, which is perpendicular to the main magnetic field and has the resonance frequency of the nucleus, is applied. This second field causes the magnetization vectors of the nuclei to flip and subsequently a fast decaying signal can be measured. This signal decay is associated with two different relaxation times T_1 and T_2. In the presence of such large homogeneous magnetic fields, magnetic nanoparticles affect the local field noticeably. Thereby, the use of magnetic nanoparticles changes the T_2 relaxation values, and, to that effect, changes the contrast in the resulting image [31, 32]. There are several different brands approved as contrast agents, e.g. Resovist [bay] and Feridex / Endorem [gue].

In summary, magnetic nanoparticles can have useful applications for therapy, imaging and diagnostics of different diseases by transporting bound therapeutics or diagnostic materials to the area of interest. The destination may be targeted by magnetic forces or specific surface coatings. Though often intended for cancer therapy and diagnosis, magnetic nanoparticles can be utilized for many different diseases like endothelial, ocular or respiratory diseases [33]. The application in the cardiovascular system is of special interest from the scientific point of view. Due to the high flow rates, it is increasingly difficult to achieve high retention rates. Especially interesting in this context is the targeting of specific regions of vessels and the heart as well as the delivery of genetic material (nucleic acids, cells and viral vectors [16–18, 34]) under flow conditions and *in vivo*.

For a successful application of magnetic drug targeting *in vivo*, an accurate understanding of the underlying processes is necessary. To gain this knowledge, we study the magnetic targeting of nanoparticles and their complexes and investigate the behavior of those nanoparticles under experimental conditions. The main contribution to success or failure of the application is the effective magnetic force on the nanoparticles. This force depends on the one hand, on the magnetic field source, and on the other hand, on the used magnetic nanoparticles. Due to the physical restrictions on the range of the magnetic field, a successful *in vivo* application is limited to applications close to the surface. Alternatively, the utilization of magnetizable implants, like needles, wires or stents, could help in generating high and localized magnetic field gradients and thereby enhance the magnetic force in deeper tissues [35–38]. Furthermore, the use of larger particles or aggregated particle complexes can also enhance the magnetic force by increasing the magnetic moment of the attractable objects [39, 40]. However, aggregated nanoparticles can cause vascular blockages if the aggregate size becomes too large [41, 42] or even cause platelet aggregation [43]. Both effects lead to thrombosis and are not desired for *in vivo* applications.
After a successful application, the magnetic nanoparticles remain in the body for a certain time. While *in vitro* studies on cells show varying grades of toxicity dependent on the particle type [44–46], *in vivo* studies [44, 47, 48] indicate that the iron oxide inherent in magnetic nanoparticles is accumulated mostly in the liver and spleen and slowly clears over the course of several days or a few weeks without ill effects.

There are many groups focusing on magnetic drug targeting, but few can explain or support their experimental findings by theoretical models, or even further knowledge about the used or necessary magnetic fields or information about the magnetic properties of the nanoparticles. While it is possible to conduct successful experiments with, e.g., a randomly chosen magnet, the results may differ considerably for slight changes in the experimental conditions. This can entail everything between no accumulation of nanoparticles for too weak field sources and a clogging of vessels if the utilized magnetic field sources are too strong. Only through detailed knowledge, a reproducibility and predictability of the results of the approach can be ensured. Without this information, an accurate description and understanding of the processes is not possible and thereby, deductions about success or failure of an experiment are not conclusive.
Theoretical models describing the magnetic drug targeting approach can include hydrodynamic, magnetic and physical boundary conditions, three- or two-dimensional analysis and additional contributions of minor forces. While Nacev *et al* base their models on diffusion [49, 50], Gitter *et al* and Alexiou *et al* mainly focus on ferrofluids [51, 52]. Both approaches are only of limited use for low particle densities. Other groups, working with particle-based simulations, often use mean particle properties [53] or disregard acceleration in their models [54]. However, most groups simplify their geometry to two dimensions [55] and do not investigate the influence of particle

properties like the distribution of hydrodynamic diameter or magnetic moment and therefore the results lack statistical validity.

In this work, we specifically concentrate on the targeting of magnetic nanoparticles and bound material to vessels. To gain an understanding of the behavior of magnetic nanoparticles, we investigate characteristic particle properties in different environments. Furthermore, we simulate the trajectories of particles under static and flow conditions and verify our models by comparing simulations with the respective experiments.
In the first part, we expand on the different properties of magnetic nanoparticles and introduce the basic theory for the transport of those nanoparticles and their complexes in fluids. With the help of computational methods, the accumulation and behavior of the nanoparticles can be predicted in dependence on the field source, the particle type and properties as well as the local flow conditions.
Subsequently, we describe the magnetic field sources designed for our experiments as well as the used numerical and experimental methods.
Additionally, we study the intrinsic behavior of magnetic nanoparticles; we investigate the physical properties of the magnetic nanoparticles as well as changes in their behavior in different environments. As a result, we present a method to determine the magnetic moment of nanoparticles via light transmission in a well-defined magnetic field. To implement this method, we introduce a custom measurement device. Additionally, we present a similar method for the measurement of the magnetic moment of larger magnetically labeled objects.
Finally, we take those informations into account and analyze the movement of the nanoparticles. Thereby, we are able to estimate the amount and position of nanoparticles which can be retained by an external magnetic field under specified conditions. The trajectories of individual particles are calculated with respect to the physical boundary conditions, the magnetic properties of both, the external field and of the particles as well as the hydrodynamics of the fluid. To achieve this, we combine finite element calculations with Monte-Carlo techniques. We present a model for vascular targeting with a full three-dimensional analysis of the magnetic and fluidic forces and a subsequent evaluation of the trajectories and the resulting accumulation of the nanoparticles. We implement this model in a static and local gene targeting application as well as in a dynamic arterial model.

2

Theory

2.1 Magnetic Nanoparticles

Nanoparticles are small objects with different shapes and a size between a few nanometers and approximately a tenth of a micrometer [13, 14]. Magnetic nanoparticles additionally demonstrate a magnetic dipole moment $\vec{\mu}$ in an external magnetic field. The magnetic and physical properties of the nanoparticles are strongly dependent on material and size [13]. Most interesting are particles with sizes comparable to magnetic domains in the corresponding bulk material. Figure 2.1 shows the dependency of the inherent magnetism on the core size of the nanoparticle for typical materials. Additionally, most nanoparticles have a surface coating which increases their overall size but in general does not change the magnetic behavior. Magnetic nanoparticles can usually be classified as paramagnetic, ferromagnetic and superparamagnetic corresponding to their size and bulk material [13, 24, 32]. In the following, we describe the most common types of magnetism for nanoparticles.

Paramagnetism In the absence of a magnetic field, the dipole moments of a paramagnetic material are randomly oriented. In the presence of a magnetic field, the dipole moments align with the external magnetic field. With increasing field strength, more dipole moments align with the external field until all moments are aligned. The complete magnetization of a particle is defined as magnetic saturation. Paramagnetic materials usually saturate at very high magnetic field strengths, e.g. gadolinium chloride start to saturate at 50 T [56]. Once the external magnetic field is removed, all magnetic moments are again randomly oriented due to thermal influences. Hence, no remanence occurs in paramagnetic materials.

Ferromagnetism Ferromagnetic particles are characterized by a remanent magnetization behavior. Ferromagnetic materials are structured by Weiss domains where the magnetic dipole moments of each domain are aligned due to exchange interaction. Without an external magnetic field, the resulting magnetizations of the individual domains are randomly oriented. When applying an external magnetic field, the domain walls reorganize and the total magnetic moment is oriented in the direction of the external field. In contrast to paramagnetic materials, ferromagnetic materials usually saturate at mediate field strength, e.g. most ferrites saturate at 0.2-0.5 T.

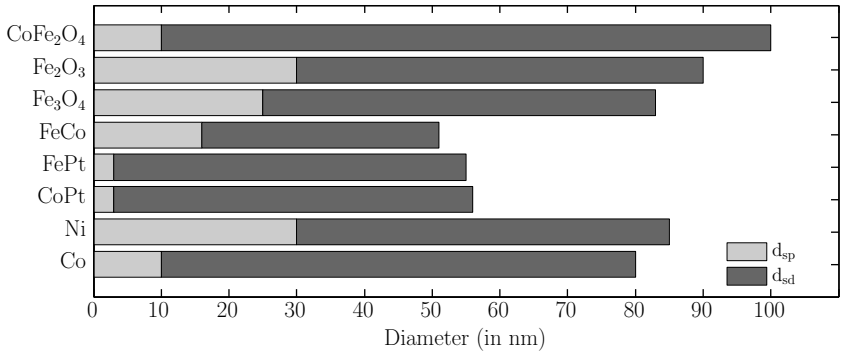

Figure 2.1: Magnetic behavior of different materials as a function of size; superparamagnetism occurs for diameters in the range of d_{sp}, single domain ferromagnetism occurs for diameters in the range of d_{sd} and multiple domain structures occur at larger diameters (following Krishnan [31])

After removing the external field, the magnetization of the material can partially or even fully remain. This behavior is called remanence. Thereby, ferromagnetic material can act as a permanent magnet.

Superparamagnetism If a ferromagnetic particle consists of only one domain and the core size is below a critical value, superparamagnetism occurs, compare also figure 2.1. Without an external magnetic field, the direction of the magnetization can randomly flip due to thermal influences, causing an apparent magnetization of zero. When applying an external magnetic field, the magnetic moment begins to align with the external field. The field strength needed to saturate superparamagnetic materials is of the same order of magnitude as the field strength necessary for ferromagnetic materials. At the same time, superparamagnetic particles show no remanence in the absence of an external field.

Usually, superparamagnetic and ferromagnetic particles consist of a magnetic core and a surface coating as shown in figure 2.2a. The core material, size and shape mainly define the magnetic properties of a superparamagnetic or ferromagnetic particle. The core material is responsible whether the particle is paramagnetic or ferromagnetic at a certain temperature. Dependent on the application, the core material differs, but often metal oxides, especially iron oxides like magnetite (Fe_3O_4) or maghemite (Fe_2O_3) are used for magnetic nanoparticles. For temperatures higher than the material specific Curie temperature, ferromagnetism and superparamagnetism disappear and the material exhibits paramagnetic behavior. Furthermore, there are so called multi-core nanoparticles, consisting of several individual core particles surrounded by a collective coating.

In this work, we confine ourselves to superparamagnetic iron-oxide particles. In the following, we consider magnetic nanoparticles as well as three types of carriers

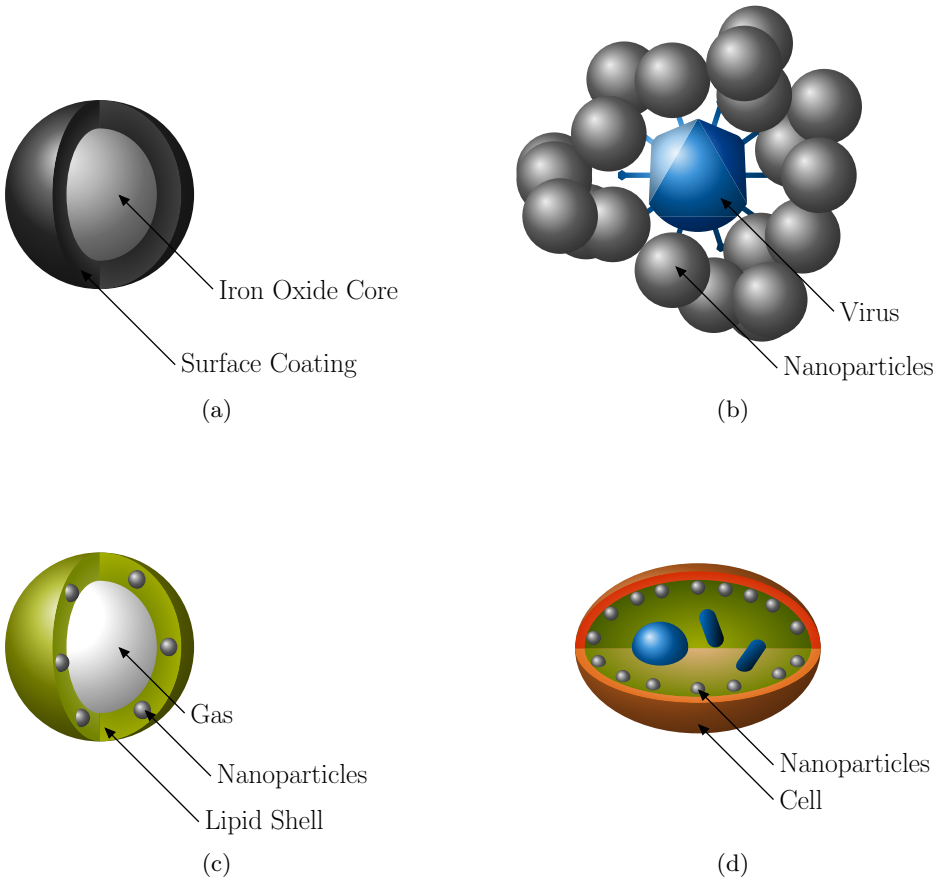

Figure 2.2: Schematic drawings of a nanoparticle (a), a nanoparticle / virus complex (b), a microbubble (c) and a cell (d) loaded with nanoparticles; sizes are not to scale; typical diameters for complexes are in the range of a few hundred nanometers, while microbubbles and cells typical have diameters of several micrometers.

as shown in figure 2.2. While figure 2.2a displays an individual nanoparticle with its core and coating, panel b shows a complex consisting of magnetic nanoparticles and a virus particle, e.g. lentivirus or adenovirus. Those complexes are formed via electrokinetic interactions by incubating viral particles and magnetic nanoparticles in buffer solutions [57]. The virus particles can contain fluorescent proteins like eGFP (enhanced green fluorescence protein) which allows us to observe their behavior microscopically. Furthermore, nanoparticle complexes can consist solely of magnetic nanoparticles. Those aggregates form via different surface interaction forces and depend on the surrounding fluid.
Another type of carriers are magnetic microbubbles which are shown in figure 2.2c. Those contain a high molecular weight hydrophobic gas, such as perfluorocarbons, and can circulate within blood. They incorporate a large number of magnetic nanoparticles which leads to a high magnetic moment compared to a single nanoparticle. By choosing an appropriate membrane, microbubbles can be made flexible

Property	Symbol	Order of magnitude
Core diameter^I	d_{core}	$10^{-9}\,\text{m}$
Hydrodynamic diameter^I	d_h	$10^{-8}\ldots10^{-7}\,\text{m}$
Hydrodynamic diameter^C	d_h	$10^{-7}\ldots10^{-6}\,\text{m}$
Core volume^I	V_{core}	$10^{-28}\ldots10^{-25}\,\text{m}^3$
Hydrodynamic volume^I	V_h	$10^{-25}\ldots10^{-22}\,\text{m}^3$
Hydrodynamic volume^C	V_h	$10^{-22}\ldots10^{-19}\,\text{m}^3$
Density	ϱ	$10^3\,\text{kg/m}^3$
Mass	m	$10^{-21}\ldots10^{-15}\,\text{kg}$
Magnetic moment^I	μ	$10^{-22}\ldots10^{-19}\,\text{Am}^2$
Magnetic moment^C	μ	$10^{-22}\ldots10^{-13}\,\text{Am}^2$
Magnetization correlated to V_h	M_V	$10^2\ldots10^5\,\text{A/m}$
Magnetization correlated to A_h	M_A	$10^{-5}\ldots10^{-3}\,\text{A}$
Zeta potential	$\lvert\zeta\rvert$	$10^1\ldots10^2\,\text{mV}$

Table 2.1: Typical orders of magnitude for particle properties where the index I or C refers to properties specific to individual nanoparticles or particle complexes, respectively; magnetic moment and magnetization are given at saturation

and behave much like red blood cells squeezing even through capillaries. Thereby a higher magnetic moment can be achieved while at the same time the risk, e.g. for thrombosis, is minimized [15].
Finally, cells can also be loaded with magnetic nanoparticles as shown in figure 2.2d. Here, magnetic nanoparticles - often bound to viral vectors or the like - are added to a cell culture. The particles sediment onto the cells within a few minutes, followed by the uptake of the particles into the cells [16–18]. The process can be enhanced by centrifugation or the application of a magnetic gradient field.

Depending on the application, different properties of the magnetic nanoparticles are of interest. For the magnetic targeting of the particles, the most interesting properties are hydrodynamic size and magnetic moment, whereas coating and zeta potential are interesting for binding particles to nucleic acids or DNA. Table 2.1 shows a list of the most common properties and their order of magnitude for single particles and complexes consisting of particle aggregations.

2.1.1 Non-Magnetic Properties

Size Distribution

The most apparent properties of nanoparticles are size and shape, e.g. spherical, ellipsoidal, cylindrical or cuboidal [58, 59]. In the following, we deal only with spherical or nearly spherical nanoparticles. Additionally, we have to distinguish between core size and hydrodynamic size of individual nanoparticles and complexes of nanoparticles. The core diameter describes the size of the iron oxide core of the nanoparticle, whereas the hydrodynamic diameter includes the coating and describes the whole nanoparticle.
Depending on the fluid, the nanoparticle type and / or the addition of viral complexes, the particles may start forming complexes which contain a large number of nanoparticles. Their hydrodynamic size is about an order of magnitude larger than of individual particles and can gain diameters up to a few micrometers. Figure 2.3a shows an electron microscopy image* of SO-Mag5 nanoparticles in HBSS where the aggregation to larger complexes has taken place.
In the following, the term "nanoparticle" describes individual particles as well as any aggregation of particles with themselves or in combination with other substances, if not mentioned differently. The term "diameter" always corresponds to the hydrodynamic diameter of whatever form the nanoparticles have in the given fluid.
Particle size distributions are usually measured by *dynamic light scattering (DLS)*. Here, the particles are observed via the intensity of their scattered light. The size of the particles is subsequently calculated from their movement via the diffusion coefficient (see also chapter 2.2.3). The diameters of the nanoparticles are supposed to follow a lognormal size distribution [13, 60, 61] and often, the result of a dynamic light scattering measurement is given as an intensity-weighted distribution which can be described sufficiently by a lognormal distribution. As a consequence of this representation, larger particles are more heavily weighted than smaller particles. It is possible to convert the intensity distribution to a number-weighted distribution. This corresponds better to the physical, hydrodynamic size, but changes the general shape of the distribution. Due to the size dependent difference in weighting between both representations, peaks can appear or disappear depending on the weighting of the distribution. Figure 2.3 comparably shows different size distributions as intensity-weighted (panel b) and number-weighted (panel c) distributions. The difference between both distributions can be recognized very well, especially in the difference of the relative peak heights and the near disappearance of the large peaks of the intensity-weighted distributions in the number-weighted distributions. Additionally, if nanoparticle sizes are measured in an ionic medium, the ions affect the electric double layer around the particle (see below, chapter 2.1.1). As a result, the extended double layer can reduce the diffusion speed and thereby enlarge the apparent diameter measured by dynamic light scattering [62, 63].

*Electron microscopy image was provided by M. Hanzlik, Electron Microscopy, Department of Chemistry, Technische Universität München

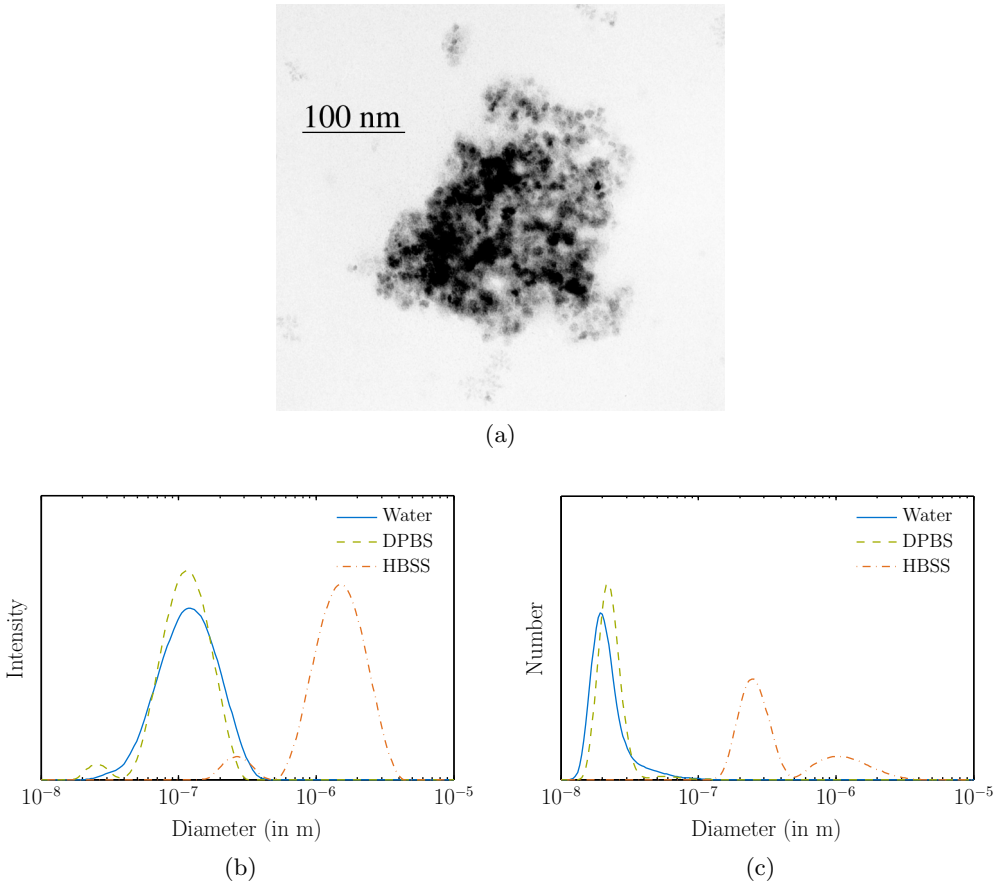

(a) (b) (c)

Figure 2.3: Electron microscopy image* of SO-Mag5 nanoparticles in buffered solution (HBSS) and size distributions as intensity-weighted (b) and number-weighted (c) distribution in water and buffered solutions (DPBS, HBSS)

Mass

The mass of individual magnetic nanoparticles or complexes is difficult to determine. The most feasible way to approximate the mass is by using the mass density of the components, like core and coating material, and their appropriate ratios or, if available, use information provided by the manufacturer. The specifications concerning the density vary between approximately $1.3\,\mathrm{g/cm^3}$ and $5.2\,\mathrm{g/cm^3}$ which corresponds to pure magnetite [64][che] and depend on the particle type. As shown later, this parameter is comparably unimportant. In this work, we assume a mass density of $2.5\,\mathrm{g/cm^3}$ for all nanoparticles and of $1.1\,\mathrm{g/cm^3}$ for cells loaded with nanoparticles [65–68].

Zeta Potential

Nanoparticles in suspension are generally charged. Figure 2.4 shows a schematic of the surface potential of a nanoparticle resulting from the surrounding ions in the

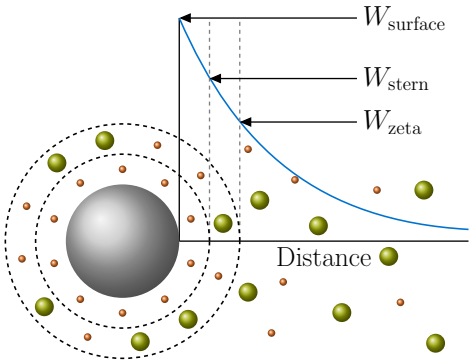

Figure 2.4: Schematic drawing of the surface potential and the ions around a particle in solution; green and red dots indicate opposingly charged ions

suspension. Counter ions are electrostatically attracted toward the particle surface. The resulting surface potential of a particle is partly shielded due to the adsorbed ions (Stern layer). Additionally, a diffuse layer of mixed ions associates themselves with the particle (electrostatic double layer). If the particle is in motion, part of the diffuse layer is sheared off and the remaining charge defines the zeta potential ξ [69]. Thereby, ξ can be determined by measuring the velocity of the particle while moving through an electric field. The zeta potential is dependent on the surrounding fluid and prevents the aggregation of the nanoparticles. It can also be used to electrostatically bind DNA (negative charge) or viruses (positive charge) to nanoparticles with the respective contrary surface charge.

2.1.2 Magnetic Properties

An important non-biological property of a magnetic nanoparticle and a crucial input parameter for our simulations is the magnetic moment or the magnetization of the nanoparticle. The magnetization M describes the strength of the magnetic dipole moment of the nanoparticle at a defined magnetic field strength and is defined as magnetic moment μ per volume of the core material. Thereby, magnetic moment and magnetization are dependent on one another.
Furthermore, the magnetization as well as the magnetic moment depends on the strength of the external magnetic flux density field. Figure 2.5 shows the magnetization curves for the different particle types as measurements and fitted curves. The fit is a Langevin function (see chapter 2.2.1) with an additional linear term, normalized to the fitted saturation magnetization. For a better depiction of the magnetization for small field strengths, figure 2.5b shows those curves in logarithmic scaling.
While the magnetization is usually constant for the same particle type at a certain

*Measurements were kindly performed by A. Bauer, Chair for Experimental Physics II (E21), Department für Physik, Technische Universität München; glass tubes for measurement were manufactured by M. Stanger, Crystal and Material Laboratory, Department für Physik, Technische Universität München

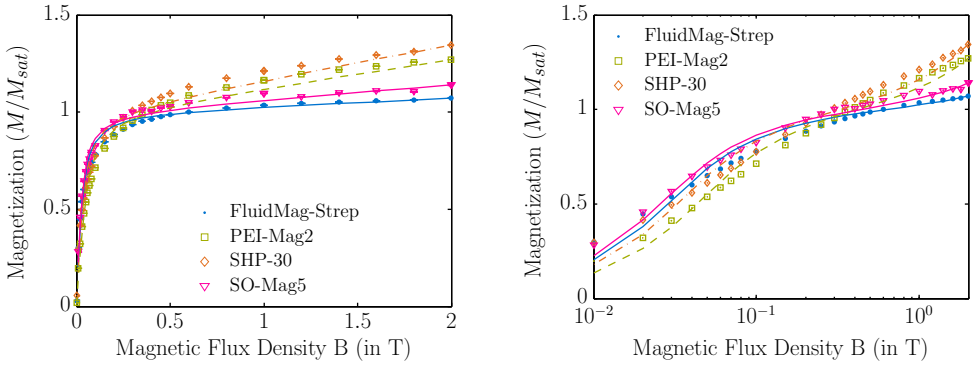

Figure 2.5: Magnetization of different nanoparticles in linear and logarithmic scaling in dependence on the magnetic flux density; values are normalized to their saturation magnetization*

flux density, the magnetic moment varies with the particle size. As a simplification, we assume that the magnetic moment is proportional to the hydrodynamic volume of the nanoparticle instead of the core volume. This is reasonable as long as the coating is homogeneous throughout the particle batch. In case of microbubbles, we assume a proportionality to the surface of the bubble, since the nanoparticles are adsorbed into the lipid shell. Those proportionalities are in the following referred to as *volume magnetization* M_V and *surface magnetization* M_A

$$M_V = \frac{\mu}{V} = \frac{6\mu}{\pi d_h^3}\,, \tag{2.1a}$$

$$M_A = \frac{\mu}{A} = \frac{\mu}{\pi d_h^2}\,, \tag{2.1b}$$

where the term "magnetization" always refers to the hydrodynamic size properties. Due to this proportionality, the distribution we gain for the magnetic moment is of the same form as the distribution for the hydrodynamic diameter. The dependence of the magnetic moment and the magnetization on the strength of magnetic flux density field is in the following referred to as "Langevin behavior".

Measurement

The magnetic moment of a nanoparticle complex, microbubble or cell can only be measured indirectly by observing the objects in a well-defined and known magnetic field. Most of the known methods to measure the magnetic moment of nanoparticles focus on the magnetization of the particles or the magnetic moment of a bulk of particles. In the following, we briefly describe the most commonly used methods.

Magnetization Measurement The magnetization behavior of nanoparticles can be measured with several similar instruments, e.g. a SQUID (superconducting quantum interference device). The principle of the measurement is common for most methods. The sample is positioned inside of a system of superconducting coils, resulting in an induced current which is proportional to the magnetization [70]. Thereby, not only the magnetization of the sample can be obtained, but also the dependency of the magnetization on the magnetic flux density. The obtained value of the magnetization is usually given in magnetic moment per weight or per volume. Thereby, it is obvious that the measured value is the magnetization for the whole bulk of particles and detailed knowledge of the amount or number of particles is necessary to determine the moment for individual particles.

Force Measurement There are several approaches to determine the magnetic moment of nanoparticles by measuring the force acting on the nanoparticles in a magnetic field. The magnetic moment of individual nanoparticles can be measured by the force necessary to move the particles towards or away from a magnetic field source with Atomic Force Microscopy [71]. Thereby, it is also possible to determine the magnetization curve of the particles. Another possible approach is to measure the change of the weight force under the influence of a magnetic field with a Gouy, Faraday or other precision balances [72–74]. However, both methods are highly susceptible to disturbances and require high precision equipment.

Optical Velocity Measurement Complexes of nanoparticles, microbubbles or cells which are large enough to be seen under a microscope, can be tracked optically in a magnetic field. Häfeli *et al* [64] as well as Zborowski and Chalmers *et al* [56, 65] used this method to track magnetic microspheres and magnetically labeled cells in a magnetic force field. This is also known as "Cell Tracking Velocimetry" or "Particle Tracking Velocimetry". The measured quantity is often called "magnetophoretic mobilty" and refers to the velocity of the objects induced by a magnetic field. The magnetic set-ups vary from complex electromagnets to single large permanent magnets. Often the cells are carried along by a laminar flow and diverted by a magnetic force perpendicular to their streamline. Based on the deviation from their original path, the magnetophoretic mobility and thereby the magnetic moment of the particles can be determined.
Additionally, there are approaches to determine the magnetic moment via the eccentricity of the trajectory in oscillating magnetic fields [75].
Depending on their size, individual nanoparticles and smaller complexes may be visible under a microscope, but their visibility may not produce high enough optical contrast to allow for an automatic evaluation. Thereby, those methods are mostly suitable for larger complexes or cells.

Indirect Optical Velocity Measurement Another approach is to observe the nanoparticles indirectly via the optical density of the suspension [76, 77]. Similar to the direct observation, the nanoparticles move in the presence of an external

inhomogeneous magnetic field which results in a decrease of the optical density over time. Mykhaylyk *et al* estimate the magnetic moment from the elapsed time and the mean distance covered by the particles.

2.2 Targeting Model

In the following, we describe the fundamentals of the magnetic targeting approach. We introduce the forces acting on a magnetic nanoparticle and the physical principles behind them.
The main principle of magnetic targeting is based on the fact that magnetic nanoparticles are pulled towards a magnetic field source. This attracting force can drag the nanoparticles through a fluid or hold the particles against an external flow.
There are several forces acting on a magnetic nanoparticle or nanoparticle complex in a targeting scenario; the main contributions are illustrated in figure 2.6 and described by the following two forces: first, the magnetic force $\vec{F}_{\text{mag}}$, due to an external magnetic gradient field, accelerates the complexes towards the magnetic field source. As a consequence, the complex is diverted from its original trajectory into the direction of rising magnetic flux density. Second, the hydrodynamic force $\vec{F}_{\text{hydro}}$ is caused by the friction of the particle against the fluid. In the case of a dynamic flow, the hydrodynamic force adds an additional contribution via the flow of the fluid. Combining both forces, we can calculate the trajectories of the magnetic nanoparticles. There are several minor forces acting on the nanoparticles which are described in more detail later in this chapter. The resulting movement of the particles stops once they reach a physical boundary where we assume they adhere [27, 78].

Generally, we divide our modeling approaches into static and dynamic models. The static model involves no flow of the fluid, whereas the dynamic case includes a fluid with a nonzero flow velocity. Furthermore, to model arteries and other vessels, we approximate the vessels by simple cylindrical shapes. Realistic artery geometries include an uneven surface with some irregularities. Those have little influence on our result, but would complicate our calculations unnecessarily due to the more complex geometry. In the following we discuss the influencing forces individually.

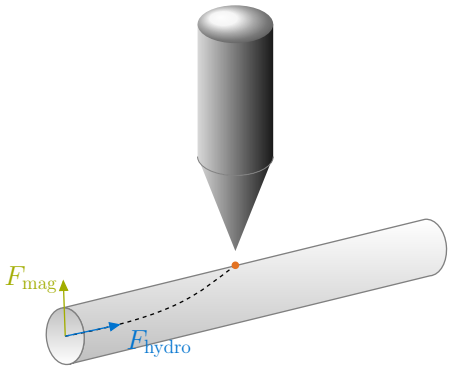

Figure 2.6: Basic principle of magnetic targeting: magnetic (green) and hydrodynamic force (blue) acting on a nanoparticle (orange) and the resulting particle trajectory (dashed)

2.2.1 Magnetostatics

Magnetic and electric fields are described by the Maxwell equations [79],

$$\nabla \cdot \vec{D} = \rho\,, \qquad \nabla \times \vec{E} = -\frac{\partial \vec{B}}{\partial t}\,, \tag{2.2a}$$

$$\nabla \cdot \vec{B} = 0\,, \qquad \nabla \times \vec{H} = \vec{j} + \frac{\partial \vec{D}}{\partial t}\,, \tag{2.2b}$$

where $\vec{E}$ and $\vec{D}$ describe the electric field and the electric displacement field, while $\vec{B}$ and $\vec{H}$ describe the magnetic flux density field and the magnetic field, respectively. ρ and $\vec{j}$ denote the charge and current density. In this work, we restrict ourselves to magnetic fields generated by permanent magnets, thereby limiting the problem to static magnetic fields without external current densities. This simplifies equations 2.2b to

$$\nabla \cdot \vec{B} = 0\,, \qquad \nabla \times \vec{H} = 0\,. \tag{2.3}$$

Combining those relations with

$$\vec{B} = \mu_0 \left(\vec{H} + \vec{M}\right)\,, \tag{2.4a}$$

$$\vec{B} = \nabla \times \vec{A}\,, \tag{2.4b}$$

where μ_0 is the permeability of the vacuum, $\vec{M}$ is the magnetization and $\vec{A}$ is the magnetic vector potential, we can in principle derive the magnetic flux density for every combination of permanent magnets. Since most geometries are too complex to calculate the fields analytically, we solve those problems with the finite element software package *Comsol Multiphysics* [com] (see chapter 3.2.1).

Based on the computed magnetic flux density, we are able calculate the magnetic force $\vec{F}_{\text{mag}}$. The force acting on a nanoparticle with the magnetic dipole moment $\vec{\mu}$ within an external static magnetic flux density field $\vec{B}$ is described by

$$\vec{F}_{\text{mag}} = (\vec{\mu} \cdot \vec{\nabla})\vec{B}\,. \tag{2.5}$$

Due to the characteristic superparamagnetic behavior, all magnetic moments of the nanoparticles are aligned in the direction of the external magnetic field and the magnetic moment is therefore defined by

$$\vec{\mu} = \mu \hat{B}\,, \tag{2.6}$$

where $\hat{B}$ denotes the unit vector in the direction of the magnetic flux density field $\vec{B}$ and $\mu = |\vec{\mu}|$ is the absolute value of the magnetic dipole $\vec{\mu}$. The magnetic force of a static magnetic flux density field can thereby be simplified to

$$\vec{F}_{\text{mag}} = \mu \cdot \vec{\nabla}|\vec{B}|\,, \tag{2.7}$$

Thus, the magnetic force is proportional to the gradient of the magnetic flux density as a first approximation. However, the value of the magnetic dipole moment μ of a superparamagnetic nanoparticle depends on the absolute value of the local magnetic flux density $B = |\vec{B}|$. Similar to ferromagnetic materials, the moment increases with the magnetic flux density until a saturation value μ_{sat} is reached. This behavior can be described by

$$\mu = \mu_{\text{sat}} \mathcal{L}(B)\,, \tag{2.8}$$

where $\mathcal{L}$ is the Langevin function [40]

$$\mathcal{L}(B) = \coth\left(\mathcal{E}B\right) - \frac{1}{\mathcal{E}B}\,, \qquad \text{with} \tag{2.9a}$$

$$\mathcal{E} = \frac{\mu_{\text{sat}}}{k_B T}\,. \tag{2.9b}$$

Here, k_B is the Boltzmann constant and T denotes the temperature. This especially means that the force is not only dependent on the strength of the magnetic field, but the shape and position of the magnetic field source relative to the target are as important as the magnetic flux density itself, since those are crucial for the distribution of the magnetic flux density gradient. For sufficiently small magnetic flux densities, the Langevin function can be approximated by [19]

$$\mathcal{L}(B \ll B_{\text{sat}}) \approx \frac{\mathcal{E}}{3} B\,. \tag{2.10}$$

thereby leading to the force

$$\vec{F}_{\text{mag}} = \frac{\mu_{\text{sat}}^2}{3\,k_B T} B \cdot \vec{\nabla} B\,. \tag{2.11}$$

However, measurements often show an additional paramagnetic contribution to the magnetic moment. This contribution might originate from a magnetic "dead layer" at the surface of the magnetic core. Due to a break in the crystal system of the structure at the surface and / or the binding of the coating molecules, a slight difference in the magnetic structure of the core can occur and result in a non-superparamagnetic contribution [57, 80]. The saturation behavior is thereby better described by

$$\mu = \mu_{\text{sat}} \left(\mathcal{L}(\mathcal{E}B) + \mathcal{E}'B\right)\,, \tag{2.12}$$

where $\mathcal{E}'$ is an appropriate proportionality factor. As an additional consequence, the Langevin parameter $\mathcal{E}$ is not always in agreement with its definition in equation 2.9b. Therefore, $\mathcal{E}$ and $\mathcal{E}'$ are usually determined by measurements.

2.2.2 Fluid Dynamics

The description of the flow of a fluid can be divided into different classes, e.g. laminar, turbulent, compressible, incompressible, Newtonian or non-Newtonian flow. For our application, we are only interested in the classifications of laminar and turbulent flow as well as Newtonian and non-Newtonian fluids.

- Newtonian fluids are described by a constant viscosity η, whereas the viscosity of non-Newtonian fluids depends on the shear rate $\dot{\gamma}$.
- Turbulent flow is characterized by eddies and vortices, often resulting from irregularities in the surrounding geometries or by high velocities. A laminar flow is a flow without turbulences. Turbulent and laminar flow are distinguished by a critical Reynolds number Re_{crit}. Flow with Reynolds numbers higher than Re_{crit} becomes unstable against small variations and evolves into turbulent flow.

For the special case of flow in a cylinder with radius R_{cyl}, the Reynolds number is defined as [81]

$$Re = \frac{2\bar{u}}{\nu} R_{\text{cyl}} \,, \tag{2.13}$$

where $\bar{u}$ is the mean velocity of the fluid and the kinematic viscosity ν is defined as

$$\nu = \frac{\eta}{\varrho} \,, \tag{2.14}$$

with the dynamic viscosity η and the density ϱ of the fluid. The critical Reynolds number Re_{crit} can vary between approximately 1000 and 2500 [82, 83].
In general, the flow of an incompressible fluid is described by the Navier-Stokes equation [81]

$$\varrho \left(\frac{\partial \vec{u}}{\partial t} + \vec{u} \cdot \nabla \vec{u} \right) = -\nabla p + \eta \left(\nabla^2 \vec{u} \right) \,, \tag{2.15}$$

where $\vec{u}$ denotes the velocity of the fluid. In the case of laminar flow inside a cylinder, the flow velocity along the flow axis z can be described by the Hagen-Poiseuille law

$$u_z(r) = \frac{\partial V}{\partial t} \frac{2}{\pi R_{\text{cyl}}^4} \left(R_{\text{cyl}}^2 - r^2 \right) \tag{2.16}$$

$$= 2\bar{u}_{in} \left(1 - \frac{r^2}{R_{\text{cyl}}^2} \right) \,, \tag{2.17}$$

where r is the radial position. The volumetric flow rate and mean inflow velocity are denoted by $\partial V/\partial t$ and $\bar{u}_{in}$, respectively. For those cases, where the geometries and boundary conditions exceed laminar Newtonian flow in a cylindrical vessel, the fluid dynamics have been modeled with *Comsol Multiphysics*.

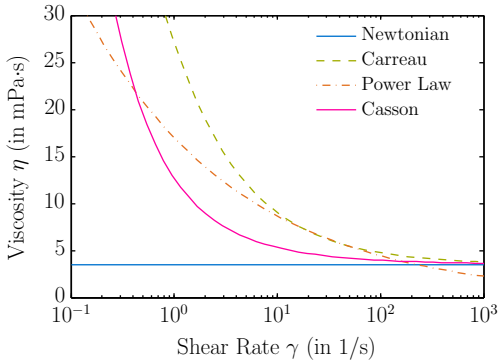

Figure 2.7: Characteristics of the viscosity of blood for Newtonian, power law, Casson and Carreau-Yasuda model

The resulting force acting on the nanoparticle is caused by the friction between fluid and particle. Since we mostly consider laminar flow conditions in this work and additionally, are solving the resulting equation of motion (equation 2.41) on a very small scale, this can be described by the Stokes' drag force. For a spherical particle moving with a velocity $\vec{v}$ in a fluid, this force is given by

$$\vec{F}_{\text{hydro}} = 3\pi \cdot \eta d_h \left(\vec{u} - \vec{v}\right) , \tag{2.18}$$

where d_h denotes the hydrodynamic diameter of the nanoparticle [81]. The Stokes force consists on the one hand of the drag exerted on the particle by the flow velocity $\vec{u}$, on the other hand it has a component opposing any external force via the velocity $\vec{v}$. The relative velocity of the particle $\left(\vec{u} - \vec{v}\right)$ is in the following also referred to as $\Delta\vec{v}$.

Fluid Dynamics of the Blood Flow

Blood consists of several different elements, like red and white blood cells as well as platelets, suspended in plasma. The majority of those components are red blood cells which have a large influence on the flow characteristics of blood. At low shear rates, the red blood cells form rouleaux, thereby increasing the viscosity. The rouleaux disperse with higher shear rates and the viscosity converges towards Newtonian behavior. Thereby, blood is a non-Newtonian fluid and the viscosity is a function of the shear rate

$$\dot{\gamma} = \frac{\partial \vec{u}}{\partial \vec{x}} . \tag{2.19}$$

Additionally, the behavior of the viscosity is influenced by the size of the vessel and the hematocrit value [84, 85].
There are several models to describe the dynamic viscosity of non-Newtonian flow;

Parameter	Symbol	Value
Flow consistency index	k	$0.017\,\mathrm{Pa}^{\beta}$
Power law index	β	0.708
Yield stress	τ_0	$0.005\,\mathrm{N}$
Constant Newtonian shear rate	η_{const}	$3.5\,\mathrm{mPa}\cdot\mathrm{s}$
Casson rheological constant	η_c	$3.5\,\mathrm{mPa}\cdot\mathrm{s}$
Infinite shear rate limit	η_∞	$3.5\,\mathrm{mPa}\cdot\mathrm{s}$
Zero shear rate limit	η_0	$56\,\mathrm{mPa}\cdot\mathrm{s}$
Relaxation time constant	Λ	$3.313\,\mathrm{s}$
Power law index (Carreau)	β	0.3568

Table 2.2: Parameters for non-Newtonian models for blood viscosity used in figures 2.7 and 2.8 [84]

among the most common ones are the power law [86], the Casson and the Carreau-Yasuda model [87, 88]. The power law model describes the viscosity as

$$\eta(\dot{\gamma})_{\mathrm{pow}} = k\dot{\gamma}^{\beta-1}\,, \tag{2.20}$$

with the flow consistency index k and the power law index β. However, this model does not accurately describe the need for yield stress as blood at rest requires [84]. The viscosity of the Casson model

$$\eta(\dot{\gamma})_{\mathrm{casson}} = \frac{\tau_0}{\dot{\gamma}} + \sqrt{\frac{\tau_0\eta_c}{\dot{\gamma}}} + \eta_c\,, \tag{2.21}$$

on the other hand fulfills this requirement. Here, τ_0 is the yield stress and η_c is the Casson rheological constant. The third model, the Carreau-Yasuda-Model is defines the viscosity as

$$\eta(\dot{\gamma})_{\mathrm{carreau}} = \eta_\infty + (\eta_0 - \eta_\infty)\cdot\left(1 + (\Lambda\dot{\gamma})^2\right)^{(\beta\,-\,1)/2}\,, \tag{2.22}$$

where η_0 and η_∞ are the viscosities for the shear rate limits, Λ is the relaxation time constant and β denotes the power law index.
The characteristic behavior of the viscosity is shown in figure 2.7 for each model. As a reference, the constant value η_{const} for the blood viscosity in a Newtonian model is included. For shear rates smaller than $100\,{}^{1}/_{\mathrm{s}}$, where the rouleaux formation takes place [84], there are large discrepancies between the individual models. For large shear rates, the Carreau-Yasuda and the Casson model converge towards the Newtonian value. The parameters used for this figure are listed in table 2.2.
Figure 2.8 shows a qualitative comparison between the parabolic flow profile of a Newtonian fluid in a cylinder and the flattened flow profile of a non-Newtonian fluid like blood, modeled with the Carreau-Yasuda and the power law model. The used parameters for the latter are listed in table 2.2, while the viscosity for the Newtonian fluid is also set to η_{const}. The mean flow rate at the inlet is $1\,{}^{\mathrm{ml}}/_{\mathrm{min}}$.

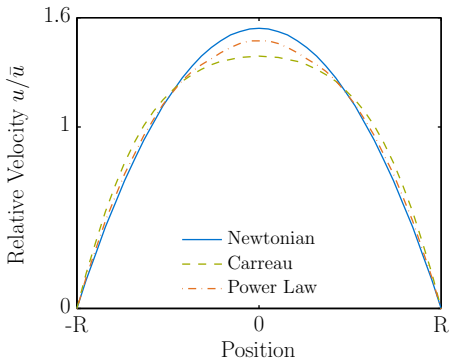

Figure 2.8: Flow profile for blood for Newtonian and non-Newtonian models in the form of Carreau-Yasuda and power law

2.2.3 Minor Forces

There are several minor forces acting on the nanoparticles. Those forces are usually several orders of magnitude smaller than the main forces. Among those are gravitational and buoyancy forces which are negligible for nanoparticles smaller than 1 µm [28, 39], diffusion, Brownian motion [89] or lift forces. If not mentioned differently, we neglect those contributions in this work. Additionally, there are several different types of interaction between particles. Primarily, those interactions result in particle aggregation and the formation of larger complexes. The aggregation of the nanoparticles is taken indirectly into account by using the experimentally determined size distribution of the particles in solution.
The influence of the locally accumulated particles on the hydrodynamic and magnetic force has been neglected: the modification of the fluidic parameters due to the accumulated particles is very small, since there are usually several orders of magnitude between the surrounding volume and the nanoparticle. Hence, the change in the flow velocity is negligible [90]. The effect of accumulated superparamagnetic particles on the local gradient of the magnetic flux density, also known as avalanche effect, has also been neglected.
An estimation for the typical magnitude of the minor forces is given in table 2.3 for the particle properties listed in table 2.1. Nonetheless, we show the impact for selected minor forces in chapters 4.2.2 and 5.3.2.

Gravity

One of the first minor contributions that comes to mind, is the influence of gravity. The gravitational force is defined as

$$\vec{F}_{\text{grav}} = m \cdot \vec{g}\,, \tag{2.23}$$

where $\vec{g}$ is the acceleration in the gravity field of the earth and m is the mass of the nanoparticle complex.

Force	Parameters	Order of magnitude
Hydrodynamic	$u = 0.1\,\mathrm{m/s}$	$10^{-9}\,\mathrm{N}$
Lift	$\Delta v = 0.01\,\mathrm{m/s}$, $\dot{\gamma} = 400\,1/\mathrm{s}$	$10^{-14}\,\mathrm{N}$
Magnetic	$B > B_{\mathrm{sat}}$, $\nabla B = 100\,\mathrm{T/m}$	$10^{-11}\,\mathrm{N}$
	$B = 0.1\,\mathrm{T}$, $\nabla B = 100\,\mathrm{T/m}$	$10^{-13}\,\mathrm{N}$
Gravity	$d_h = 1\,\mu\mathrm{m}$	$10^{-14}\,\mathrm{N}$
Dipole	$s = d_h$	$10^{-14}\,\mathrm{N}$
Sedimentation velocity	$d_h = 1\,\mu\mathrm{m}$	$10^{-6}\,\mathrm{m/s}$
Brownian movement	$d_h = 1\,\mu\mathrm{m}$	$10^{-6}\,\mathrm{m/s}$
Magnetic velocity	$B > B_{\mathrm{sat}}$, $\nabla B = 100\,\mathrm{T/m}$	$10^{-3}\,\mathrm{m/s}$

Table 2.3: Maximum orders of magnitude of the forces acting on nanoparticles and resulting nanoparticle velocities for typical particle properties as listed in table 2.1

Lift Force

Small particles in a non-homogeneous flow experience a force in the direction of higher velocities as shown in figure 2.9. This shear lift force originates in the viscous flow of the fluid around the particle, which essentially differs on the different sides of the particle. Saffman [91] derived an analytical expression for the lift force under the assumption of [92–94]

$$Re_{\mathrm{v}} = \frac{d_h \Delta v}{\nu} \ll 1\,, \tag{2.24a}$$

$$Re_{\gamma} = \frac{\dot{\gamma} d_h^2}{\nu} \ll 1\,, \tag{2.24b}$$

$$Re_{\Omega} = \frac{\Omega d_h^2}{\nu} \ll 1\,, \tag{2.24c}$$

$$\vartheta = \frac{\sqrt{Re_{\gamma}}}{Re_{\mathrm{v}}} = \frac{\sqrt{\dot{\gamma}\nu}}{\Delta v} \gg 1\,, \tag{2.24d}$$

where Ω is the rotational angular speed of the particle. Saffman's expression for the lift force is then

$$\begin{aligned} \vec{F}_{\mathrm{lift,Sa}} &= 1.615\sqrt{Re_{\gamma}} \cdot \eta d_h \Delta v \\ &= 1.615\sqrt{\dot{\gamma}\eta\varrho} \cdot d_h^2 \Delta v\,. \end{aligned} \tag{2.25}$$

McLaughlin [92] generalized this analysis and obtained the following expression for the lift force

$$\vec{F}_{\mathrm{lift}} = \frac{J(\vartheta)}{J(\vartheta)|_{\vartheta\to\infty}} \vec{F}_{\mathrm{lift,Sa}}\,, \tag{2.26}$$

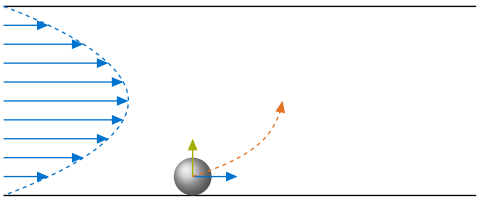

Figure 2.9: Schematic drawing of a particle in shear flow; blue arrows indicate the hydrodynamic flow, the green arrow indicates the lift force and the orange arrow indicates the resulting force

where $J(\vartheta)$ is an empirical expression given by

$$J(\vartheta) = 0.6765 \left(1 + \tanh\left(2.5 \log\left(\vartheta + 0.191\right)\right)\right) \left(0.667 + \tanh\left(6(\vartheta - 0.32)\right)\right), \tag{2.27}$$

which converges to 2.255 for $\vartheta \to \infty$ (Saffman limit).

Brownian Motion, Diffusion and Sedimentation

Small particles in a liquid or gas are subject to random motion due to the collision with atoms and molecules. The mean distance Δs covered per time step Δt by the random motion is determined by [24, 95]

$$\Delta s = \sqrt{6D\Delta t}\,, \tag{2.28}$$

where D is the diffusion coefficient in a fluid and described by the Stokes-Einstein law

$$D = \frac{k_B T}{3\pi\eta d_h}\,. \tag{2.29}$$

Due to this random movement, the particles statistically move towards regions with lower particle concentrations C. The resulting transport phenomenon, known as diffusion, is described by

$$\frac{\partial C}{\partial t} = \nabla \cdot (D \nabla C)\,. \tag{2.30}$$

If gravitation and diffusion are in an equilibrium state in the system [96, 97], the particles in the fluid are suspended. If the condition for the equilibrium is not fulfilled, sedimentation occurs. This behavior can be approximated by the Peclet number

$$Pe = \frac{V_h \Delta\varrho\, g}{k_B T} \cdot z\,, \tag{2.31}$$

where g is the gravitational acceleration and z is the relative position of the particle in sedimentation direction. $\Delta\varrho$ is the difference between the density of the particle

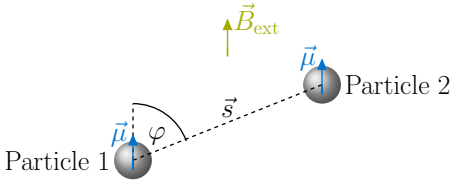

Figure 2.10: Interaction between two superparamagnetic nanoparticles in an external magnetic flux density field

and the surrounding fluid. While small values can be associated with no or very slow sedimentation, larger values imply a faster sedimentation. Only for $Pe/z \ll 1$, there is no sedimentation.
If the diffusion is neglected as a counterforce to gravity, the sedimentation velocity can be approximated by

$$v_{\text{sedim.}} = \frac{d_h \Delta\varrho\, g}{18\eta}\,. \tag{2.32}$$

Interaction Forces

Additionally to external forces, there are several possibilities for nanoparticles to interact either with each other, with the molecules of the solution or the surrounding tissue or material.

Magnetic Interaction Superparamagnetic nanoparticles in an external magnetic field exhibit an induced magnetic dipole moment. The magnetic flux density of a dipole with the moment μ at distance s is defined as [19, 79, 98]

$$\vec{B}_{\text{dipole}} = \frac{\mu_0}{4\pi s^3}\left(3(\vec{\mu}\cdot\hat{s})\hat{s} - \vec{\mu}\right) = \frac{\mu_0}{4\pi s^3}\mu\left(3\cos(\varphi)\,\hat{s} - \hat{\mu}\right)\,, \tag{2.33}$$

where φ describes the angle between the distance vector $\vec{s}$ and the dipole vector $\vec{\mu}$ of the particle, as indicated in figure 2.10. Consequently, the interaction energy and force between two nanoparticles can be obtained by

$$W_{\text{dipole}} = \frac{\mu_0}{4\pi s^3}\left(-3(\vec{\mu}_1\cdot\hat{s})(\vec{\mu}_2\cdot\hat{s}) + \vec{\mu}_1\cdot\vec{\mu}_2\right) \tag{2.34}$$

$$\vec{F}_{\text{dipole}} = -\nabla W_{\text{dipole}}\,. \tag{2.35}$$

Figure 2.10 shows the schematic interaction between two nanoparticles with identical magnetic moments $\vec{\mu}$, as occurs when two identical particles are aligned parallel to an external magnetic field. In this case, the magnetic force reads

$$\vec{F}_{1,2} = -\frac{3\mu_0}{4\pi}\frac{\mu^2}{s^4}\left[\left(5\cos^2(\varphi) - 1\right)\hat{s} - 2\cos(\varphi)\,\hat{\mu}\right]\,. \tag{2.36}$$

For the minimal distance between both particles ($s = d_h$) and locations in line with each other ($\vec{s}||\vec{\mu}$, $\varphi = 0$), the force is at its maximum

$$\vec{F}_{\max} = -\frac{3\mu_0}{2\pi}\frac{\mu^2}{d_h^4}\,. \tag{2.37}$$

This behavior can result in aggregation of magnetic nanoparticles in an external magnetic field. According results are shown in chapter 4.3.

Surface Interaction Short ranged surface interactions in combination with the above mentioned forces like Brownian motion, diffusion or magnetic interaction, can lead to the formation of particle aggregates. Several mechanisms are known to cause interactions between colloidal particles in suspensions. Polymers applied on the particle coating can interact and yield to steric interactions [99, 100]. In an aqueous solution, hydrogen bonding can occur [99]. The two main contributions, however, are the van der Waals attraction W_{vdW} and the opposing repulsion due to an electrical double layer potential W_{edl}. Those forces are described by the classical DLVO-theory, named after Derjaguin, Landau, Verwey and Overbeek [24, 101, 102]. The interaction is mainly defined by the surface potential ψ_0 of the particles and the composition of the solvent. Since the value of the surface potential is not easily determinable, either the Stern or the zeta potential is often used as the surface potential.

For two identical particles with radius r and a core distance s, the van der Waals and the electric double layer potential for small potentials read [102]

$$W_{\mathrm{vdW}} = -\frac{A_H}{6}\left(\frac{2r^2}{s^2-4r^2} + \frac{2r^2}{s^2} + \ln\left(\frac{s^2-4r^2}{s^2}\right)\right) \tag{2.38a}$$

$$W_{\mathrm{edl}} = 4\pi\varepsilon\psi_0^2 \begin{cases} \dfrac{r}{2}\ln\big(1+\exp\big(-\kappa(s-2r)\big)\big) & \text{for } \kappa r > 5 \\ \dfrac{r^2}{s}\exp\big(-\kappa(s-2r)\big) & \text{for } \kappa r < 5 \end{cases}, \tag{2.38b}$$

with

$$\kappa = \sqrt{\frac{2N_A e^2 I}{\varepsilon_{\mathrm{sol}} k_B T}}\,, \tag{2.38c}$$

where A_H is the Hamaker constant, e is the elementary charge, N_A is the Avogadro constant and $\varepsilon_{\mathrm{sol}}$ is the dielectric permittivity of the solvent. The Debye-length κ^{-1} is defined above in dependence on the ionic strength I and has approximately the value $3 \cdot 10^{-10} \cdot 1/\sqrt{I}$ for water at room temperature.
Analytic expressions for the repulsive double layer potential of the DLVO theory are derived from the Poisson-Boltzmann equation and are subject to many assumptions and approximations. One of the first assumptions is that cations and anions of the

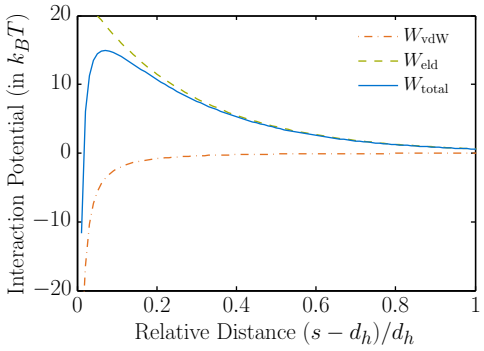

Figure 2.11: Van der Waals, electric double layer and total interaction potential between particles in solution

electrolyte solution are of the same valence (1:1 solution), [e.g. 96, 102, 103]. This is a very drastic constraint as we will see later in chapter 4.3. Additionally, the above given equation 2.38c is based on the Debye-Hückel approximation for small potentials.
The Hamaker constant A_H is material dependent and there are several ways to estimate it [96, 103]. Based on the Lifshitz theory, the non-retarded Hamaker constant describing the interaction of two identical particles across a medium reads

$$\begin{aligned} A_H &= A_{H,\nu_e=0} + A_{H,\nu_e>0} \\ &= \frac{3}{4} k_B T \left(\frac{\varepsilon_{\text{prt}} - \varepsilon_{\text{sol}}}{\varepsilon_{\text{prt}} + \varepsilon_{\text{sol}}} \right)^2 + \frac{3h\nu_e}{16\sqrt{2}} \frac{\left(n_{\text{prt}}^2 - n_{\text{sol}}^2 \right)^2}{\sqrt{n_{\text{prt}}^2 + n_{\text{sol}}^2}^3} , \end{aligned} \tag{2.39}$$

where ν_e is the electronic absorption frequency, typically around $3 \cdot 10^{15}$ Hz. $n_{\text{prt,sol}}$ and $\varepsilon_{\text{prt,sol}}$ are the refractive index and the dielectric permittivity of the particle material or solvent in the visible frequency range, respectively. In case of electrolyte solutions, a screening due to the ionic charges occurs and the zero-frequency distribution gains an additional term. The Hamaker constant is then given by

$$A_H = A_{H,\nu_e=0} \exp\big(-\kappa s\big) + A_{H,\nu_e>0} \,. \tag{2.40}$$

Figure 2.11 shows both potentials W_{vdW} and W_{edl} as well as the resulting total potential W_{total} for nanoparticles with a diameter of 20 nm and a zeta potential of 50 mV in a 100 mM salt solution. Note that the zeta potential also indirectly depends on the ionic strength. With increasing ion concentration, the electric double layer potential decreases more swiftly. Thereby, leading to a point where its influence is virtually neutralized at a critical ionic strength I_{crit} and there is no more repulsive component. At this point, one has to take near-field forces into account.

Adhesive Forces on the Vessel Wall As a consequence of the movement of the nanoparticle towards the magnetic field source, it can occur that a particle comes in contact with the vessel wall. Here, several additional forces contribute to the forces acting on the particle. The main contributions to the detachment of the particle are the hydrodynamic and the lift force. Here, only the tangential components at the center of the nanoparticle are of interest. Additionally, there are Born repulsion, van der Waals forces and electric double layer forces which correlate in a complex way. This makes it difficult to predict the behavior for realistic surfaces. Nonetheless, experiments show that nanoparticles do not detach from a surface for low to mediate flow velocities [27].

2.2.4 Particle Trajectories

Combining the above mentioned forces and contributions, the complete trajectory of an individual magnetic nanoparticle is described by the equation of motion 2.41. With the explicit magnetic (equation 2.7) and hydrodynamic force (equation 2.18), this equation reads

$$m\dot{\vec{v}} = \mu(B(\vec{x}))\vec{\nabla}B(\vec{x}) + 3\pi\eta d_h\left(\vec{u}(\vec{x}) - \vec{v}\right) + \vec{F}_{\text{minor}}\,, \tag{2.41}$$

where $\vec{v} = \dot{\vec{x}}$ is the velocity of the nanoparticle and $\vec{F}_{\text{minor}}$ denotes a combination of minor forces. The gradient of the magnetic flux density $\vec{B}$ as well as the flow velocity $\vec{u}$ depend on the position $\vec{x}$ inside the container or vessel. Additionally, the magnetic moment depends on the position if the magnetic saturation is not reached.

2.3 Optics

Every time, a beam of light encounters some kind of object, it is diverted from its trajectory and scattered. The scattering is often accompanied by absorption, e.g. by transformation into thermal energy. Both, scattering and absorption remove energy from the propagating light and it is attenuated. This attenuation is called extinction [104]. The corresponding physical quantity is called absorbance and describes the loss of light intensity loss due to scattering and absorption and is measured as the optical density of a substance[†]. In this work, we neglect possible absorption processes and only consider the scattering of light.

2.3.1 Beer-Lambert-Law

The Beer-Lambert-Law states that the light absorbance $\mathcal{A}$ by a substance is proportional to the distance s the light propagates through the material. The attenuation coefficient α which describes this relation can be expressed as a product of the molar extinction coefficient ϵ and the concentration C of the attenuating substance. Alternatively, α can be expressed by the extinction cross section σ_E and the number N of objects per volume V

$$\mathcal{A} = \alpha \cdot s = \epsilon \cdot C \cdot s = \sigma_E \cdot \frac{N}{V} \cdot s \,. \tag{2.42a}$$

For a constant distance s, the concentration of a substance can be measured by the light intensity through the medium. The correlation between light transmission $\mathcal{T}$, absorbance $\mathcal{A}$ and the concentration C of the sample substance is described by[‡]

$$\mathcal{A}(C) = -\ln\big(\mathcal{T}(C)\big) \qquad = \epsilon \; s \; C \,, \tag{2.42b}$$

$$\mathcal{T}(C) = \frac{\mathcal{I}}{\mathcal{I}_0} \qquad = \exp\big(-\epsilon \; s \; C\big) \,, \tag{2.42c}$$

where $\mathcal{I}$ and $\mathcal{I}_0$ are the light intensity with and without the sample, respectively. However, the Beer-Lambert-Law has several limitations. Foremost is the requirement of low concentrations and the homogeneity of the scattering substance.

2.3.2 Scattering of Light

The scattering of light with the wavelength λ by spheres with a diameter d is generally described by Mie scattering. If we consider light scattering in another medium

[†]The meaning of the described expressions may sometimes vary, depending on the reference but in this work are used as explained above.

[‡]The distinction between fluids and solids and thereby between Euler's number and 10 as base for equation 2.42 is not required in our case, since we are not interested in the absolute value of the extinction coefficient.

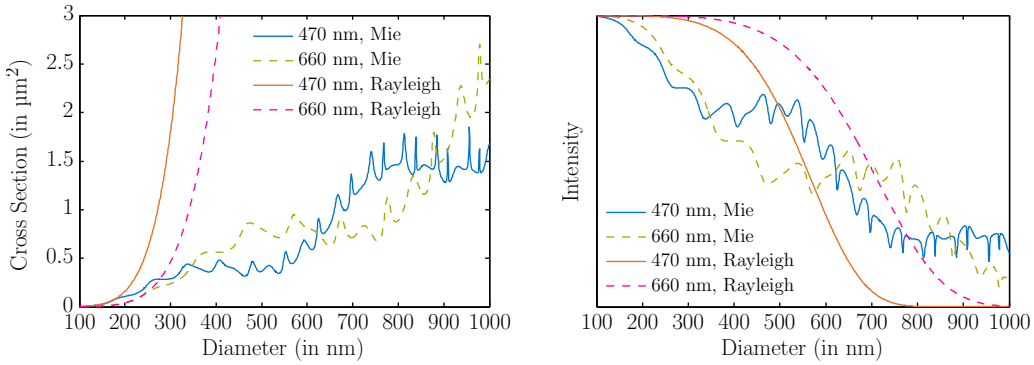

(a) (b)

Figure 2.12: Extinction cross section (a) and relative intensity (b) for 470 and 660 nm as well as for Mie and Rayleigh scattering

than air or vacuum, we have to use the corresponding wavelength in the solvent and the relative refractive index

$$\lambda = \frac{\lambda_0}{n_{\text{sol}}}\,, \tag{2.43a}$$

$$n = \frac{n_{\text{prt}}}{n_{\text{sol}}} \tag{2.43b}$$

where λ_0 is the wavelength of the light in vacuum and $n_{\text{prt,sol}}$ are the refractive indices of the particle and solvent, respectively.
The description of the light scattering according to Mie is very extensive and for a more detailed description, see e.g. [104–106]. In the following, we describe only the necessary equations for our application. The absorption cross section reads

$$\sigma_E = \frac{\lambda^2}{2\pi} \sum_{m=1}^{\infty} (2m+1)\, \Re\left(a_m \left(\frac{d\pi}{\lambda} \right) + b_m \left(\frac{d\pi}{\lambda} \right) \right)\,, \tag{2.44a}$$

and is a function of the size dependent Mie coefficients

$$a_m(x) = \frac{n^2 j_m(nx) \left[x j_m(x) \right]' - j_m(x) \left[n x j_m(nx) \right]'}{n^2 j_m(nx) \left[x h_m^{(2)}(x) \right]' - h_m^{(2)}(x) \left[n x j_m(nx) \right]'}\,, \tag{2.44b}$$

$$b_m(x) = \frac{j_m(nx) \left[x j_m(x) \right]' - j_m(x) \left[n x j_m(nx) \right]'}{j_m(nx) \left[x h_m^{(2)}(x) \right]' - h_m^{(2)}(x) \left[n x j_m(nx) \right]'}\,, \tag{2.44c}$$

which in turn are functions of the spherical Bessel $j_m(x)$ and Hankel functions $h_m^{(1,2)}(x)$ with their corresponding derivatives

$$\left[x f_m(x) \right]' = x f_{m-1}(x) - m f_m(x)\,. \tag{2.44d}$$

Following [104, 107], the extinction coefficient for a solution of objects with a size distribution $f(d)$ is described by the accumulation of the individual cross sections

$$\epsilon = \frac{N}{V} \sum_{d} \sigma_{E,d} = \int f(d) \sigma_{E,d} \, \mathrm{d}d \,. \tag{2.45}$$

If the diameter d of the sphere is much smaller than the wavelength of the light, the scattering can be simplified and described by Rayleigh scattering. The scattering cross section is then described by

$$\sigma_{\text{Rayleigh}} = \frac{2\pi^5}{3} \frac{d^6}{\lambda^4} \left(\frac{n^2 - 1}{n^2 + 2} \right)^2 . \tag{2.46}$$

The measurements in this work are conducted with a wavelength of either 470 nm or 660 nm and the investigated nanoparticles may range from 100 nm to approximately 1 µm. Figure 2.12a shows the extinction cross section as defined in equations 2.44a and 2.46 for both wavelengths and sphere diameters ranging from 100 nm to 1 µm. It can be seen that the Rayleigh approximation works well for diameters up to approximately a third of the wavelength. Figure 2.12b displays the intensity for Mie as well as for Rayleigh scattering for the same wavelengths and sizes. The results are scaled to accommodate both, Mie and Rayleigh scattering.

3

Materials and Methods

In the following, we describe the materials and methods used for the results of chapters 4 and 5. This includes magnetic field sources for two experimental and two measurement set-ups. The former are designed for the experimental verification of a static as well as a dynamic model. The measurement devices are intended for the determination of the magnetic moment of either magnetically labeled cells and microbubbles or magnetic nanoparticles and nanoparticle complexes.
Furthermore, we shortly introduce the general methods used for our models and simulations. More detailed descriptions of the algorithms are given in the corresponding sections of chapter 4 and 5.

3.1 Magnetic Field Sources

In general, there are two different forms of magnetic fields: static time-independent and dynamic time-dependent fields. While static time-independent magnetic fields can be generated by permanent magnets and certain electromagnets, time-dependent fields have to originate in electromagnetic field generators. The latter can be used to create oscillating magnetic forces and therefore provide a three dimensional spatial and temporal guidance of magnetic nanoparticles. However, since permanent magnets are very simple to utilize and apply, we limit the following description to set-ups containing permanent magnets.

3.1.1 Halbach Cylinders

In this work, we mostly use magnetic set-ups based on the Halbach array. This has the advantage of achieving relatively homogeneous and large field gradients. A Halbach array is an infinite arrangement of permanent magnets where the magnets are rotated perpendicular to the axis of the array. As a result, the magnetic field on one side of the array is increased, while the field on the other side is nearly canceled [108]. A special application of the Halbach array is the Halbach cylinder. Here, several permanent magnets are uniformly arranged parallel to the axis of the cylinder, while the magnetization vectors of the magnets are located in the plane perpendicular to the axis. The direction of the magnetization is given by

$$\vec{M} = M_{\mathrm{rem}} \left(\sin\left(k\varphi\right) \hat{x} - \cos\left(k\varphi\right) \hat{y} \right) , \tag{3.1}$$

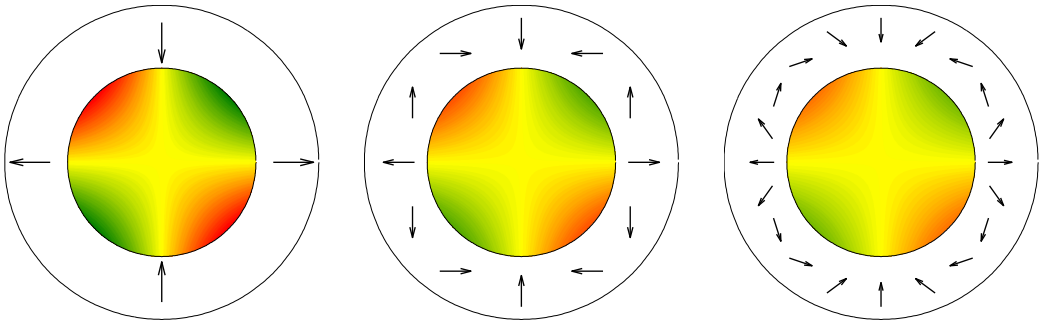

(a) (b) (c)

Figure 3.1: Halbach cylinder seen from above with 4 (a), 12 (b) and 20 magnets (c); arrows indicate the magnetization of the permanent magnets, color indicates the axial component of the magnetic vector potential; units are arbitrary but identical throughout all three figures

where M_{rem} is the remanent magnetization of the magnets. A choice of $k > 0$ leads to an internal magnetic field and $k < 0$ to an external magnetic field. For our applications, we are interested in a magnetic flux density field inside the cylinder which decreases linearly. This can be achieved with a Halbach cylinder with $k = 3$ which leads to a magnetic vector potential with four poles (quadrupole) as shown in figure 3.1. Ideally, the magnetization in the magnetic ring of the Halbach cylinder varies continuously. The generated magnetic flux density would then be perfectly uniform and entirely confined to the inside of the cylinder. For a realistic set-up, the number of magnets limits the homogeneity in close distance to the magnets. Figure 3.1 shows Halbach cylinders for $N = 4$, 12 and 20 magnets. The number of magnets has to be at least 4, but is otherwise not limited. The magnets can also be arranged in multiple concentric rings to achieve a higher magnetic flux density. Please note, that the magnets for the individual set-ups are not identical in size, but chosen in such a way that they can be accommodated around the cylinder, while maximizing the volume of the square sectioned magnets. The axial component of the magnetic vector potential is indicated by the color inside the magnet ring, where the color scale is arbitrary but identical throughout all three figure. Thereby, a comparability of the three cylinder set-ups without external constraints is achieved. It can be seen that the three set-ups only differ in the strength of the vector potential and not in the shape. The magnetic vector potential inside the cylinder can be estimated by

$$A = c_B \cdot \begin{pmatrix} 0 \\ 0 \\ x \cdot y \end{pmatrix} = c_B \cdot \begin{pmatrix} 0 \\ 0 \\ r^2 \cdot \cos(\varphi) \cdot \sin(\varphi) \end{pmatrix}, \tag{3.2}$$

where x and y denote cartesian coordinates and r and φ denote cylindrical coordinates. The constant c_B can be described by [108]

$$c_B = 2B_{\text{rem}} \left(\frac{1}{r_1} - \frac{1}{r_2} \right) \frac{\cos^2\left(\pi/N\right) \sin\left(2\pi/N\right)}{2\pi/N}, \tag{3.3}$$

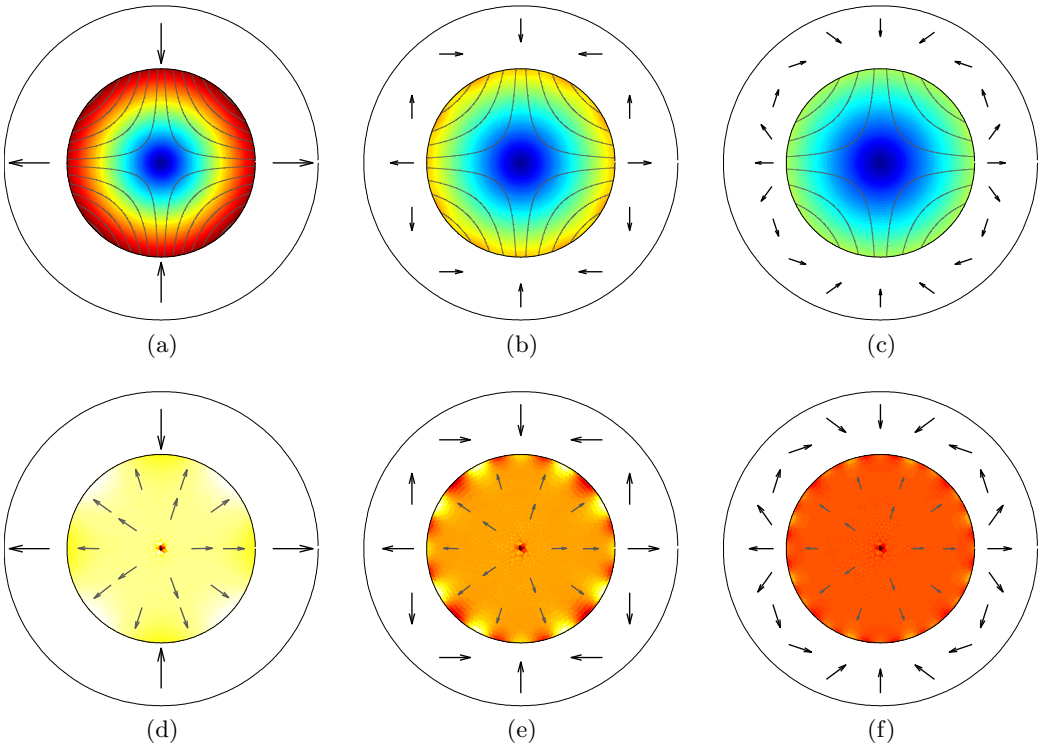

Figure 3.2: Magnetic flux density (a-c) and gradient of magnetic flux density (d-f) in the plane perpendicular to the axis of the cylinder for 4 (a, d), 12 (d, e) and 20 magnets (c, f); units are arbitrary, but identical throughout each row; black arrows indicate the magnetization of the permanent magnets, gray lines (a-c) indicate magnetic streamlines and gray arrows (d-f) indicate direction of magnetic gradient

where r_1 and r_2 are the inner and outer radius of the magnet circle, respectively, and B_{rem} is the remanent magnetic flux density of the permanent magnets. As a result, the absolute value of the magnetic flux density and the gradient of the magnetic flux density can be written in the form of

$$|\vec{B}| = c_B \cdot r \,, \tag{3.4a}$$

$$\nabla|\vec{B}| = c_B \,. \tag{3.4b}$$

Expression 3.3 is based on segment shaped permanent magnets without any space between them. For permanent magnets of other shapes, c_B can be roughly approximated by weighting the expression with the volume or area fraction of the physical magnets

$$c_A = c_B \cdot \frac{A_{\text{magnets}}}{(r_2 - r_1)^2 \pi} \,. \tag{3.5}$$

The resulting magnetic flux density fields for the set-ups in figure 3.1 are shown in figures 3.2a-c for $N = 4$, 12 and 20 magnets. Additionally, the figure shows

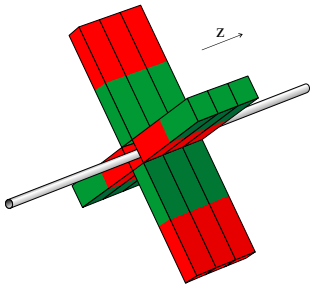

Figure 3.3: Configuration of magnets for arterial targeting: twelve small permanent magnets are positioned in three consecutive quadrupole arrangements; the colors indicate the poles of the magnets

the stream lines of the magnetic flux density as gray lines. The resulting magnetic gradient is shown in figures 3.2d-f where the color indicates the absolute value of the gradient and the arrows indicate the direction. Again, it can be seen that the number of magnets does not influence the shape of the fields, but mainly the strength. However, a higher number of magnets is accompanied by a fewer inhomogeneities of the field gradient in the outer region of the cylinder. Accurate values for magnetic field and gradient are given below for specific set-ups.

Arterial Model

For the investigation of the arterial model in chapter 5.3, we use the geometry shown in figure 3.3. The geometry consists of an artery, modeled as a cylinder with an inner diameter of 0.75 mm and a length of 30 mm, and twelve cuboidal rare-earth permanent magnets (height = 10 mm, width = 2 mm, NdFeB N35; [hkc]) arranged around the artery. The magnets are positioned in four groups of three magnets each. All magnets of each of the triplets have the same orientation among one another. The triplets themselves have an opposing orientation to each other.

Measurement Configuration for Cells

For the observation of cells and microbubbles, we designed a small set-up which can be placed under an inverted microscope. The usage and results of this set-up are described in chapter 4.1. The layout of the set-up is shown in figure 3.4a. Similar to the arrangements described above, 20 small cuboidal rare-earth permanent magnets (height = 20 mm, width = 4.5 mm, NdFeB, N52; [hkc]) are arranged in a Halbach cylinder. Inside the set-up a standard cell culture dish is placed. Additionally, there are several rings which can be used to adjust the z-position of the cell culture dish in a range of 7 mm.

Measurement Configuration for Nanoparticles

To provide a measurement set-up for nanoparticles in a magnetic gradient field, we developed an additional measurement device which is described in detail in

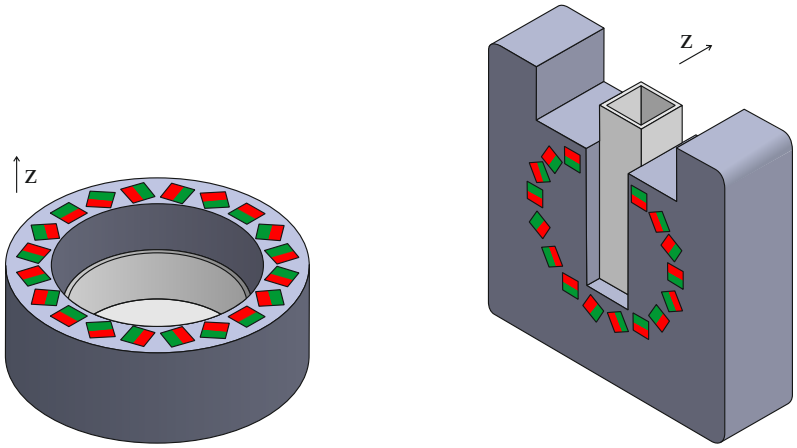

(a) (b)

Figure 3.4: Measurement set-ups for magnetic moments of cells and microbubbles (a) as well as for magnetic nanoparticles (b) with mounting and cell culture dish or cuvette, respectively: in the first case, twenty permanent magnets are positioned in a circle around the cell culture dish (a), in the second case, sixteen permanent magnets are arranged in an incomplete circle around the cuvette (b); colors indicate the poles of the magnets

chapter 4.2. The geometry of this set-up is shown in figure 3.4b. Similar to the arrangements of the magnets above, 16 cuboidal rare-earth permanent magnets (height = 20 mm, width = 4.5 mm, NdFeB N52; [hkc]) are arranged in an incomplete circle. There are two magnets missing at the top of the set-up due to the space required by the cuvette. Additionally, the positions of the remaining four topmost magnets are slightly lower and more inward than their position in a perfect circle. This partly compensates for the missing field contributions of the two omitted magnets.

3.1.2 Other Magnetic Set-Ups

Permanent Magnets with Soft-Iron Tips

To achieve a localized and symmetric accumulation of magnetic nanoparticles, usually a large permanent magnet or an electromagnet with an appropriate tip is used. We built different combinations of soft iron tips (Armco Telar 57, [aks]) and a rare-earth permanent magnet (height = 50 mm, diameter = 30 mm, NdFeB N50, [m4u]) for local transduction and cell positioning [109]. Theoretical and experimental results for the targeting efficacy are discussed in chapter 5.2. Figures 3.5a-c show schematic drawings of three different tip shapes. The tips are denoted according to the diameter on their topmost point (200 µm and 3 mm) and shape (flat and rounded).
The tips themselves were optimized in an iterative process concerning strength and direction of the magnetic gradient field. The topmost and lowest diameters were held constant, while the middle diameter and the heights of the individual parts were varied. Those parameters, as well as the material were subject to parameter runs to obtain the best magnetic gradient field with respect to an optimal magnitude and direction for the desired local particle accumulation.

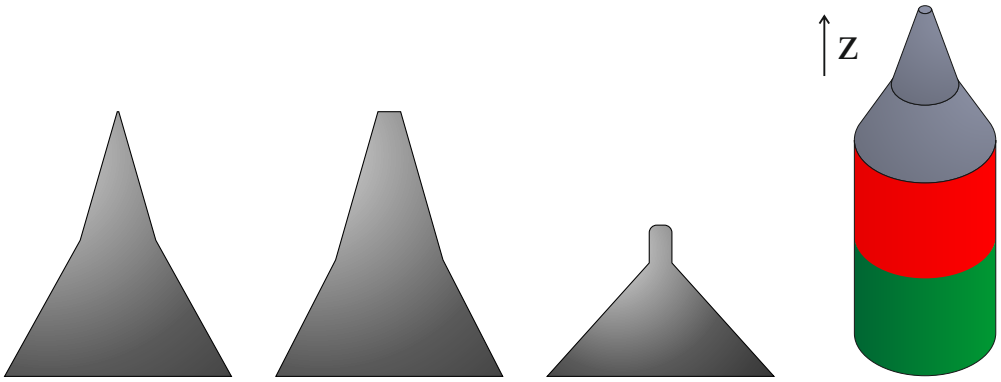

Figure 3.5: Schematic drawing of soft iron tips with different diameters and shapes: 200 µm flat (a), 3 mm flat (b) and 3 mm with a rounded tip (c); 3 mm flat tip mounted on the permanent magnet where the colors indicate the poles of the magnet

3.2 Numerical Methods

The main focus of this work is on the modeling and simulation of particle movement. Thereby, we want to gain an understanding of the different particle types under varying conditions. Based on the individual requirements, we optimize different configurations of magnet geometries and are able to describe the particle trajectories in dependence on the magnetic flux density gradient and the flow conditions (see chapter 2.2). We are using numerical field calculations as a tool to optimize the geometry and Monte-Carlo related methods to predict the resulting trajectories and the accumulation of the nanoparticles. In the following, we address those methods in more detail.

3.2.1 Finite Element Method

The *finite element method (FEM)* is a technique for obtaining approximate numerical solutions for mathematical problems on a discrete mesh. Usually, this method is used for complex geometries or equations which cannot be solved analytically. Depending on the physics, a set of partial differential or integral equations has to be solved. Similar to lattice calculations, the domain is subdivided into a finite number of discrete sub-domains, usually called elements. A set of basis functions are derived from the differential equations and parameterized by the local coordinates. Those basis functions are then solved for each element [110][com].

For the purpose of finite element calculations of the magnetic flux density as well as the flow velocity, we chose the software package *Comsol Multiphysics* and its *AC/DC* and *CFD* module. Here, an interface offers the possibility to define the governing equations for volumes as well as boundary conditions. The relevant equations were solved for triangular or tetrahedral meshes for two or three dimensions, respectively. Typically, the following conditions were set:

- Magnetostatics
  - The **volume** of the individual permanent magnets is described by
    $$\vec{B} = \mu_0 \mu_r \vec{H} + \vec{B}_{\mathrm{rem}} \,,$$
    with the remanent flux density B_{rem} chosen according to the manufacturers declarations (see table A.2) and the relative permeability $\mu_r = 1$ and $B_{\mathrm{rem}} = 0$.
  - The **volume surrounding** the permanent magnets was usually chosen to be air and modeled accordingly with $\mu_r = 1$. The amount of air surrounding the magnets was large enough to permit the magnetic flux density to decline appropriately.
  - The **exterior boundaries** of the surrounding volumes were set as magnetic insulation according to
    $$\vec{n} \times \vec{A} = 0 \,.$$

- Fluid dynamics
  - The **volume** of the fluid was modeled as Newtonian or non-Newtonian fluid with the according material properties as the experiment requested (see chapter 2.2.2)
  - The **inlet** boundary in case of laminar flow was chosen as a laminar inflow profile, supplying a parabolic flow profile from the start; in all other cases, the inlet boundary was modeled with a constant pressure at the inlet and an according region to establish the flow profile
  - The **outlet** boundaries were modeled with a constant pressure of $p = 0$ at the outlet
  - The **remaining** boundaries were chosen as walls with

$$\vec{u} = 0\,.$$

3.2.2 Monte-Carlo Method

In general, *Monte-Carlo (MC)* methods are techniques which use random numbers to make statistical estimates. These estimates can be solutions of deterministic problems, evaluations of integrals or averages over random processes [111]. Monte-Carlo methods are most suited for calculations where an exact result with a deterministic algorithm is infeasible. However, there is no consistent definition of the term *Monte-Carlo method*. The methods vary, but usually consist of the following steps:

1. definition and random generation of input parameters according to a probability distribution;
2. performance of algorithms on the inputs to solve deterministic problems;
3. combination or evaluation of the results.

The most widely known examples for Monte-Carlo methods are Monte-Carlo integration and Markov Chain Monte-Carlo simulations. In this work, we limit the use of random numbers on the input parameters and use completely deterministic algorithms to solve the problems, i.e. differential equations.

3.2.3 Trajectory Simulation and Analysis

Magnetic and fluidic fields were calculated with *Comsol Multiphysics* and the discrete values were subsequently exported into MATLAB [mat] via the *LiveLink for Matlab* module of *Comsol Multiphysics* on previously defined coordinates. Additionally, a domain index was exported to identify every volumetric body, so that it was possible to distinguish between magnet, fluid and surrounding space. Due to the underlying array structure of MATLAB, the coordinates had to be provided on a rectangular grid. In contrast to triangular grids, quadrilateral grids are less accurate [112] and, if rectangular, less flexible. Refinements in one area, result in

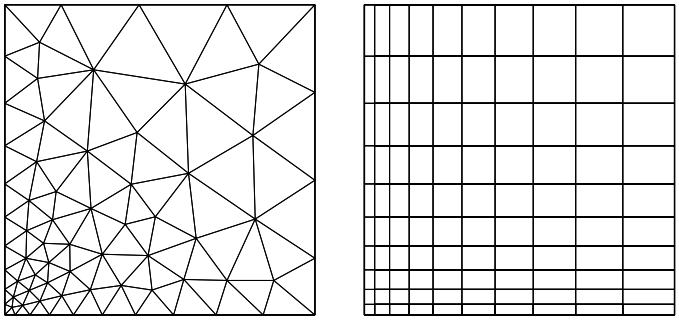

(a) (b)

Figure 3.6: Comparison of triangular and rectangular mesh structures and the result of local refinements

a refinement of the grid in a whole area alongside one axis as shown in figure 3.6. This increases the data volume extremely if there is a need for more detailed data in an area of interest, e.g. detailed data on a vessel wall results in a refined grid over the whole cross section.

The exported data was subsequently available in MATLAB as discrete values. In order to perform accurate differentiations and integrations, it is mandatory to provide smooth and continuous data sets for all variables. Therefore, we used two or three-dimensional smoothing B-splines [113] to generate continuous data sets and to differentiate the magnetic flux density field. To compensate for the mesh-burdened values and to avoid an uneven progression and thereby irregularities in the magnetic gradient, the data was smoothed [114, 115] and a small tolerance was provided for the B-splines. Potentially undefined values on the grid, e.g. the fluid velocity outside of the vessel, were linearly extrapolated to provide data for the spline interpolation. Based on those expressions for magnetic field, gradient, fluid velocity and domain, we solved the differential equation 2.41 and thereby calculated the trajectories for a number of particles. However, depending on the orders of magnitude of the different terms of equation 2.41, the differential equation becomes stiff. This means that for certain numerical methods, the solutions are numerically unstable. It is therefore necessary to use a solving algorithm adapted to such instabilities. In the following, the differential equation 2.41 is always solved with an implicit Runge-Kutta algorithm provided by MATLAB. The algorithm has to stages: the first stage is a trapezoidal rule step and the second stage is a backward differentiation (TR-BDF2, [116]).
After the physical model was build, we generated the random particle properties based on corresponding distributions. All random numbers were generated with the Mersenne Twister method [117] with a seed based on the respective time. An exception is the generation of the random numbers used for Brownian motion. Here, the random numbers must be reproducible for individual steps of the integration, otherwise they interfere with the adaption of the Runge-Kutta algorithm. To achieve

this, the seed was regenerated in each step based on the current position. More detailed remarks concerning evaluation and analysis are given in the corresponding chapters 4.2 and 5.1.

3.2.4 Error Sources

There are several different error sources contributing to the result of our simulations. On the one hand, there are possible errors on the used input parameters and the experimental setup, e.g. geometric and manufacturing variations. On the other hand, there are several possible errors originating solely from the different steps of the simulation. In the following, we list the main error contributions. The experimental error sources include

- variations of the magnetic flux density field and gradient due to manufacturing limits in size and material of the magnetic field sources as well as due to variations in position and distance of the magnets relative to the target and, in case of multiple magnets, to each other;
- variations in the fluid flow, including differing viscosities due to temperature variations, changes in the flow velocity, due to e.g. varying vessel diameters or inaccuracies of the pumping mechanism as well as eddies due to irregularities in the vessel surface;
- inaccurate values for particle properties like hydrodynamic size, magnetic moment and density or mass, due to measurement inaccuracies, statistic fluctuations or fluid-specific aggregation behavior (see also section 4.3).

As discussed in chapters 4 and 5, the last of those error sources has the biggest influence. On the one hand, variations of the particle properties have a large impact on the resulting particle behavior and accumulation; on the other hand, those properties are the most difficult to measure and are the least reliable. Throughout this work, the experimentally determined values are measured in triplicates, whereas we usually describe them by mean value and standard deviation. For input parameters in the form of distributions, e.g. hydrodynamic diameter and zeta potential of the nanoparticles, we determine the resulting distribution by convoluting several individually measured distributions [118] and provide them in terms of mean value and standard deviation of the distribution.
Additionally, there are several possible error sources originating in the simulation:

- inaccuracies of the field calculations via the finite element method and the subsequent interpolation and smoothing process: the consequences of inaccuracies in the field calculations have the same influences as the above mentioned variations of flow velocity and magnetic field sources.
- algorithmic and rounding errors as well as inaccuracies due to limited number of particles: to estimate the error due to the limited number of particles on

global results like retention rates and particle accumulation, we utilized the bootstrapping method [119]. Here, the original dataset is resampled and statistical estimates are calculated on the new samples. The number of samples is chosen to be equal to the number of nanoparticles.

- initial distribution of particles: while we assume a uniform distribution of particles in static models, we present the influence of the initial particle distributions in flow in chapter 5.3.2.

In chapters 4.2.2 and 5.3.2, we investigate the influences of many of those parameters on the final results like retention rate and particle accumulation. Furthermore, we employ several assumptions in our calculations:

- a constant ratio of magnetic moment to particle volume or area
- a spherical shape of the nanoparticles, particle complexes, cells and microbubbles
- movement of nanoparticles, particle complexes, cells and microbubbles independent of one another
- with the exception of the magnetic moment, no change of the particle properties in the presence of a magnetic field
- a negligible contribution of other minor forces

While some of those assumptions are fully justified, some are only valid under certain conditions as we discuss in chapters 4 and 5.

3.3 Experimental Materials and Methods

3.3.1 Technical Materials

Optical Layout of the Measurement Device for Nanoparticles

For the measurement of the magnetic moment of nanoparticles, we designed a device to measure and record the optical density of a particle suspension in the presence of a magnetic field over time. The optical layout and the light path of this device are depicted in figure 3.7. As a light source, we used a duo *light-emitting-diode (LED)* which emits light in the wavelengths 470 nm (blue) and 660 nm (red). The LED intensity was adapted in such a way that a comparable light output for both wavelengths is achieved. The LED is followed by a collimating lens with a focal length of 12 mm and a numerical aperture of 0.14. After passing the lens, the light beam has an approximate diameter of 9 mm. To further reduce the diameter, exchangeable apertures can be employed. Note, that small apertures also reduce the light output by approximately their squared diameter.
Subsequently, the light beam irradiates the particle suspension and enters the detector which provides a square wave signal whose frequency is proportional to the light intensity.

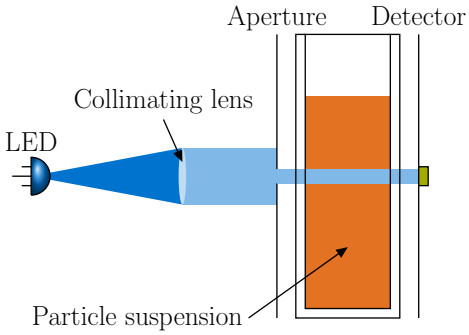

Figure 3.7: Optical set-up of the measurement device for nanoparticles; light is emitted from the LED and collimated by the lens; after passing through the particle suspension, the remaining light intensity is measured by the detector

3.3.2 Experimental Materials

In the following, we shortly list the nanoparticles, microbubbles and cells as well as salt and buffered solutions and measurement containers used for our experiments.

Nanoparticles

SO-Mag5 nanoparticles* contain a magnetite core and are covered by *silicon oxide (SO)* and phosphonate groups [57].

*Nanoparticles were kindly provided by O. Mykhaylyk, Institute of Experimental Oncology and Therapy Research, Klinikum rechts der Isar, Technische Universität München

PEI-Mag2/PEI-Mag4 particles* are iron oxide nanoparticles and are covered by *polyethyleneimine (PEI)* combined with a fluorinated surfactant [120].

FluidMag-Strep nanoparticles are magnetite nanoparticles with a streptavidin functionalized starch coating [che].

SHP-30 nanoparticles have a magnetite core with a carboxylic acid surface [oce].

Salt and Buffered Solutions

As buffered solutions *Dulbecco Phosphate Buffered Saline* (*DPBS*, [bio]) and Modified *Hanks Balanced Salt Solution* with sodium bicarbonate (*HBSS*, [sig]) were used. Solutions of salts were produced with double distilled water (Siemens UltraClear [sie]), including sodium chloride (NaCl), calcium chloride ($CaCl_2$) and sodium phosphate. The sodium phosphate solution was produced by equal molar amounts of Na_2HPO_4 and NaH_2PO_4 to achieve an approximately neutral pH and is denoted as $NaHPO_4$ in the following. pH values of the solutions are given in A.3.

Containers

Cell Culture Dishes for the microscopic observation of cells and microbubbles had an inner diameter of 34 mm and were made of *polystyrene (PS)* [tpp].

Cuvettes for size and transmission measurements were standard disposable semi-micro cuvettes made of *polymethyl methacrylate (PMMA)* [bra].

3.3.3 Experimental Methods

All measurements were performed at room temperature and with the following equipment / methods:

Light Transmission measurements of samples were performed either using the custom made measurement device for time sequences in the presence of a magnetic field, or using a Specord 210 light spectrometer [spe] for single measurements in the absence of a magnetic field. For both measurements wavelengths of 470 nm and/or 660 nm were used.

T_2 relaxation values of samples were measured in a 0.5 T *MRI scanner Research Lab* provided with a *magnet 22 MHz* magnet unit and a *drive l* control unit [pur]. T_2 values were measured either once, or over a certain time span every 60 s.

Size Distributions of magnetic nanoparticles and complexes were always determined by dynamic light scattering using a ZetaSizer Nano ZS [zet]. For the number-weighted diameter distribution and its transformation, the refractive index for magnetite of 2.42 [121] was used.

Zeta Potential of nanoparticle suspensions was determined from their electrophoretic mobility using a ZetaSizer Nano ZS and a dip cell (ZEN1002, [zet]). For details on the measurement method of both particle diameter and zeta potential see also chapter 2.1.1.

pH values were measured for different solutions excluding and including nanoparticles with a pH electrode (ScienceLine pH electrode A157 [si]); values are given in A.3.

Magnetization of nanoparticles was measured with a Quantum Design Physical Properties Measurement System [qua]. Here, a few microliters of suspension containing the nanoparticles were filled into glass ampules and dehydrated with a SpeedVac concentrator (SPD111V, [the]). This was repeated several times to accumulate approximately 0.5 mg of nanoparticles. Finally, the ampules were sealed shut and measurements of DC magnetization were performed at a temperature of 300 K and in magnetic flux density fields up to 2 T using an extraction technique. The contributions of the sample holder and the glass ampule we determined separately and subtracted. However, the measurement accuracy did not allow a determination of possible residual remanences which would indicate a ferromagnetic or truly superparamagnetic behavior.

Optical Microscopy was performed using a combination of an inverse microscope (Zeiss Axiovert 200, [zei]) equipped with a digital CMOS camera (Hamamatsu C11440 [ham]).

Characterization of Nanoparticles

In the following, we describe the methods for the characterization of magnetic nanoparticles, microbubbles and cells in suspension. The according results are presented in chapter 4. All measurements were performed at room temperature and carried out in triplicate.

Magnetic Microbubbles with 150 $\mu g\ Fe/ml$ of either SO-Mag5 or PEI-Mag4 nanoparticles[†] were concentrated with the help of a permanent magnet to a fifth of the solution volume and subsequently diluted in a 10 % glycerol solution. The microbubbles were then put into a cell culture dish inside the measurement set-up and instantaneously recorded microscopically.

[†]Magnetic microbubbles were kindly provided by H. Mannell, Walter Brendel Centre of Experimental Research, Ludwig-Maximilians-Universität München

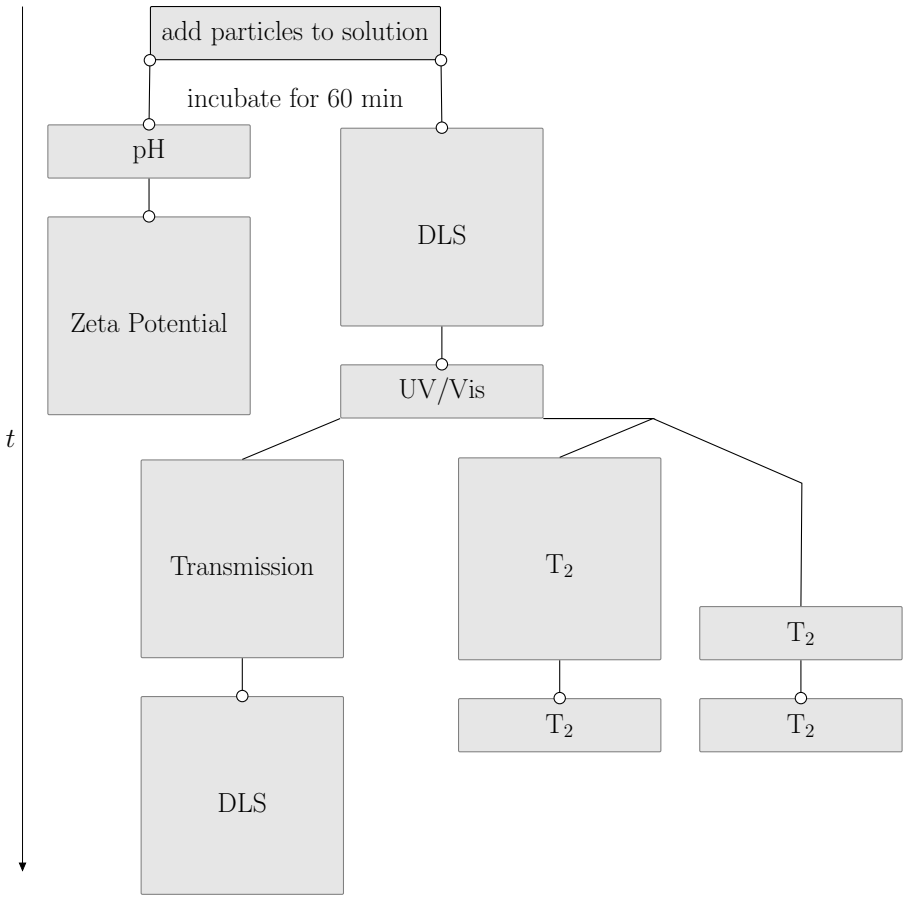

Figure 3.8: Time flow chart for measurements of particle aggregation behavior; circles indicate agitation

Cells of different types, including *embryonic cardiomyocytes (eCMs)*, *embryonic stem cell-derived cardiomyocytes (ES-CMs)* and *bone marrow cells (BMCs)*[‡] were previously fixated and subsequently diluted in PBS to achieve an approximate number of $2.5 \cdot 10^5$ cells per ml. The cells were then put into the cell culture dish inside the measurement set-up and instantaneously recorded microscopically.

Magnetic Nanoparticle Aggregation was measured with several different methods: light transmission and dynamic light scattering for aggregation in absence of a magnetic field and T_2 relaxation and measurements for aggregation in the presence of a magnetic field. The measurements were performed in the sequence depicted in figure 3.8 for different ionic strengths of the salt solutions:

[‡]Cells were kindly provided by the Klinik für Herzchirurgie and Institut für Physiologie 1, Universität Bonn and prepared by A. Ottersbach

- Magnetic Nanoparticles were added to salt or buffered solutions to achieve an iron content of 25 $^{\mu g\ Fe}/_{ml}$ and the suspension was incubated at room temperature for 60 minutes. Afterwards, the particle suspensions were agitated using a vortex mixer for approximately 10 s.
- The pH value of the suspension including nanoparticles was measured.
- The zeta potential was determined from the electrophoretic mobility and the size distribution was determined by dynamic light scattering with 100 runs per measurement.
- The transmission of the sample was measured with an UV/Vis spectrometer at a wavelength of 470 nm. Measurement results are shown in reference to the solution without nanoparticles.
- Subsequently, the particle suspension was again agitated and the sample was divided into three samples. Two samples, each with 200 µl of suspension were used for MRI measurement, while the third sample was measured in our custom measurement device.
- One of the 200 µl samples was put into the 0.5 T MRI system for 25 min, while the other was kept on the bench as control sample. The T_2-relaxation time was measured every 60 s; after 25 min, the sample was removed and the T_2-relaxation time of the control sample was measured. Subsequently, both samples were agitated for 10 s and measured again.
- The third sample was put into the custom device and the light transmission was measured for 30 min at 660 nm. Subsequently, the sample was again agitated and the size distribution was measured a second time.

4

Characterization of Nanoparticles

Magnetic nanoparticles are characterized by several different properties as described in chapter 2.1. A full characterization of magnetic nanoparticles includes the main properties like size, zeta potential and magnetic moment as well as several additional properties, e.g. the composition of coating and core. In the following chapter, we primarily focus on the magnetic characterization of nanoparticles.
As already described in chapter 2.1.2, the measurement of the magnetic moment of nanoparticles, microbubbles or cells can be difficult and often yields unsatisfying results for the purpose of simulations. The methods described in chapter 2.1.2 focus on the magnetization of the particles or the magnetic moment of a bulk of particles. In contrast to most of the mentioned methods, we are interested in the magnetic moment of the individual nanoparticles in the respective medium. Additionally, we aim to design a simple set-up of a manageable size which can be used in any laboratory and moved without problem from one location to another between individual measurements.
In the following we introduce a method which is able to measure the magnetic moment of magnetic nanoparticles, complexes, microbubbles and cells. Based on the previously explained Halbach cylinders, we developed two similar methods to measure the magnetic moment of nanoparticles and complexes as well as microbubbles and cells. Both methods are based on the observation of the movement of the concerning objects under well-defined conditions. Particles, complexes, microbubbles or cells are added to a fluid in a high, but homogeneous magnetic flux density gradient field. Thereby, a homogeneous movement of the objects is assured. We observe the movement via light transmission or optical microscopy and are able to draw conclusions about the magnetic moment of the object.
In the last part of this chapter, we address the behavior of nanoparticles in different types of salt solutions in absence and presence of a magnetic field. Nanoparticles aggregate in different salt solutions depending on their surface coating and zeta potential as well as the ionic type and strength of the corresponding solution. We compare the particle properties and investigate the aggregation behavior of the nanoparticle types used in this work for different salt and buffered solution with several independent measurement methods.

4.1 Magnetic Moment of Cells and Microbubbles

Due to their size, cells and microbubbles can be observed very effectively using optical microscopy. This allows us to directly observe the movement and behavior of the individual objects. Magnetically labeled cells or microbubbles are positioned inside a well-defined magnetic gradient field as shown in figure 4.1. In contrast to previous works by Chalmers, Zborowski or Häfeli [56, 64, 65], we measure the diversion of the nanoparticles in an otherwise static environment for superparamagnetic particles. Therefore, our magnetic set-up is designed for a homogeneous field gradient and involves an array of several permanent magnets.
Henceforth, we refer to the tracked cells and microbubbles simply as objects since this method is not generally limited to those two types of carriers, but applicable to any magnetically labeled object of an appropriate size range. The objects and their movement due to the magnetic force is recorded over a certain time span. Subsequently, we process the resulting image sequence and reconstruct the trajectory of the objects. This allows us to determine the properties of the observed cells and microbubbles.
To evaluate the recorded images concerning object size and velocity, we use a custom tracking algorithm. Though there are many particle and cell tracking algorithms freely or commercially available [122, and references therein], most of those [e.g. 123, 124] are meant to track only small distances and non-overlapping trajectories, e.g. for tracking Brownian motion or morphodynamic behavior. Therefore, they often perform poorly when applied to problems with large distances between individual particle locations. Other packages are able to track in three dimensions [e.g. 125, 126] or are overly complex for our application. Therefore, we created our own cell and microbubble tracking algorithm. To this purpose, we use a set of basic algorithms and combine them in a new way to a stable and fast tracking algorithm which reliably traces the object movement.

4.1.1 Magnetic Set-Up

The set-up for the observation of cells or microbubbles is described in chapter 3.1.1. As shown in figure 3.4a, it consists of a circle of permanent magnets surrounding a cell culture dish. The whole set-up is placed under an inverted microscope. Previous to the measurement, the radial position is marked on the bottom of the cell culture dish. The vertical position of the inner bottom of the cell culture dish can be changed in 1 mm steps from 1.5 mm above the bottom level of the magnets to 8.5 mm. The dish has to be filled with approximately 1 ml of fluid to achieve a homogeneous level of the fluid. This adds another 0.8 mm, so that we approximate the medium position of the object with 2 to 9 mm in 1 mm steps. In general, a higher position of the cell culture dish is preferable, since this coincides with a higher magnetic flux density and a higher and more homogeneous magnetic gradient. However, often the variability of the microscopes optics is limited and a lower position has to be chosen. Additionally, due to the limited space available under a microscope, the height of

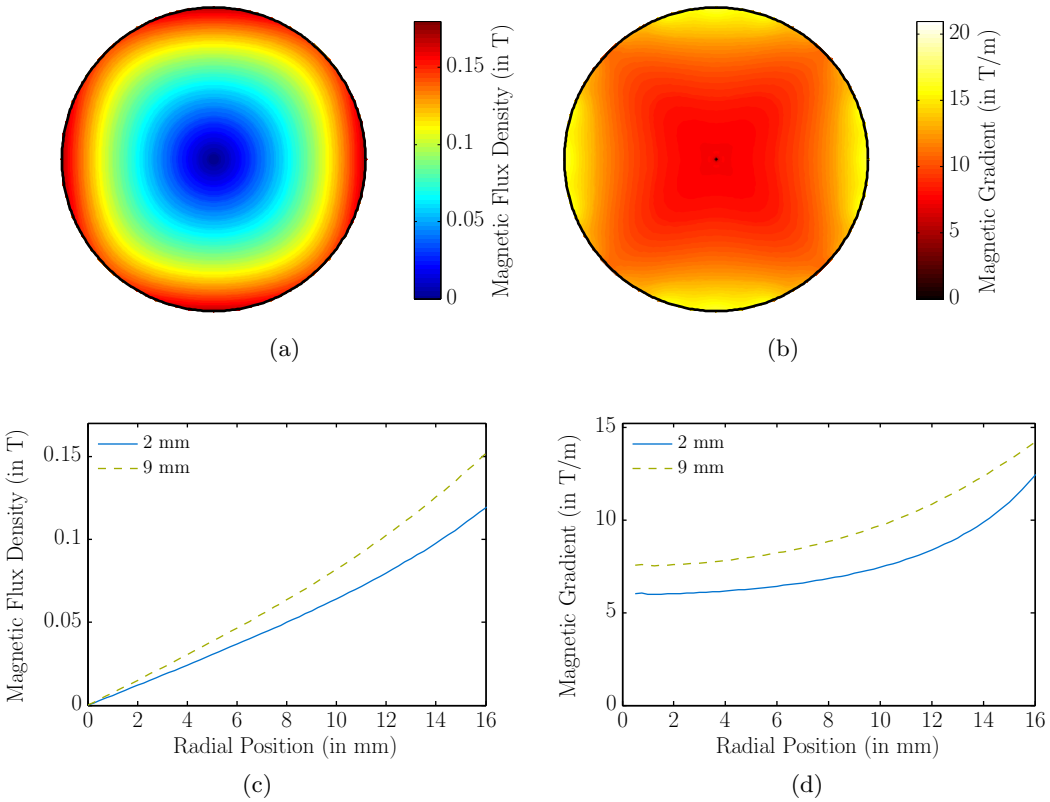

Figure 4.1: Magnetic flux density (a, c) and gradient of magnetic flux density in radial direction (b, d) inside the cell culture dish, in the horizontal plane at the highest position (a, b) and as a radial cut for the lowest and highest position (c, d)

the magnets is too small in reference to the diameter of the set-up to produce a truly constant magnetic gradient. The respective boundary effects influence and attenuate the magnetic field inside the set-up, so the magnetic flux density does not increase exactly linearly at the vertical center of the set-up. The magnetic gradient in the radial direction is therefore only approximately linear. Figure 4.1 shows the magnetic flux density (a, c) and the magnetic gradient (b, d). Panel a and b show the magnetic density and gradient in the plane perpendicular to the axis at a height of 9 mm. Figures 4.1c and d show those quantities as a cut in radial direction for the lowest and highest position (2 mm and 9 mm). If we assume an infinite height of the magnets for this set-up, we would obtain a magnetic gradient of 12 $^{\mathrm{T}}/_{\mathrm{m}}$ which coincides roughly with a magnetic gradient of 13.3 $^{\mathrm{T}}/_{\mathrm{m}}$ as approximated by equation 3.5. However, due to the limited height of the magnets, we achieve only a magnetic gradient of approximately 7.8 $^{\mathrm{T}}/_{\mathrm{m}}$ at the vertical center of the set-up.

4.1.2 Measurement and Evaluation

The magnetically labeled objects in solution are placed into a cell culture dish which is subsequently placed into the magnetic set-up. The set-up is then positioned under an inverted microscope and the movement of the objects is recorded. It is recommendable to choose a position close to the center but not at the center, e.g. at a radial position of 6 mm, where there is a very homogeneous magnetic field gradient. Ideally, the time step of the recording should be chosen in such a way that the distance covered by the objects between each frame is in the same range or smaller than the object diameter, so that the objects overlap slightly. Thereby, the covered distance is also smaller than the distance between individual objects of the same image. Measurements have shown that the optimal recording speed for cells and microbubbles lies at about 4 fps and should not be less than 1 fps. This means, that we record an image sequence with 0.25 seconds between the individual images. To evaluate the recorded images concerning object size and velocity, we use a custom tracking algorithm which we present in the following.

Tracking Algorithm

The previously recorded images are evaluated with the algorithm visualized in figure 4.2. The left column (I) describes the algorithm itself, while the middle column (II) is an exemplary excerpt of an image or image sequence, respectively. The right column (III) depicts a numeric representation of the image or resulting data. Our algorithm consists of several parts which in turn consist of one or several steps indicated by the circled numerals in the first column of figure 4.2. The first part loads and filters the image data. It is based on the IDL particle tracking algorithm by Crocker *et al* [127–129] and is explained in step 1. The second part finds all object positions in all images and is represented by step 2 and 3. In the next part, the connections between the individual objects in the images are found and the trajectories are reconstructed in step 4. Finally, in the last part (step 5) the trajectory data is evaluated. The individual steps of the algorithm are explained in more detail in the following.

1. The selected images are imported into MATLAB and converted into gray scale. An example image is shown in figure 4.3a. Depending on the coloring of the image, the color spectrum has to be inverted to achieve bright objects on a dark background, e.g. in case of microbubble microscopy (figure 4.3b). Based on the approximate object size $\mathcal{W}$, e.g. obtained by the microscopy software, and a freely chosen noise level $\mathcal{N}$, the images are band-pass filtered. The filter applies convolutions of the image matrix with a gaussian and a rectangular

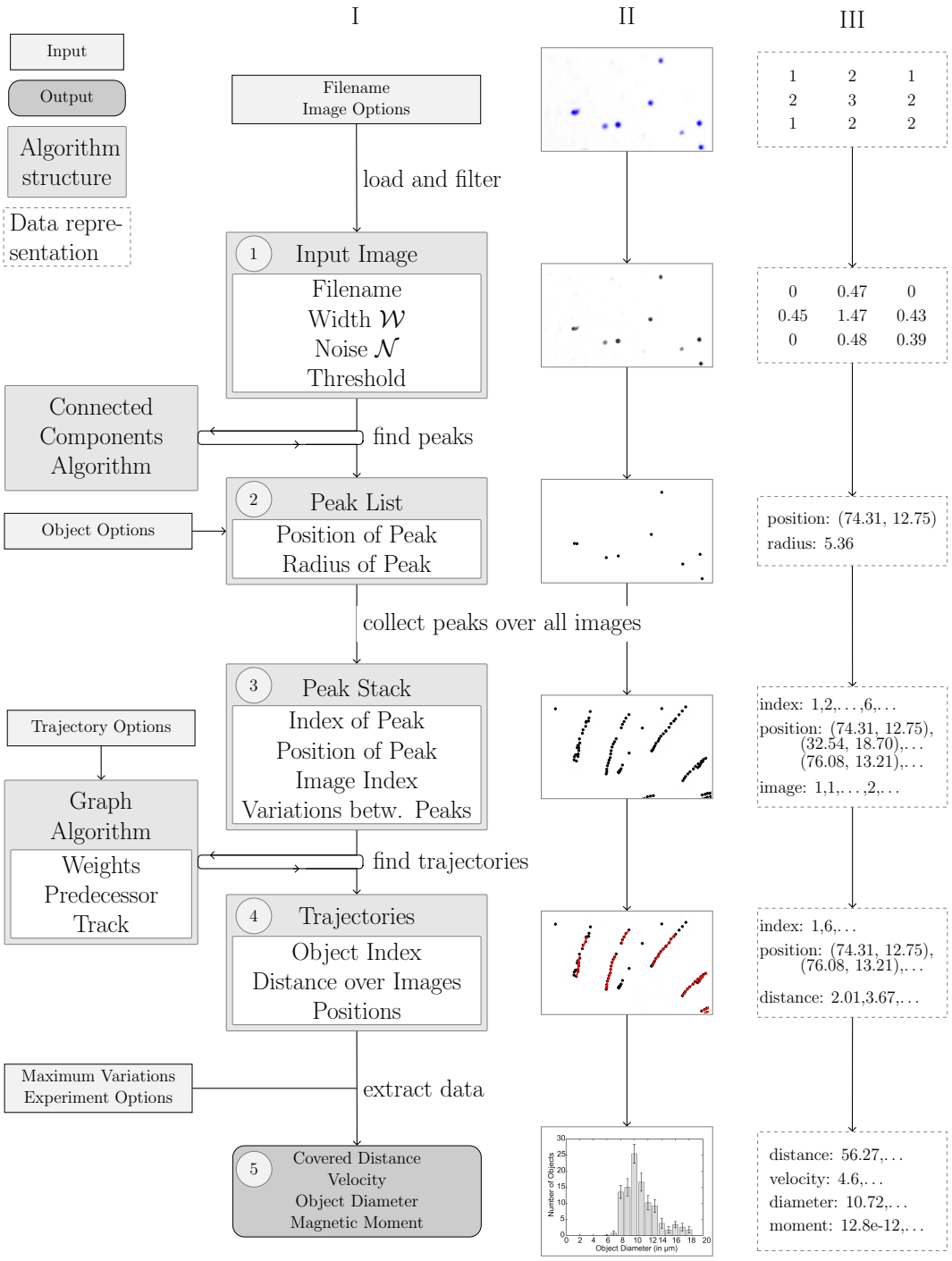

Figure 4.2: Schematic description of tracking algorithm for cells and microbubbles: the left column (I) describes algorithm, the middle column (II) is an exemplary excerpt of an image or image sequence and the right column (III) depicts a numeric representation; circled numerals correspond to the steps described in the text

filter

$$\mathcal{F}_{\text{gauss}}(\vec{x}) = \frac{1}{f_{\text{gauss}}} \exp\left(-\frac{\vec{x}^2}{2\mathcal{N}^2}\right) \tag{4.1a}$$

$$\begin{aligned}\mathcal{F}_{\text{rect}}(\vec{x}) &= \frac{1}{f_{\text{rect}}} \text{rect}\,(2\mathcal{W}+1) \\ &= \begin{cases} \frac{1}{2\mathcal{W}+1} & \text{if } -\frac{2\mathcal{W}+1}{2} \leq |\vec{x}| \leq \frac{2\mathcal{W}+1}{2} \\ 0 & \text{else} \end{cases}\end{aligned} \tag{4.1b}$$

where $f_{\text{gauss,rect}}$ are normalization factors and rect is the rectangular or boxcar function. The difference between applying both filters individually smoothes the image and subtracts the background [127–129]. The resulting image is shown in figure 4.3c. Afterwards, we apply a freely chosen threshold, see figure 4.3d.

2. In the next step, the objects are located. Here, the appearance of cells and microbubbles differs in the center of the object. While the investigated cells are displayed as filled circular shapes under the microscope, microbubbles are shown as ringlike shapes with varying widths, as shown in figure 4.5c. The objects are located with the help of a connected-component algorithm [130, 131]. Here, all connected pixels are collected and assigned to an object, see figure 4.3e. To better illustrate the process, the example image was rescaled to represent an object with only a few pixels in width.
   To locate the connected pixels, the image is scanned for non-zero pixels. If such a pixel is found, it is marked with an identification number and subsequently removed from the image. This is repeated for the four cartesian neighbors of the original pixel until no neighbors with a non-zero value remain. In figure 4.3e, the start pixel in the upper left corner is indicated by a white arrow. Subsequently, all neighboring pixels are found, as indicated by the different symbols. The colored arrows represent the individual steps where the non-zero neighbors are located until the final pixel is found, again indicated by a white arrow. All pixels marked with a certain identification number then belong to the same connected object. The next found object receives a new identification number. Overlapping and touching objects are recognized as one larger object as long as they are directly connected by at least one pixel. In contrast to the often described version on binary data, we perform this algorithm on the thresholded gray scale datasets. This offers further possibilities in distinguishing touching objects.
   In the following, $\mathcal{P}_n$ denotes the set of all pixels k associated with the object with the identification number n, while $\mathcal{B}_m$ denotes the individual images. The intensity-weighted centroid $\vec{c}_n$ of the found objects n and the distance r_k from each pixel k of the object $\mathcal{P}_n$ to the centroid

$$\vec{c}_n = \frac{\sum\limits_k \mathcal{I}(\vec{x}_k)\vec{x}_k}{\sum\limits_k \mathcal{I}(\vec{x}_k)}\,, \tag{4.2a}$$

$$r_k = \|\vec{c}_n - \vec{x}_k\|\,, \tag{4.2b}$$

are calculated for all $k \in \mathcal{P}_n$. Here, $\mathcal{I}(\vec{x}_k)$ is the intensity of the pixel k at the position described by $\vec{x}_k$.
To calculate the object radius, a sobel filter is applied. Thereby, the edge of the object is obtained as shown in figure 4.3f. On the sobel-filtered image $\mathcal{S}_m$, we calculate the radius R_n of the object

$$R_n = \frac{\sum\limits_k \mathcal{I}_\mathcal{S}(r_k) r_k}{\sum\limits_k \mathcal{I}_\mathcal{S}(r_k)} \,, \tag{4.2c}$$

by calculating the weighted arithmetic mean of the distance r_k of the (outer) edge from the centroid for $k \in \{k \in \mathcal{S}_m | \, \overline{r_k} < r_k < \max\big(r_k\big)\}$. The calculation of the mean value is again weighted by the intensity, or rather the intensity $\mathcal{I}_\mathrm{s}$ of the sobel filtered image $\mathcal{S}_m$ which can be interpreted as the intensity gradient of the original image. We limit the selection of edge pixels, on the one hand, by taking only those pixels into account which have a larger distance than the mean distance of all object pixels. Thereby, we discard the inner edge in case of microbubbles. On the other hand, we remove those edge pixels at a larger distance than the maximum distance of the object pixels, thereby limiting the influence of other objects in close proximity. The resulting centroid and radius are also shown in figure 4.3f in reference to the sobel filtered image and in figure 4.3g in reference to the original microscope image.
Finally, we filter the found objects by allowing only a certain size range

$$R_\mathrm{min} \leq R_n \leq R_\mathrm{max} \,. \tag{4.3a}$$

This removes too large or too small objects (equation 4.3a). We also allow only those objects whose total area is in good agreement with their reconstructed radius (circularity condition)

$$\left| \frac{R_n^2 \pi}{N_k} - 1 \right| < \Delta_A \,, \tag{4.3b}$$

$$\frac{\overline{\mathcal{I}}(k_R)}{\overline{\mathcal{I}}(k)} > \Delta_I \,, \tag{4.3c}$$

where $k_R \in \{k \in \mathcal{P}_n | \, r_k < R_n\}$ or $k_R \in \{k \in \mathcal{P}_n | \, {}^{R_n}\!/_4 < r_k < R_n\}$ in case cells or microbubbles, respectively. N_k is the number of pixels $k \in \mathcal{P}_n$. In case of microbubbles, we additionally limit the objects to those with a black center of minimum size

$$\frac{r_k}{\min\big(k\big)} < \Delta_C \,. \tag{4.3d}$$

Figure 4.5a exemplarily shows a microscopy image and the objects found by our algorithm with their corresponding size denoted as blue circles. Typical values for the maximum/minimum allowed parameters Δ can be found in table 4.1b.

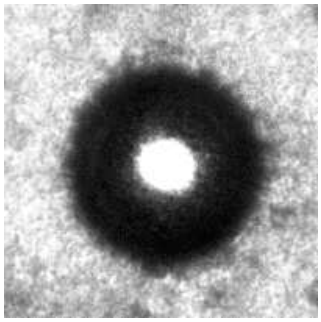

(a) Microscopy image,

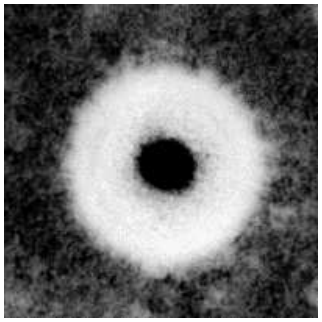

(b) image after inversion,

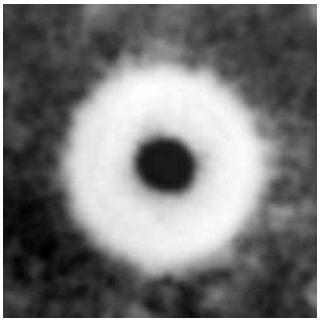

(c) after filtering

(d) and after application of a threshold;

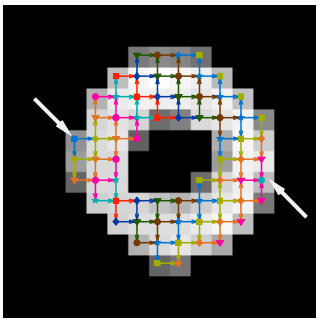

(e) Detection of connected components: start and final pixel are indicated by white arrows; detection proceeds along colored arrows.

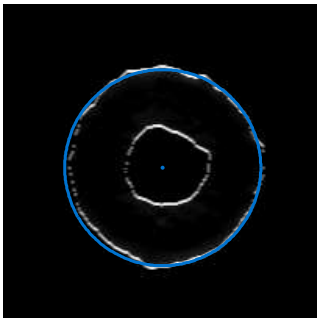

(f) Sobel filtered image with centroid and radius indicated by blue line and dot

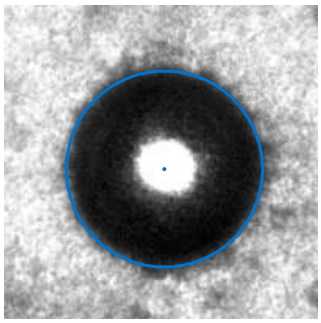

(g) and centroid and radius indicated by blue line and dot compared to original image;

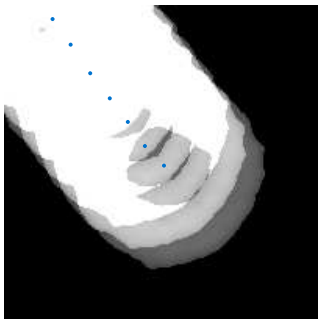

(h) Overlay of several images and centroids of located objects

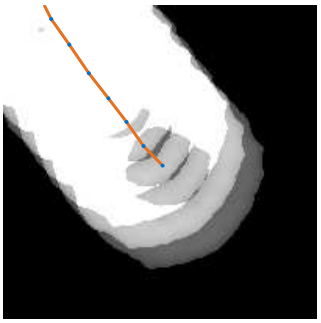

(i) and reconstructed trajectory denoted by orange line

Figure 4.3: Individual steps of the tracking algorithm on the example of a microbubble; the image is imported (a), if necessary inverted (b), filtered (c) and a threshold is applied (d); subsequently the object positions are located (e) with centroid and radius (f, g) collected over all images (h) and the trajectories are reconstructed (i)

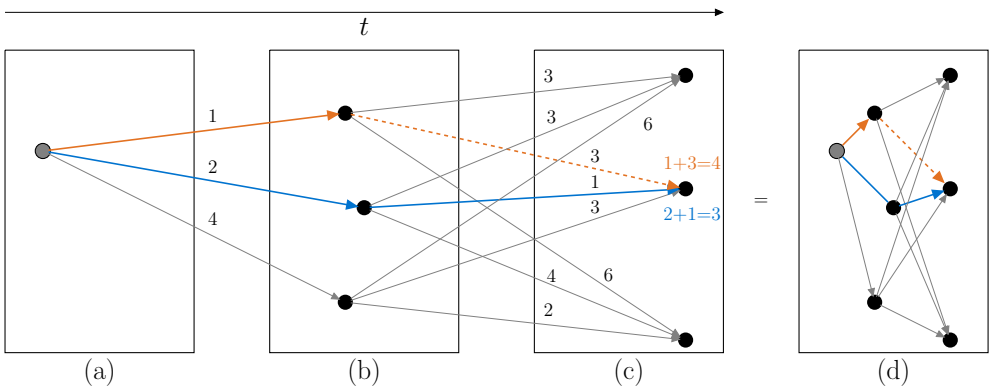

Figure 4.4: Schematic description of graph algorithm for a sequence of three subsequent images (a-c); arrows denote edges between objects with their according weights noted above them; panel (d) shows an overlay of panel (a) to (c)

3. The found objects are then collected into a single dataset including a reference to the originating image. A set of several found objects in close proximity is shown as blue dots in figure 4.3h, including an overlay of the corresponding filtered images. For the purpose of the reconstruction of the trajectory, we beforehand calculate the weights for the connections between all objects located in neighboring images $\mathcal{B}_m$ and $\mathcal{B}_{m+1}$. Those connections are called edges. The weights for those edges include the absolute distance s_{np} and the relative radius ΔR_{np} of any two objects

$$s_{np} = \|\vec{x}_n - \vec{x}_p\| \,, \tag{4.4a}$$

$$\Delta R_{np} = \left| \frac{R_n}{R_p} - 1 \right| \,, \tag{4.4b}$$

where $n \in \mathcal{B}_m$ and $p \in \mathcal{B}_{m+1}$. To judge the angle of the trajectory, we first calculate the angle between all objects of neighboring images relative to the cartesian coordinates x and y. The relative angle $\Delta\varphi_{np}$ for each edge is then defined in reference to the most often occurring angle Φ over the complete image set

$$\varphi_{np} = \operatorname{atan}\left(\frac{y_n - y_p}{x_n - x_p} \right) \,, \tag{4.5a}$$

$$\Phi = \max\left(H\left(\varphi_{np} \right) \right) \bmod 180^\circ \,, \tag{4.5b}$$

$$\Delta\varphi_{np} = \frac{\varphi_{np}}{\Phi} \,, \tag{4.5c}$$

where $n \in \mathcal{B}_m$ and $p \in \mathcal{B}_{m+1}$ and $H(\varphi_{np})$ denotes the histogram over the angles φ_{np}. However, we cannot distinguish between backward and forward angles, since the direction of the previous edge is yet unknown.

Parameter	Value
Minimum diameter	$0.5 \cdot \mathcal{W}$
Maximum distance	$10 \cdot \mathcal{W}$
Minimum track length	5
Graph weight distance G_s	1
Graph weight radius G_r	1
Graph weight angle G_φ	2

(a)

Parameter	Value
Δ_C	5
Δ_A	0.3
Δ_I	0.65

(b)

Parameter	Value
Maximum angle	30°
Maximum angle std	45°
Maximum radius std	0.5
Maximum distance std	0.5

(c)

Table 4.1: Typical parameters used for input (a, compare steps 1-3), peak identification (b, compare step 2) and optimization (c, compare step 4) of trajectory reconstruction

4. The object positions are subsequently traced throughout the image sequence by a Dijkstra graph algorithm [132]. The algorithm searches for the best path to any connected object based on a single source object. In our case, the edges of the graph algorithm are directed and limited to neighboring images, while, additionally, the distance an object can cover between two images is limited. Figure 4.4 shows a schematic description of the utilized structure. Panels (a) to (c) denote individual images, while panel (d) shows an overlay of those three images. All edges between objects of neighboring images are assigned a weight value which can be based on different quality ratings. For the schematic, we simply chose the distance as a weight parameter. The edges between the objects are plotted as arrows with their weight denoted above them. Starting from one individual object in figure 4.4a, all objects in the next image are assigned a value identical to the weight of the corresponding edge between the starting object and itself (figure 4.4b). The edge with the smallest weight value is indicated by an orange arrow. This edge connects the start object to the closest object in the next image. Continuing from this closest object, we repeat the previous step for all objects in the third image (figure 4.4c). However, we assign a distance value corresponding to the sum of the distances between all three objects. This step is repeated for all other objects of the second image. The resulting distance value is updated if it is

smaller than the previous one. Thereby, instead of the path indicated by the orange arrows, the best path is described by the blue arrows, since the total of their weight is smaller.
In our algorithm, the edges are weighted by the absolute distance, the relative radius of two objects and the angle of the path as denoted in equations 4.4 and 4.5. For this purpose, all three properties are calculated beforehand as described above. The ratio of the three weights $G_{s,r,\varphi}$ can be chosen freely and is highly dependent on the object size, covered distance and distance between the objects and neighboring paths. Typical parameters can be found in table 4.1a. The path finding is performed for every object of the first image and all objects of the subsequent images which are not already included in a previously found path. Figure 4.3i again shows the superimposed image data and corresponding objects, additionally to the reconstructed trajectory.
After finding all available best paths, those trajectories are checked for plausibility by comparing the properties of the objects belonging to a trajectory. This includes, on the one hand, comparing the radius and distance between all objects, and, on the other hand, comparing the angles of the segments of each trajectory. If only a few objects of the trajectory do not fit the specifications, the trajectory is split at the corresponding point into several individual trajectories. Figure 4.5b exemplarily shows an overlay of a series of filtered microscopy images and a number of trajectories found by our algorithm.

5. The remaining trajectories can then be evaluated concerning covered distance, velocity and size. From the positions throughout the image sequence, the recording frame rate and the scale, the velocity and the size of the objects can be deduced. Thereby, we can draw conclusions about the magnetic moment of the objects using equation 2.41. Neglecting acceleration and all minor forces, we can use the one-dimensional equation

$$\mu_{\mathrm{sat}} \mathcal{L}(B(r)) \nabla_r B(r) = 3\pi\eta d_h \, v_r \,, \tag{4.6}$$

to estimate the magnetic moment μ at the radial position r. To evaluate the magnetic moment, we use a χ^2-fitting procedure as described in chapter A.1.3. For this purpose, we combine the data points $R_{t,m}$ and $s_{t,m}$ to their product

$$y_{t,m} = R_{t,m} \cdot s_{t,m} \,, \tag{4.7}$$

where $R_{t,m}$ denotes the radius of the object belonging to one trajectory t and the image $\mathcal{B}_m$ and $s_{t,m}$ is the distance covered by the object between images $\mathcal{B}_m$ and $\mathcal{B}_{m+1}$. Using equation 4.6, the model function $\mathcal{M}$ and χ^2 read

$$\mathcal{M} = \mu \mathcal{L}(B(r)) \cdot \frac{\nabla B \Delta t}{6\pi\eta} = \mu \cdot c \,, \tag{4.8a}$$

$$\chi^2 = \sum_m \left(\frac{y_{t,m} - \mu_t \cdot c}{\sigma_{t,m}} \right)^2 \tag{4.8b}$$

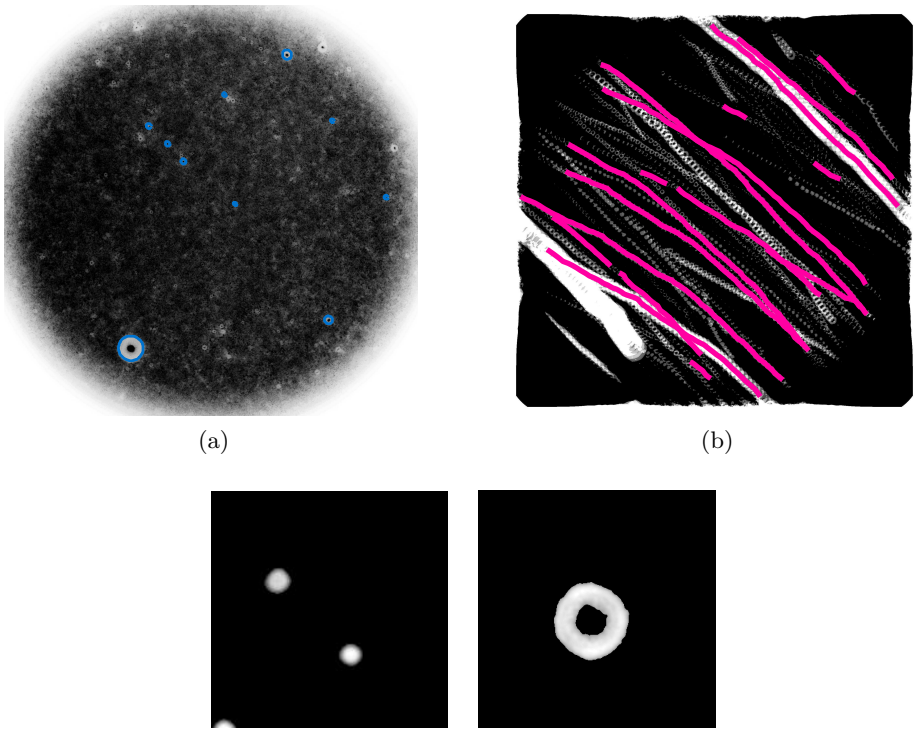

(a) (b)

(c)

Figure 4.5: The first image of a sequence of microscopic images of microbubbles loaded with SO-Mag5 nanoparticles (gray scale) with the reconstructed objects encircled (blue) (a); an overlay of the series of filtered images (gray scale) and the trajectories reconstructed by the algorithm (pink); comparison of a filtered image of cells (c, left side) and microbubbles (c, right side)

with μ as the free parameter. Minimizing expression 4.8b results in an error weighted mean value for the magnetic moment of the objects of one trajectory

$$\mu_t = \frac{1}{c} \frac{\sum\limits_m \frac{y_{t,m}}{\left(\sigma^y_{t,m}\right)^2}}{\sum\limits_m \frac{1}{\left(\sigma^y_{t,m}\right)^2}} \,. \tag{4.9a}$$

For the estimation of the error σ^y on the observable y, we assume an error $\sigma^{s,R}$ of 1 px for the distance and object radius. Further assuming a complete correlation between both errors, we gain [118]

$$\frac{1}{\left(\sigma^\mu_t\right)^2} = c^2 \sum_m \frac{1}{\left(\sigma^y_{t,m}\right)^2} \,, \tag{4.9b}$$

$$\left(\sigma^y_{t,m}\right)^2 = \left(\sigma^{s,R}\right)^2 \left(s_{t,m} + R_{t,m}\right)^2 \,. \tag{4.9c}$$

4.1.3 Performance of the Algorithm

To verify the results of our tracking algorithm, we performed systematic tests of the recognition rate and computation time of the algorithm for different sets of input images. To this purpose, we generated sets of images with different object and trajectory properties as well as different numbers of objects.
As image size, we chose 128×128 px with 20 images per sequence. The mean object diameter $\bar{d}$ was always set to 5 px and the number of objects per image was varied as indicated by the object density. Here, one object per image corresponds to an object density of 0.12 % and 100 objects per image correspond to 12 %. The generated objects were allowed to touch, but not to overlap. The recognized objects were compared to the previously created objects by position and subsequently, the trajectory composed of those objects was investigated. Here, a fully connected trajectory was rated higher than multiple fragmented pieces of a trajectory.
We varied several object and trajectory properties. While the mean object diameter $\bar{d}$ was kept constant, the distance $\bar{s}$ between objects of a trajectory was varied in multiples of the object radius. This is equivalent to changing the frame rate of the recording. For this purpose, we defined the frame rate corresponding to covered distance of $\bar{s} = \bar{d} = 5$ px between images as f_0. Additionally, we varied the deviation of the object properties for objects belonging to the same trajectory $\Delta r_t, \Delta s_t$, Δs_t and between objects of different trajectories ($\Delta r_n, \Delta s_t$, Δs_n) as well as the angle of the trajectory ($\Delta\varphi_n$, $\Delta\varphi_n$). The standard deviation for those variations was set to 20 % of the mean value. Furthermore, we disabled and enabled the individual weights used for the graph algorithm.

Figure 4.6 shows the results for object and trajectory recognition as well as mean object distance and computing time. Colors, line style and markers are explained in the bottom panel of figure 4.6. While the color of the plot lines indicates the distance between objects in a trajectory, the line style denotes the different weights for the graph algorithm. If only the continuous plot lines are shown, as in figure 4.6a, c, e, this means that the result is mainly independent of the trajectory reconstruction and different weights and deviations lead to comparable results.
Figure 4.6a shows the amount of recognized objects. Since the object recognition is performed independently of the trajectory reconstruction, this result does not depend on the weights of the graph $G_{s,r,\varphi}$ or the distance of the objects in a trajectory. As expected, the recognition of the objects decreases with increasing object number, since the objects tend to overlap more and more, and no longer fulfill the requirements (compare equation 4.3) for object recognition. At an object density of 15 %, less than 20 % of the objects are recognized. Figure 4.6c shows the mean object distance in relation to the object distances of a trajectory. The results listed in chapter 4.1.4 are obtained for mean object distances between 0.5 and 2.5 times the object diameter and object densities in the range between 0.5 and 2 %, so we are in a region where the algorithm performs well. In figure 4.6c, the progression of the computing time can be seen. The main load of the algorithm is located in the object

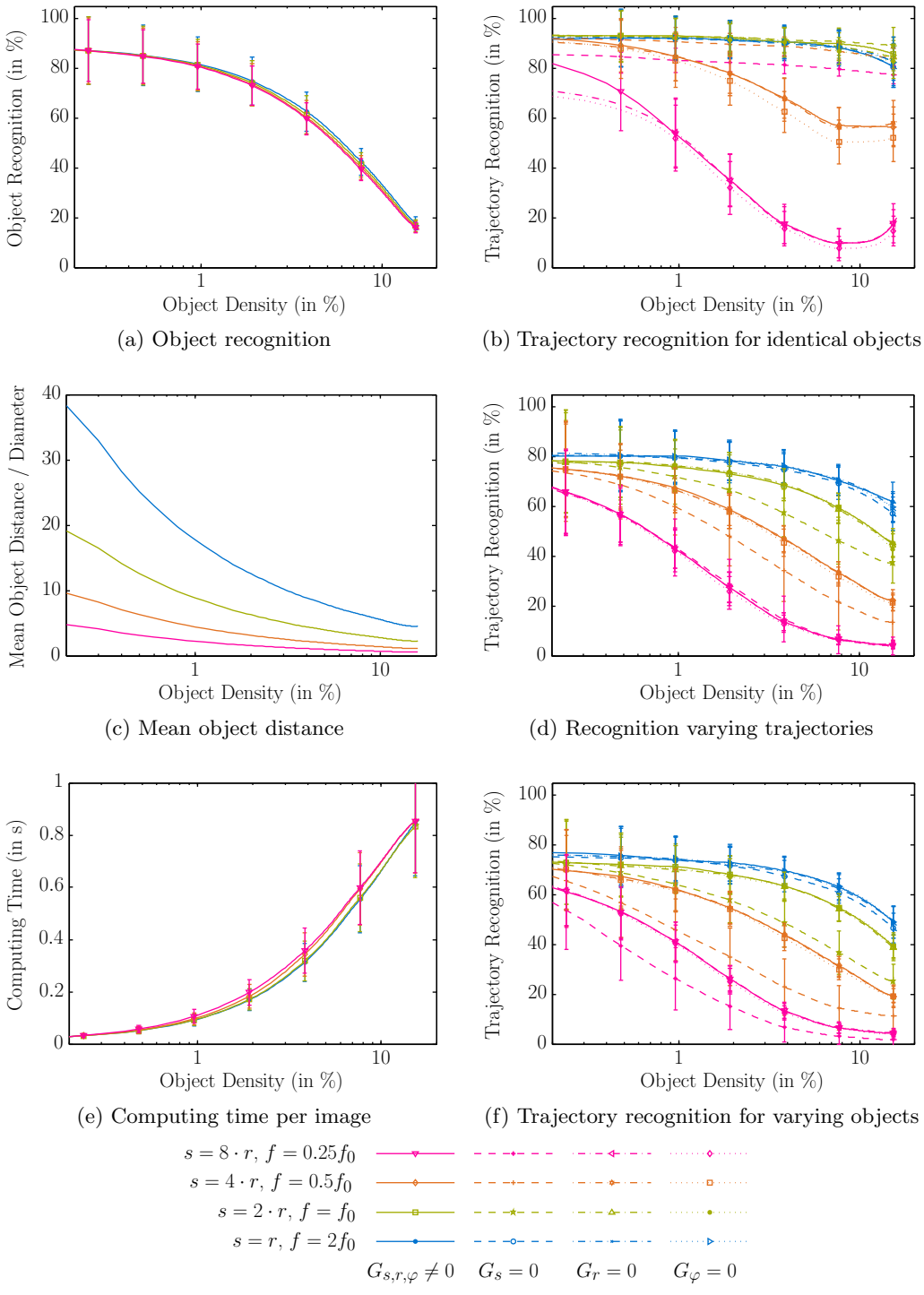

(a) Object recognition

(b) Trajectory recognition for identical objects

(c) Mean object distance

(d) Recognition varying trajectories

(e) Computing time per image

(f) Trajectory recognition for varying objects

Figure 4.6: Performance of the cell tracking algorithm in dependence of object density in the image: ratio of recognized objects (a), mean distance between objects in terms of object diameter (c), computing time per image (e) as well as ratio of trajectory recognition relative to ratio of object recognition for different properties (b, d, e) and legend for all plots

recognition, since every bright pixel has to be identified and assigned. Thereby, the computing time mainly depends on the object density and image size and not on the actual trajectory recognition. The displayed times are given as elapsed real time on one core of an Intel Xeon E5520 processor. Since we evaluate only the performance of the trajectory reconstruction, the evaluation of the movement (step 5) is not included in the computing time.
Figures 4.6b, d, f show the amount of recognized trajectories relative to the amount of recognized objects. While figure 4.6b shows the trajectory recognition for identical objects, moving with same speed in the same direction, figure 4.6d shows the result for trajectories of varying objects, with different size, velocity and direction. However, the object properties within individual trajectories remain constant. Finally, in figure 4.6f, the trajectory recognition for objects whose properties within a trajectory were varied is shown. This might represent objects drifting slightly out of focus and back, or vibrations causing blurring or lateral displacement. It can be seen that, independent of the graph weights, an object distance in the range of the object size or smaller leads always to a higher trajectory recognition. As expected, the success rate of the trajectory recognition decreases with increasing object density and decreasing frame rate. In the special case of identical objects, moving with same speed in the same direction (figure 4.6b), the weight on the distance G_s constrains the recognition rate, since the distance is the most unspecific feature in this case. The recognition rates remain comparably constant over the different distances / frame rates. The distance weight is far more important for trajectories where the objects vary between trajectories, but not inside them. The reconstructions with $G_s = 0$ in figure 4.6d show less success than other weight combinations for small and medium object distances. Additionally, the recognition rate is generally lower and decreases faster than the recognition rates in figure 4.6b. If the individual objects of a trajectory vary, the recognition rate decreases further and the influence of the distance weight increases.

4.1.4 Results

We performed several measurements with the above described set-up. In table 4.2, we list the results for object diameter, velocity, magnetic moment and surface magnetization. Values are given as mean value and standard deviation. Figure 4.7 shows the results exemplarily for two different cell types. The first column of panels (figure 4.7a, c, e) shows the results for live BMCs, while the second column (figure 4.7b, d, f) shows the same for ES-CMs. Figure 4.7a and b show the reconstructed diameter. The calculated magnetic moment and surface magnetization are shown in figure 4.7c, d and e, f, respectively. The individual panels show the histogramatic data for approximately 570 trajectories in case of the BMCs and nearly 1600 trajectories in case of the ES-CMs, including the calculated errors as described above. The trajectories were extracted from 1250 images each. Additionally, we show the distribution fitted to the data which we later use in our simulations (see chapter 5.2.1).

Object Type	Nanoparticle	Diameter Velocity	Magnetic Moment Surface Magnetization
Microbubbles	$2.5\,\mathrm{pg\ Fe/MB}^{\dagger\dagger}$	$4.1 \pm 1.1\,\mu\mathrm{m}$	$103 \pm 40.7\,\mathrm{fAm^2}$
	SO-Mag5	$19.1 \pm 8.6\,\mu\mathrm{m/s}$	$3.7 \pm 0.6\,\mathrm{mA}$
Microbubbles	$2.5\,\mathrm{pg\ Fe/MB}^{\dagger\dagger}$	$3.8 \pm 1.7\,\mu\mathrm{m}$	$60.2 \pm 47.1\,\mathrm{fAm^2}$
	PEI-Mag4	$11.4 \pm 4.8\,\mu\mathrm{m/s}$	$2.5 \pm 1.1\,\mathrm{mA}$
BMC	$20\,\mathrm{pg\ Fe/cell}$	$9.4 \pm 2.5\,\mu\mathrm{m}$	$333 \pm 435\,\mathrm{fAm^2}$
(bone marrow cells)	SO-Mag5	$40 \pm 59\,\mu\mathrm{m/s}$	$1.7 \pm 2.0\,\mathrm{mA}$
eCM (embryonic	$200\,\mathrm{pg\ Fe/cell}$	$9.6 \pm 1.5\,\mu\mathrm{m}$	$225 \pm 313\,\mathrm{fAm^2}$
cardiomyocytes)	SO-Mag5	$23 \pm 38\,\mu\mathrm{m/s}$	$1.3 \pm 1.9\,\mathrm{mA}$
ES-CM (embryonic stem	$200\,\mathrm{pg\ Fe/cell}$	$9.3 \pm 1.8\,\mu\mathrm{m}$	$694 \pm 256\,\mathrm{fAm^2}$
cell derived cardiomyoc.)	SO-Mag5	$99 \pm 36\,\mu\mathrm{m/s}$	$2.9 \pm 1.3\,\mathrm{mA}$

Table 4.2: Results of measurements for cells and microbubbles as mean value and standard deviation of the fitted distribution; eCMs and ES-CMs were provided as fixated cells, while BMCs were live cells

††Iron amount of microbubbles was calculated based on a mean microbubble density of $60 \cdot 10^6\,\mathrm{MB/ml}$

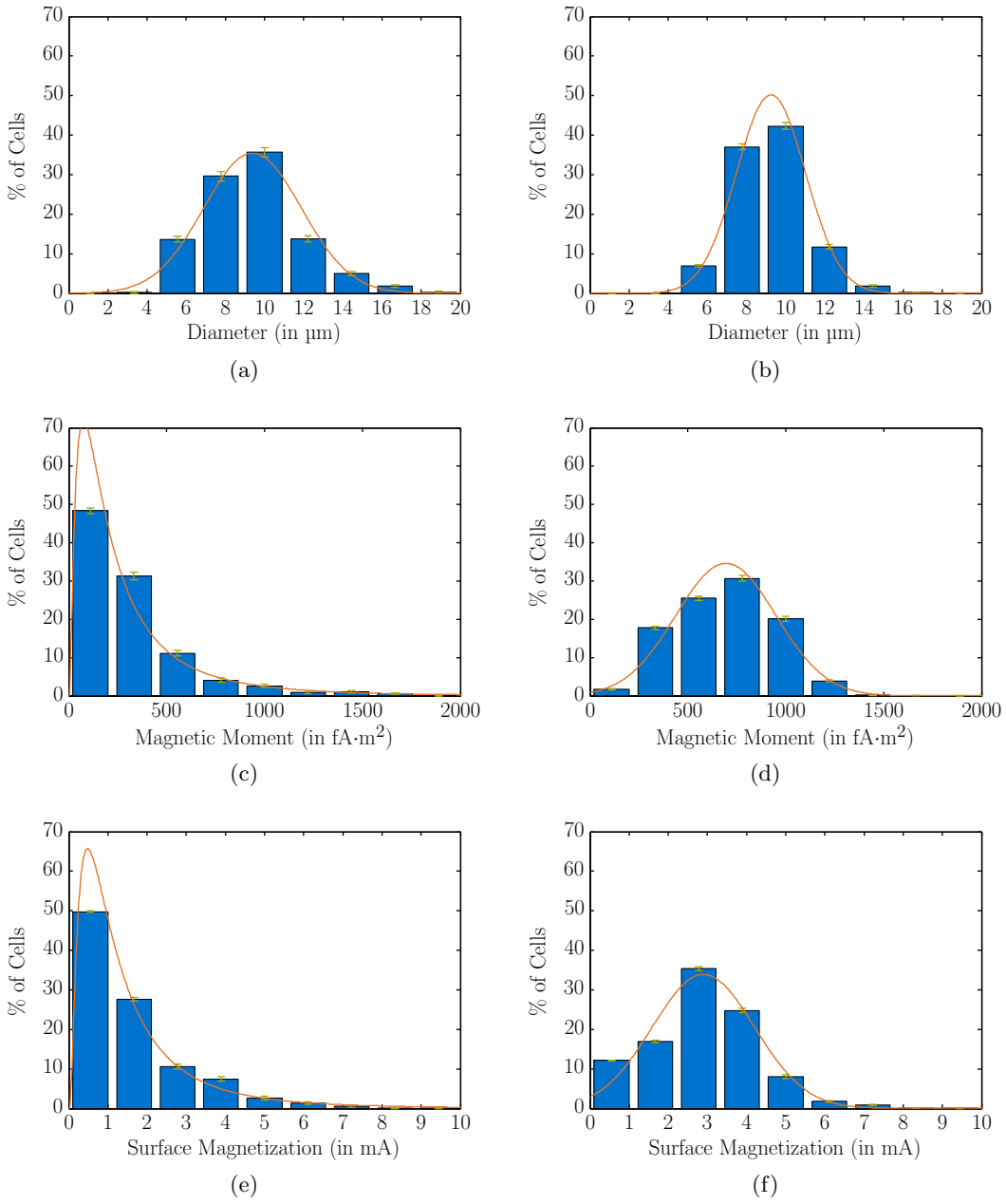

Figure 4.7: Representative data from trajectory reconstruction of live BMCs (left column) and fixated ES-CMs (right column): diameter of cells (a, b) as well as calculated magnetic moment (c, d) and magnetization (e, f); the data evaluated from the microscopy images is displayed as blue bar plots with green error bars; the fitted distribution is shown as red line

4.2 Magnetic Moment of Nanoparticles

Though magnetic nanoparticles and nanoparticle complexes can be observed under a microscope, it is difficult to evaluate those results automatically. Furthermore, the equipment necessary for this measurement might not always be available under the required conditions, e.g. in a S2 laboratory. Therefore, we adjusted the set-up to observe nanoparticles indirectly via the optical transmission of the fluid. The nanoparticles and complexes move towards the magnetic field source and thereby away from the observation point. Due to this movement, the optical density of the fluid decreases and the transmission increases over time at the measurement location. From this behavior, we can estimate the particle movement and draw conclusions about the magnetic moment.
Though a comparable approach to determine the magnetophoretic mobility of nanoparticles by measuring the optical density of a fluid was already mentioned by Mykhaylyk *et al* [76, 77], we improved the magnetic as well as the measurement set-up and, furthermore, developed an enhanced evaluation of the optical density.

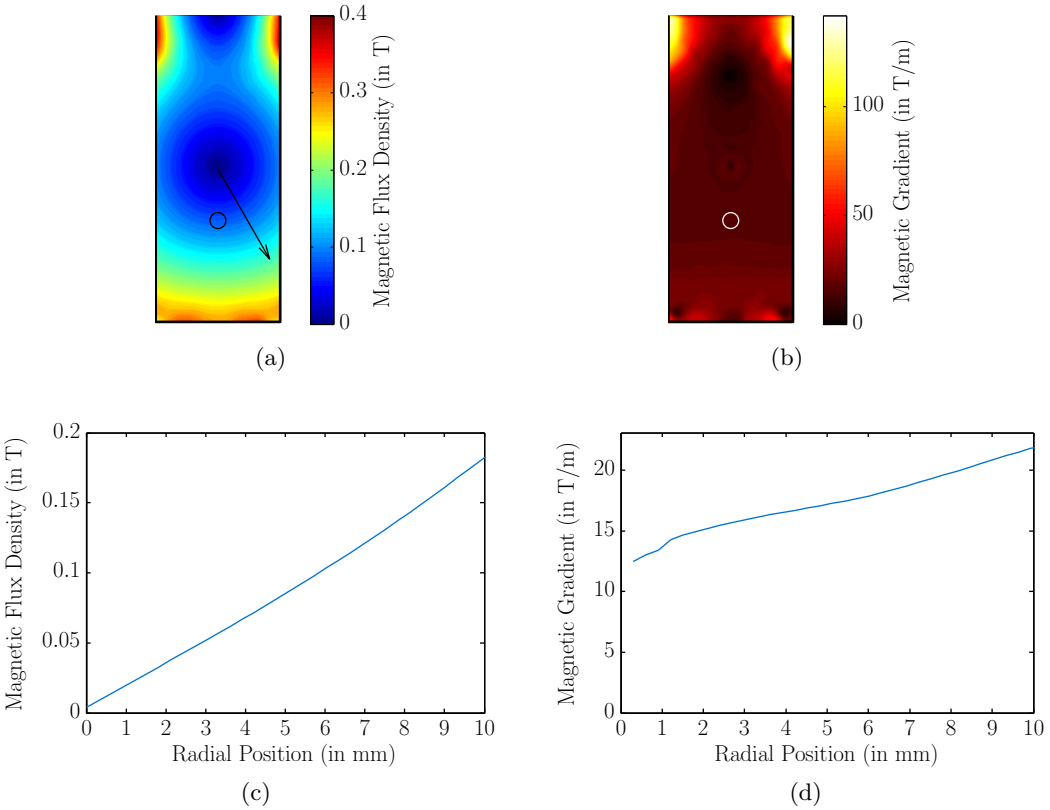

Figure 4.8: Resulting magnetic flux density field (a, c) and magnetic gradient (b, d) of measurement set-up in the central plane inside the cuvette (a, b) and in radial direction from the center of the magnet circle to the cuvette bottom (c, d)

4.2.1 Magnetic Set-Up

The set-up for the measurement of magnetic nanoparticles is described in chapter 3.1.1. As shown in figure 3.4b, it consists of several permanent magnets arranged in an incomplete circle. Figure 4.8 shows the magnetic flux density (a, c) and the magnetic gradient (b, d) of the set-up. Figures 4.8c and d show those quantities as a cut in radial direction. The radial direction is defined from the center of the circle of permanent magnets outward, as indicated by the arrow in figure 4.8a. The location of the observation window is indicated by the black or white circle in figure 4.8a and b, respectively.
Due to the limited height of the magnets in this set-up, we achieve a magnetic gradient of approximately 16.1 $^{\mathrm{T}}/_{\mathrm{m}}$ at the observation window. If we assume an infinite height of the magnets, we would obtain a magnetic gradient of 21 $^{\mathrm{T}}/_{\mathrm{m}}$ which coincides very well with magnetic gradient approximated by equation 3.5 of 20.8 $^{\mathrm{T}}/_{\mathrm{m}}$. Due to the same reasons, the magnetic flux density increases not completely homogeneously over the volume. In the lower half of the circle however, the magnetic flux density field increases approximately linearly with the radius. The magnetic gradient in the radial direction increases only about 1 to 1.5 % per millimeter.

4.2.2 Measurement and Evaluation

Measurement

The measurement and evaluation principle are schematically shown in figure 4.9 and 4.12, respectively. Magnetic nanoparticles in solution are put in a standard cuvette

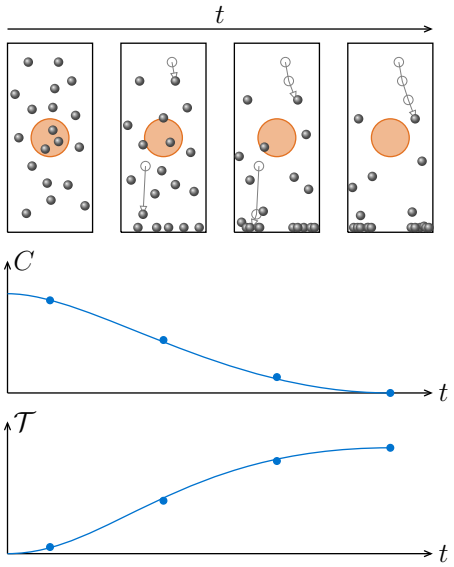

Figure 4.9: Principle of measurement: a sample with nanoparticles at four different times during a measurement and the corresponding concentration and transmission curves; the observation window is indicated by the red circle; sizes are not to scale

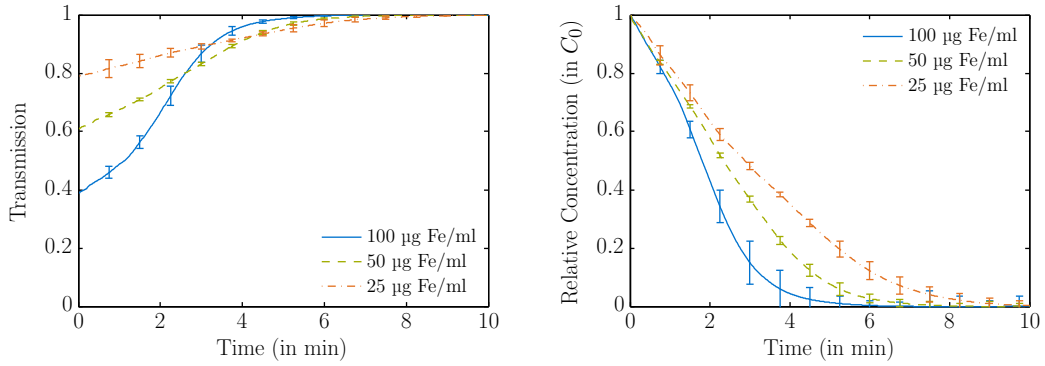

(a) (b)

Figure 4.10: Transmission (a) and transformed concentration (b) curves for different concentrations of SO-Mag5 nanoparticles in HBSS; error bars are displayed only for a few points

and placed in the measurement set-up. For more information about the set-up, see chapters 3.1.1 and 3.3.1. The top row of figure 4.9 shows the sample at four different times during the measurement. The observation window is indicated by the red circle and the corresponding concentration and transmission curves are shown below the samples. Due to the magnetic force, the nanoparticles move in outward direction as indicated by the arrow in figure 4.8a. The direction of movement is indicated by gray arrows for selected particles. The concentration C of nanoparticles in the observation window decreases with advancing nanoparticle movement. Thereby, the transmission $\mathcal{T}$ of the suspension at the measurement location increases over time. The transmission value is recorded for a certain amount of time and curves similar to the ones shown in figure 4.10a are gained.
The curve is recorded until no change in the transmission is visible and we can assume that all particles have moved away from the observation window. At this point we measure only the optical density of the medium. We define this final intensity value as $\mathcal{I}_0$. Figure 4.10a shows the recorded transmission curves for different concentrations of SO-Mag5 nanoparticles in HBSS at a wavelength of 660 nm.

Calibration

Additionally to the recorded time dependency of the light transmission of the particle suspension in the presence of the magnetic gradient field, we need to determine the correlation between the transmission / absorbance and the nanoparticle concentration. To this end, a calibration curve is recorded with the optical density measurement device of choice and an exponential or linear fit is applied to the transmission or absorbance, respectively. An exemplary calibration curve can be seen in figure 4.11 for SO-Mag5 nanoparticles in HBSS at 470 nm and 660 nm. While figure 4.11a shows the exponential decrease of the light transmission, figure 4.11b shows

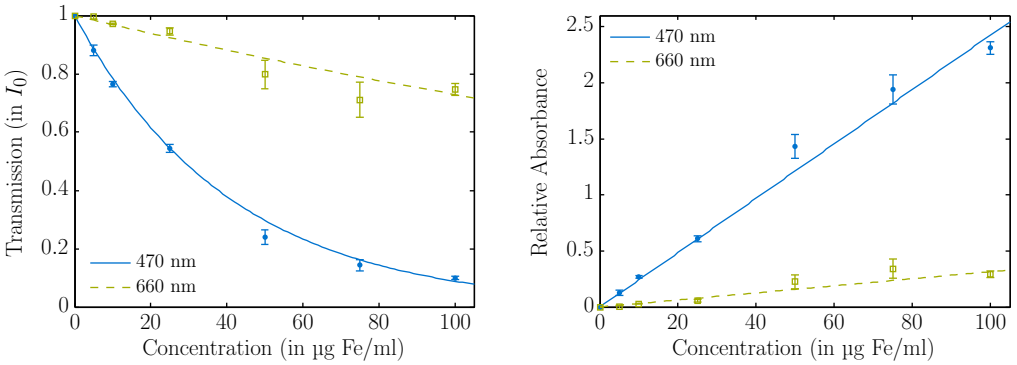

(a) Transmission (b) Absorbance

Figure 4.11: Relative transmission and absorbance for different concentrations of SO-Mag5 nanoparticles in HBSS: dots denote experimental values and line describes exponential (a) and linear (b) fit for transmission and absorbance, respectively

the linear increase of the absorbance. We are thereby able to determine the extinction coefficient ϵ, compare also equation 2.42.
With this calibration, the transmission curve can be transformed into a relative concentration. Figure 4.10b shows the calculated concentration over time corresponding to the transmission values in figure 4.10a.

Evaluation

Figure 4.12 shows the evaluation principle of the measured transmission curves. The left column symbolizes the experimental results, while the right column depicts the corresponding simulation. The measured transmission curves (Experiment II) in figure 4.10a can be transformed into concentration curves with the help of the calibration (Experiment I) shown in figure 4.11. The resulting concentrations (Experiment III) are shown in figure 4.10b.
To evaluate those curves, we aim to duplicate the experimental result in a simulation. Therefore, we calculate the trajectories of a number of particles (Simulation II) based on equation 2.41 and the size distribution of the sample (Simulation I). Subsequently, we evaluate the particle density per time step in the observation window. To compensate for the different intensities caused by the polydispersity of the nanoparticles, the particles are weighted by their respective absorption cross sections, compare equation 2.44. We are then able to reproduce the transmission curves of the experimental results (Simulation III). For a given set of input conditions, we can match the shape of the curves from experiment and simulation and thereby determine the value of the magnetic moment as a parameter.
For magnetic nanoparticles and complexes, we assume a constant ratio of magnetic moment to volume and thereby a constant magnetization. For the purpose of the evaluation, we therefore use the magnetization as a free parameter to determine the magnetic moment of the particles.

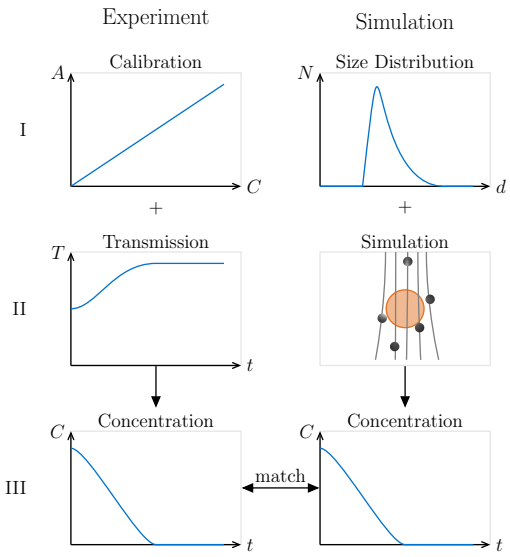

Figure 4.12: Principle of evaluation; left column depicts evaluation of experimental data, while right column denotes simulation of the same data; magnetization is determined by matching experimental result with simulation

Impact of Input Parameters

There are several input parameters which can influence the results of the measurement and simulation. Apart from the magnetic flux density and gradient which are static in this set-up, there are viscosity and aperture as parameters on the experiment side as well as density, magnetization and size distribution on the particle side. The size distribution in turn consists of mean value and variance. Additionally, we show the impact of gravity and Langevin behavior. To investigate the influence of those parameters on the shape of the concentration curve, we simulate each parameter variation separately. Figure 4.13 shows the concentration curves for the parameters listed in table 4.3 (denoted by "no variation") as well as for the individually changed parameters.
First, we study the influences on a monodisperse distribution with particles in saturation. Subsequently, we investigate the influence of polydisperse size distributions and Langevin behavior. The gained concentration curves can be fitted to the weighted superposition of an exponential function and a linear function

$$C(t) = w_{\mathcal{E}} \exp\left(-a \cdot t^2 - b \cdot t\right) + (1 - w_{\mathcal{E}})(1 - c \cdot t) \cdot \mathcal{H}\left(\frac{1}{c} - t\right), \tag{4.10}$$

with the positive parameters $a \geq 0, b \geq 0, c \geq 0$ and the weight $0.8 \leq w_{\mathcal{E}} \leq 1$. While the parameters a, b, c determine the overall slope of the curve, $w_{\mathcal{E}}$ is responsible for the curvature.
The experimental parameters, density and gravity as well as the particle parameters were varied as follows:

Parameter	Symbol	Default Value
Aperture	δ	$1\,\mathrm{mm}$
Density	ϱ	$2.5\,\mathrm{g/cm^3}$
Diameter	d_h	$500\,\mathrm{nm}$
Volume magnetization	M_V	$50\,\mathrm{kA/m}$
Langevin parameter $\mathcal{L}(\mathcal{E}B)$	$\mathcal{E}$	∞
Viscosity	η	$0.95\,\mathrm{mPa \cdot s}$

Table 4.3: Standard parameters used for evaluation of time dependent transmission measurements

- The device comes with different apertures between 1 and 2 mm in diameter. As can be seen in figure 4.13a the change between the smallest and the largest aperture has no impact on the concentration curve.
- The viscosity of the fluid is largely temperature dependent and usually varies for different solutions between 0.8 and 1.1 mPa · s (compare figure A.5). Those values influence the concentration curve visibly as can be seen in figure 4.13a. The changes correspond to a change in the inferred magnetization of ±10 %.
- The density of the nanoparticles and thereby their mass is another mostly unknown parameter. Figure 4.13b shows the variation between $0.5\,\mathrm{g/cm^3}$ (microbubbles) and $5.2\,\mathrm{g/cm^3}$ (pure magnetite nanoparticles) with and without the consideration of gravitational forces. A change in the particle density leads to only very small changes in the concentration curve, since the magnetic force is dominant.
- As expected, the size of the nanoparticles is one of the most important parameters and has a very large influence on the result. Since a smaller size corresponds to a smaller magnetic moment, the magnetic force on the nanoparticles is smaller and the particles move slower. Figure 4.13c shows that a reduction of the diameter by 50 % results in an approximately four times longer time until all particles are outside of the observation window.
- The other important parameter is the magnetization behavior of the particles, as this is the parameter we want to determine. Though the influence is not as drastic as the diameter, figure 4.13c shows that a reduction of the magnetization by 50 % results in an approximately two times longer travel time for the particles.
- All prior results were given for particles in saturation. The Langevin magnetization behavior changes the magnetic moment and thereby the magnetic force on the particles, depending on their position. This parameter is described by $\mathcal{E}$ as defined in equation 2.9b. In figure 4.13c, we show the result for $\mathcal{E} = 70$

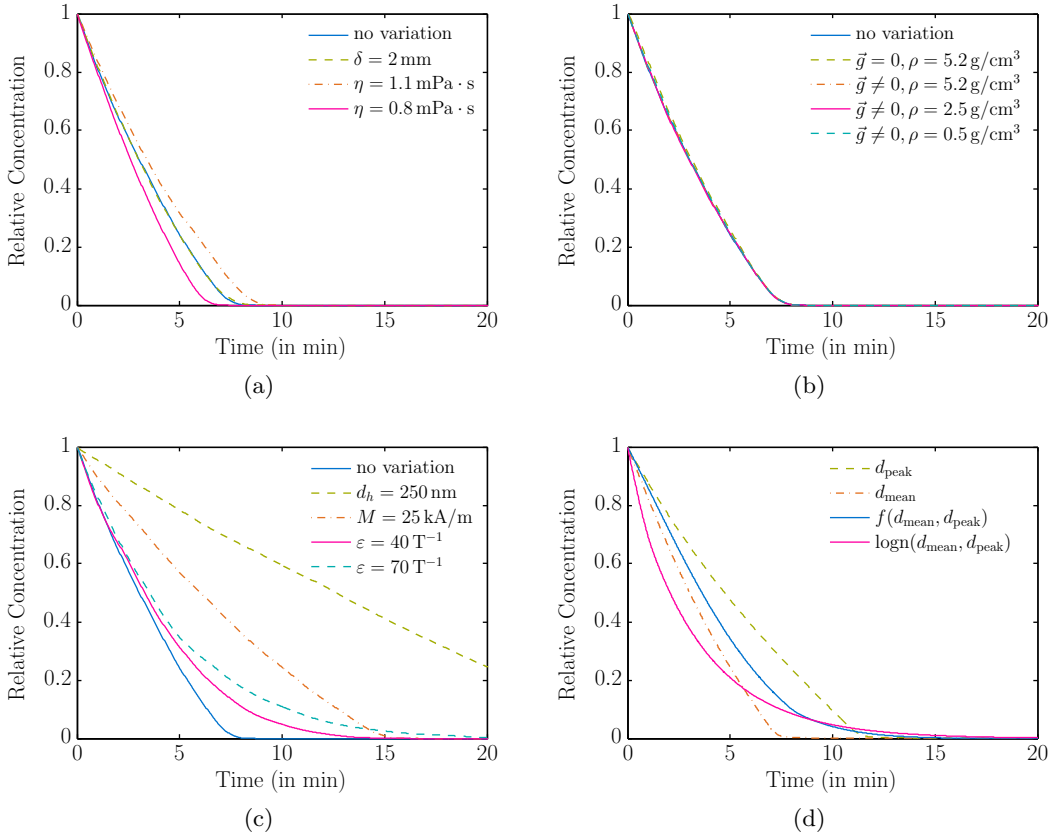

Figure 4.13: Simulated concentration curves for different experimental parameters (a), for variations of density and gravity (b), for different particle parameters (c) and polydisperse particle sizes (d)

($\mu = 0.86\mu_{\mathrm{sat}}$ at $B = 0.1\,\mathrm{T}$) and $\mathcal{E} = 40$ ($\mu = 0.75\mu_{\mathrm{sat}}$ at $B = 0.1\,\mathrm{T}$), which corresponds to the approximate values for the particle types used in the experiments, e.g. $\mathcal{E}(\text{SO-Mag5}) \approx 70$ and $\mathcal{E}(\text{PEI-Mag2}) \approx 40$. Though the initial slope of the curve is similar, this parameter results in a more rounded curve and the weight parameter $w_{\mathcal{E}}$ approaches 1. For a higher $\mathcal{E}$, the concentration curve is closer to the one of the saturated particles. A change in the Langevin parameter slows the movement of the particles considerably, especially those close to the center of the set-up.

- Finally, we apply a size distribution for the particle diameter. Figure 4.13d shows the concentration curves for two individual diameters as well as a bidisperse and a lognormal size distribution, all with the same volume magnetization. For a better intuitive understanding, we did not vary the variance of the distribution directly, but the peak value of the distribution as defined in chapter A.1.2. The mean diameter d_{mean} of the distribution is 500 nm as in the previous steps, while the peak value d_{peak} of the distribution is 400 nm.

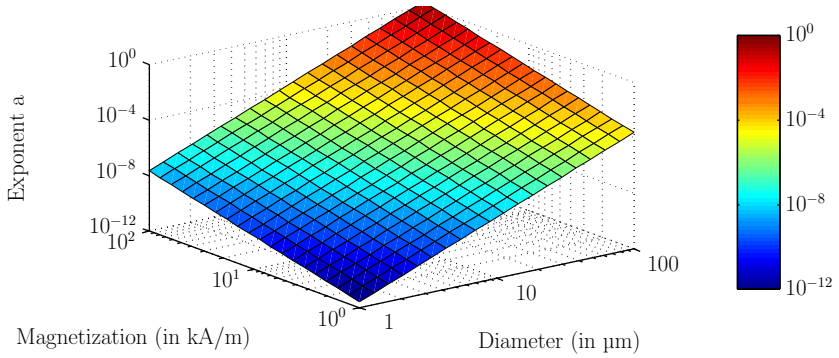

Figure 4.14: Progression of the exponents of equation 4.10 for a range of diameters and magnetization values

This corresponds to a standard deviation of 200 nm.
Additionally to the results for monodisperse particles with d_{mean} and d_{peak}, figure 4.13d shows the concentration for a bidisperse distribution with peaks at d_{mean} and d_{peak} weighted with 0.46 and 0.54. This proportion corresponds to their relative occurrence in a lognormal distribution.
The shown curves for polydisperse distributions can no longer be approximated by a single exponential function, but consistent with equation 2.45 by a superposition of the individual exponential functions C_i with $i = 1, \ldots, N$. For this purpose, we can bin the size distribution into N segments on the 99.73% interval around the mean value. For an adequate description, the number N of divisions should be of order 100. The overall concentration is then given by

$$C(t) = \sum_{i=1}^{N} w_i \, C_i(t) \tag{4.11a}$$

$$w_i = \frac{1}{V} \sum_{L_i \leq d_i < L_{i+1}} \sigma_{E,i} \cdot N_i \,, \tag{4.11b}$$

$$L_i = \exp\big(\mu - 4\sigma\big) + \frac{\exp\big(\mu + 4\sigma\big) - \exp\big(\mu + 4\sigma\big)}{N - 1}(i - 1) \,, \tag{4.11c}$$

where L_i denotes the lower boundary of the bin i. The sum over all weights w_i adds up to 1 to ensure physical consistency.

Figure 4.14 exemplarily shows the progression of the fit parameter a of equation 4.10 for different magnetization and diameter values. The parameter can be described by a 1×1 polynomial of the logarithmic parameters

$$\ln\big(a\big) = p_1 \cdot \ln\big(d\big) + p_2 \cdot \ln\big(M\big) + p_3 \,, \qquad \text{or} \tag{4.12a}$$

$$a = d^{p_1} \cdot M^{p_2} \cdot \exp\big(p_3\big) \,. \tag{4.12b}$$

The fit parameters b and c show a similar behavior. Based on the above information, we can approximate the concentration curve resulting from a distribution of nanoparticles for a given magnetization.

Evaluation

Based on the above results, we can provide an initial guess for the magnetization for a given size distribution with known viscosity and Langevin parameter. We then calculate the trajectories as described in the beginning of this chapter and match the gained concentration against the experimental result. To refine the result, we vary the magnetization based on the initial guess and find the best match by a least-squares minimization [133].

4.2.3 Results

We performed several measurements with the described set-up for magnetic nanoparticles and particle complexes. In table 4.4, we list the results for diameter and magnetization. Additionally, figure 4.15 shows the measurement results for the volume magnetization for different iron concentrations of FluidMag-Strep and SO-Mag5 nanoparticles. For orientation, we fitted a constant value and an exponential curve to the data, respectively. While we can fit a constant value within one standard deviation for the measurement results of FluidMag-Strep particles, the results for SO-Mag5 nanoparticles decrease with increasing particle concentration.

Nanoparticle	Iron Concentration	Diameter	Volume Magnetization
SO-Mag5	$10\,\mu g\,Fe/ml$	$430 \pm 79\,\mu m$	$34.9 \pm 3.4\,kA/m$
	$25\,\mu g\,Fe/ml$	$638 \pm 187\,\mu m$	$19.0 \pm 3.2\,kA/m$
	$50\,\mu g\,Fe/ml$	$1108 \pm 324\,\mu m$	$9.3 \pm 3.2\,kA/m$
	$100\,\mu g\,Fe/ml$	$1308 \pm 487\,\mu m$	$4.2 \pm 0.1\,kA/m$
FluidMag-Strep	$10\,\mu g\,Fe/ml$	$279 \pm 123\,\mu m$	$49.8 \pm 13.9\,kA/m$
	$25\,\mu g\,Fe/ml$	$214 \pm 114\,\mu m$	$59.4 \pm 11.4\,kA/m$
	$50\,\mu g\,Fe/ml$	$344 \pm 165\,\mu m$	$42.7 \pm 8.1\,kA/m$
	$100\,\mu g\,Fe/ml$	$464 \pm 226\,\mu m$	$59.1 \pm 28.4\,kA/m$

Table 4.4: Measurement result for custom transmission device for different concentrations of nanoparticles in HBSS; diameter is given as mean value and standard deviation of the fitted distribution over all measurements, while magnetization is given as mean value and standard deviation over individual measurements

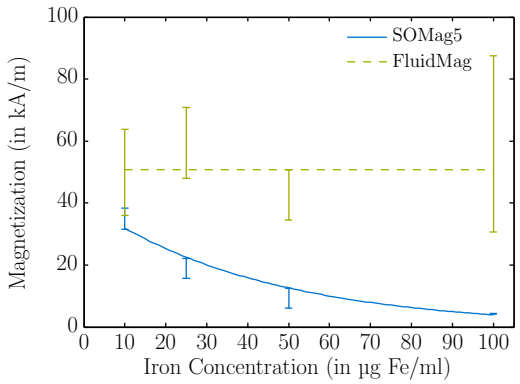

Figure 4.15: Measurement result for custom transmission device for different concentrations of nanoparticles in HBSS

4.3 Particle Aggregation

Depending on the solution in which the nanoparticles are suspended, they are stable or form aggregates. Many nanoparticle types show a different aggregation behavior for different solutions and thereby exhibit different complex sizes depending on the solution. To investigate this behavior, we analyzed the aggregation of SO-Mag5 and PEI-Mag2 nanoparticles in different salt solutions, like sodium chloride, calcium chloride and sodium phosphate as well as in the buffered solutions HBSS with calcium and magnesium and DPBS. We compare several methods of measurement which let us estimate the size and aggregation state of the individual nanoparticles or complexes, respectively, in the absence as well as in the presence of a magnetic field. The used methods include light transmission, dynamic light scattering and zeta potential measurements. For an investigation of this behavior in a homogeneous magnetic field, we use magnetic relaxation measurements and transmission measurements for results in an inhomogeneous magnetic field.

The figures in the following chapter show measurement results for different suspensions of SO-Mag5 nanoparticles. Measurements at different ionic strengths of salt solutions like sodium chloride (NaCl), calcium chloride ($CaCl_2$) and sodium phosphate (denoted as $NaHPO_4$ in the following figures) were performed. The resulting values are plotted in dependence on the ionic strength of the solution, while water and buffered solutions are inserted at their total ionic strengths, compare table A.3. We assume that aggregation sets in at a certain ionic strength I_{c_-} and saturates at I_{c_+}. The results of each measurement for a certain salt were fitted onto a model function

$$\begin{aligned}\mathcal{M}(I) = {} & \mathcal{H}(I_{c_-} - I) \cdot y_1 + \mathcal{H}(I - I_{c_+}) \cdot y_2 \\ & + \frac{1}{I_{c_+} - I_{c_-}} \left((y_2 - y_1) \cdot I + I_{c_+} y_1 - I_{c_-} y_2 \right) ,\end{aligned} \tag{4.13}$$

where $\mathcal{H}(x)$ is the Heaviside function and $y_{1,2}$ are the measurement values for the not aggregated and aggregation saturated state, respectively. In other words, the model function consists of three parts. The first part describes a constant value y_1 until the aggregation process starts at I_{c_-}, followed by a linear slope in the second part until the aggregation process saturates at I_{c_+}. The third part again describes a constant value y_2. We define a third value I_{c_m} which describes the ionic strength at the center between the not aggregated and aggregation saturated state as

$$I_{c_m} = \mathcal{M}\left(\frac{I_{c_+} - I_{c_-}}{2} \right) . \tag{4.14}$$

This model function has no physical or chemical motivation, but matches our experimental findings quite well and is solely used to describe and compare the aggregation behavior. We performed similar experiments for PEI-Mag2 nanoparticles. We do not present those results as images, but only indicate them in the text.

4.3.1 Influence of Ionic Strength and Valence

Figure 4.16 shows the result for light transmission, zeta potential and hydrodynamic diameter measurements. The vertical lines in the lower area of figure 4.16b indicate the corresponding ionic strength of the prior mentioned salts in the buffered solutions. Measurements in purified water and buffered solutions, like DPBS and HBSS, were only taken at the natural concentration and are plotted at the value of their total ionic strength.
Figure 4.16a depicts the measured zeta potential values for all salt solutions. The according pH values are shown in table A.3. However, the zeta potential measurements for higher ionic strength are to be treated with reserve, since the measurement method is not suited for high ionic strengths. The high conductivity arising from the high ionic strength, is accompanied by a high current and a subsequent heating. Additionally, high ionic strengths collapse the electrical double layer, thereby making it more difficult to measure. However, the zeta potential for SO-Mag5 particles in water lies at approximately $-28\,\mathrm{mV}$, while the zeta potential for PEI-Mag2 nanoparticles is approximately $+42\,\mathrm{mV}$.
Figure 4.16b shows the result for light transmission for the particle suspensions at 470 nm in reference to the corresponding solution without nanoparticles. It can be seen that, based on the initial value in purified water, the transmission decreases. For the salt solutions, the starting point of this decrease is highly dependent on the salt concentration or ionic strength. For calcium chloride suspensions, the decrease of the transmission starts almost immediately, while the transmission of the sodium chloride suspension is stable up to approximately 10 mM. For sodium phosphate, the transmission decreases not until an ionic strength of over 100 mM. In contrast to those results, PEI-Mag2 particles are stable up to 1 M of sodium chloride solutions and aggregate fastest in sodium phosphate solutions.
Since the light transmission of a particle suspension for a certain particle concentration is dependent on the particle size [134, 135], the results shown in figure 4.16b are in good agreement with figure 4.16c and d. Figure 4.16c exemplarily shows the size distribution of nanoparticles in calcium chloride solutions with different ionic strengths. In figure 4.16d, the diameter of the nanoparticles in the different suspensions are shown in the form of the mean value and standard deviation of the intensity distributions. The particle diameter is stable for small salt concentrations and increases considerably with the ionic strength until a stable value is reached. It can be seen in figures 4.16b and d that the critical ionic strength $I_{c\_}$ at which the nanoparticles start to aggregate is different for each of the used salts.

The sedimentation velocity for the measured salt concentrations can be calculated as described in equation 2.32. In the not aggregated state, the nanoparticles have a velocity of approximately $50\,\mu\mathrm{m/h}$ which is negligible within the time of the experiment. The fully aggregated nanoparticles have velocities of approximately $10\,\mathrm{mm/h}$ which corresponds to approximately 4 mm in 25 min and is of more significance.

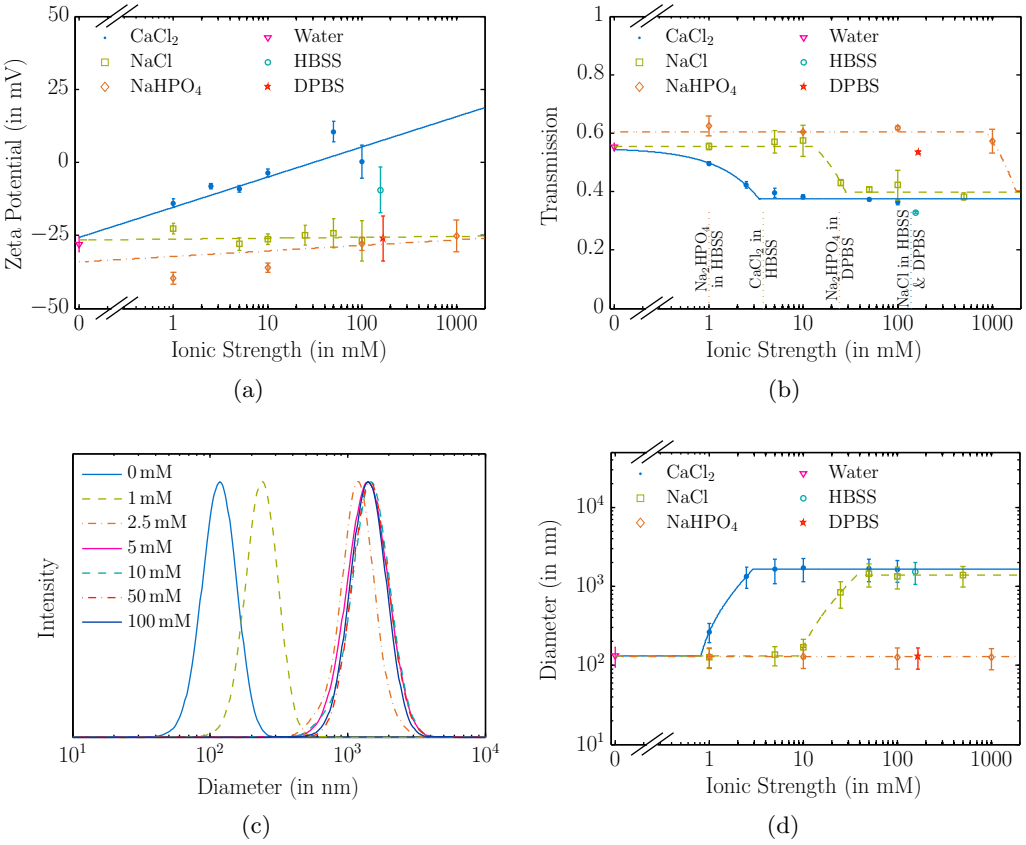

Figure 4.16: Influence of ionic strengths of nanoparticle suspensions on zeta potential (a) as well as on particles size measured by light transmission at 470 nm (b) and dynamic light scattering (c, d); water and buffered solutions are inserted at their total ionic strengths; size distributions are displayed for $CaCl_2$ suspensions (c); we refrained from displaying error bars in panel (c) for the sake of conciseness

4.3.2 Influence of Magnetic Field

Figure 4.17 shows the T_2 relaxation times after 25 min with and without a magnetic field. Since the T_2 relaxation time corresponds to particle aggregation [136–138], this is a well-founded indication of the aggregation process. Figure 4.17a exemplarily shows the relaxation time of calcium chloride suspensions over 25 min in the presence of a magnetic field. All T_2 values increase over time with the exception of purified water. A small amount of calcium chloride is enough to destabilize the particles sufficiently for aggregation in the presence of a magnetic field. Figure 4.17b shows the T_2 relaxation times after 25 minutes in the presence of a magnetic field, while 4.17c shows the same for the control samples without a magnetic field for all salt and buffered solutions. Please note the differing y-scales between 4.17b and c, d. It can be seen that the aggregation is enhanced by the magnetic field. This is reasonable

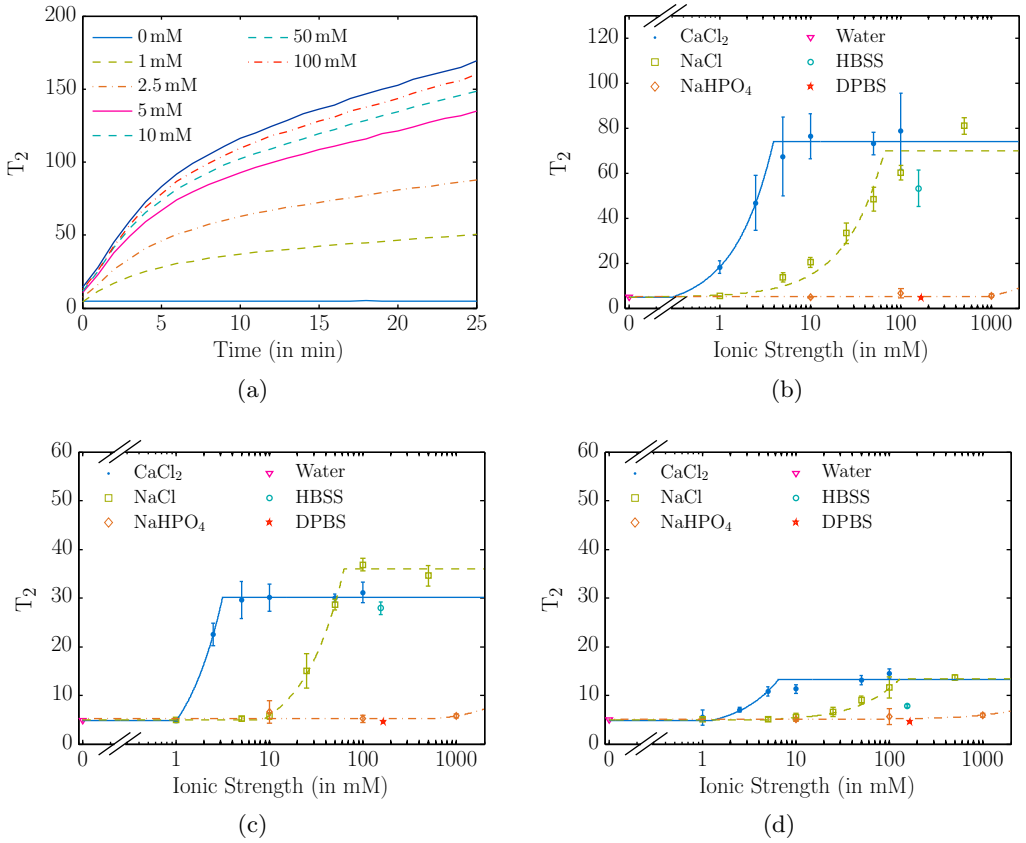

Figure 4.17: T_2 relaxation times of calcium chloride suspensions over time (a) and for different nanoparticle suspensions after 25 minutes in the presence of a magnetic field (b), in absence of a magnetic field (c) and after agitation (d); we refrained from displaying error bars in panel (a) for the sake of conciseness

since the used nanoparticles are superparamagnetic and the external magnetic field introduces an additional attracting force. Nonetheless, aggregation seems also to take place in the absence of a magnetic field, but with far less efficiency. The ionic strength $I_{c\_}$ where aggregation initiates is in good agreement with figure 4.16b and c. Figure 4.17d shows the T_2 value for both sample types after agitation. There is no significant difference recognizable between the samples with and without magnetic field after agitation.

Figure 4.18a shows the results for transmission measurements for water, buffered solutions and salt solutions with an ionic strength of 10 mM. Transmission values at $t = 0$ show a similar result as displayed in figure 4.16b. More interesting though is the behavior in the first few minutes of the measurement. Here, the transmission of the $CaCl_2$- and HBSS suspensions increases nearly linearly over the time, as described in chapter 4.2.2. For both solutions, the nanoparticles are already aggregated to their maximum size, see figure 4.16. For NaCl-, $NaHPO_4$- and DPBS

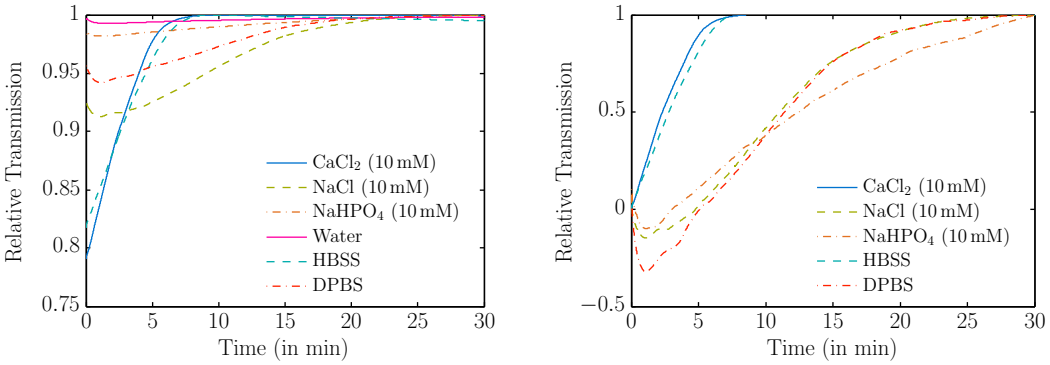

Figure 4.18: Transmission measurements in a magnetic field for nanoparticles in water, buffered solutions and salt solutions with an ionic strength of 10r mMelative to the final transmittance of the solution (a) and relative to the initial and final value (b); we refrained from displaying error bars for the sake of conciseness

suspensions, the transmission decreases initially until the trend reverses and the transmission increases similarly to the other two curves. However, the slope of the latter three curves is less steep as the one of the former two curves. For a better view of this phenomenon, figure 4.18b shows the transmission rescaled to their initial and final value. The transmission curve for water is not shown in the rescaled image, since the curve shows too much noise at this magnification to depict the result in a descriptive manner. However, as can be seen in 4.18a, the effect occurs also to a small degree in water.

Aggregate sizes were measured again after the application of the custom measurement device and subsequent agitation (data not shown). No significant differences to the size distributions of figure 4.16d were recognizable.

4.4 Discussion

We have successfully developed measurement devices for the characterization and study of magnetically labeled objects of different size ranges. Although both devices including their evaluation are only functional prototypes and there is room for improvements, both measurement methods have proven to be working successfully. Furthermore, both devices are of a comparably small size, can be used in different laboratories and easily be moved between laboratories.
While we took advantage of the possibility of observing larger objects like cells and microbubbles directly, we used the indirect observation via light transmission for smaller objects like nanoparticles and their complexes. However, the employed measurement methods differ not only by the size of their intended sample objects, but are fundamentally different due to their observation method. It is very difficult to measure microbubbles in the transmission device and nanoparticles via the microscope. Microbubbles come in an optically dense fluid which includes different phospholipids [15]. In our experiments, it has proven difficult to dilute the fluid enough for successful optical measurements, while keeping an appropriate concentration of intact microbubbles. To the same effect, a high cell density ($\approx 5 - 10 \cdot 10^6$ $^{\text{cells}}/_{\text{ml}}$) is necessary to achieve adequate results via transmission measurements. Vice versa, while complexes of magnetic nanoparticles are visible using a microscope, only the largest complexes are observable due to the limited contrast under an inverted microscope and their features are too indistinct for a successful automatic evaluation.

Magnetic Moment of Cells and Microbubbles

Although there already exist several similar methods to measure the magnetic moment or the magnetophoretic mobility of cells, most of them implicate that the cells are observed in flow. The most common method is to use a combination of one or multiple permanent magnets and a cell tracking velocimetry set-up. Zborowski and Chalmers *et al* [56, 65] used such a set-up in combination with paramagnetic particles. Those have a magnetic moment which is directly proportional to the magnetic field. Their set-up is optimized to a constant gradient of the magnetic energy density ∇B^2 which provides a constant force for paramagnetic nanoparticles.
Häfeli *et al* [64] as well as Wilhelm *et al* [139] used a single permanent magnet to divert the particles perpendicular to their flow direction, thereby exerting a very inhomogeneous force. Under those circumstances, it is inadequate to neglect the acceleration due to the magnetic force. Zborowski and Chalmers *et al* [56, 65] as well as Häfeli *et al* [64] used their set-ups for the evaluation of paramagnetic particles, assuming the magnetic moment to be proportional to the magnetic field.

While most of the cell tracking velocimetry set-ups are rather complicated, our only demand is the availability of an inverted microscope equipped with a digital video camera. In contrast to the described methods, we have a static environment for our objects, so we can safely assume that all observed long scale movement is due to the magnetic force. Additionally, we use containers where all optical planes

are perpendicular to the light beam to avoid optical distortions. The design of a constant energy density gradient is not applicable in the case of superparamagnetic nanoparticles. Even though the magnetic force can be approximated in a similar way (compare equation 2.11), this is only valid for flux densities smaller than 50 to 100 mT. For magnetic flux densities larger than 200 to 300 mT, the magnetic moment can be approximated as constant. However, for the region between both approximations, the magnetic moment is not linearly dependent on the magnetic flux density and we need to include the known magnetic properties for the evaluation.
Nevertheless, we aimed for a constant force, by designing a set-up with a homogeneous magnetic gradient. However, the magnetic gradient is not completely homogeneous and the absolute value of the magnetic flux density is comparably small and varies strongly in the outer region of the cell culture dish. This is due to the limited height available under the microscope. As mentioned above, the Langevin behavior would have little to no influence on the magnetic moment for higher magnetic flux densities, since this is equivalent to nanoparticles with a higher magnetic saturation. Thereby, such a set-up would be preferable. Nonetheless, we disregard the acceleration of the objects due to the non-homogeneous field gradient, similar to the measurements by Zborowski *et al* and Häfeli *et al*. The error on the magnetic moment is in the range of 5 to 10 % in the observed region and we are likely to underestimate the magnetic moment, see chapter A.2.2 for an estimate.
Moreover, large magnetic flux densities and magnetic gradients lead to a large magnetic force on the cells or microbubbles, thereby causing higher velocities of the objects. This not only makes a higher recording frame rate necessary, but also makes it more difficult to capture the movement of an adequate cross section of objects, since those with a higher magnetic moment might already be outside of the field of view. A better, but somewhat more complicated improvement would be a set-up with a high magnetic flux density and a comparably small, but constant magnetic gradient. In any case, further improvements concerning the magnetic set-up would imply larger and / or more permanent magnets. To accomplish a higher set-up size, while at the same time not interfering with the microscope optics, a custom made microscope stage would be necessary. Furthermore, such a microscope stage would also allow for a better positioning of the device itself, e.g. by including indentions for the device for several positions.

Figure 4.7 exemplarily shows the measurement results for two different cell types. The listed values for the magnetization were calculated individually for each reconstructed trajectory and subsequently fitted.
While all measured cell types share a normal distribution for the size distribution, only the ES-CMs display the same for velocity, magnetic moment and magnetization. The data gained from eCMs, BMCs and microbubbles can be fitted well to lognormal distributions. Therefore, it stands to reason that on the one hand, the displayed lognormal behavior originates from the lognormal distribution of the nanoparticles. Furthermore, the distributions of diameter and magnetic moment

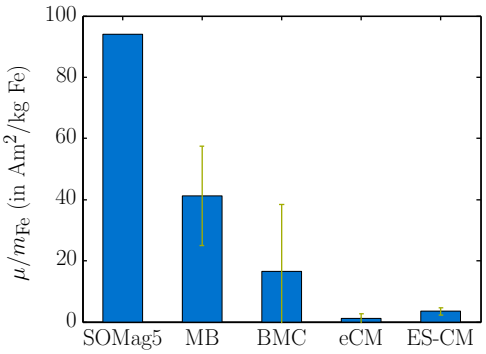

Figure 4.19: Comparison of magnetic moment per used iron amount for SO-Mag5 nanoparticles, microbubbles (MB) and different cell types (BMC, eCM, ES-CM)

cannot be transformed into the magnetization distribution by simple expressions as suggested by equation 2.1. This indicated that the amount of incorporated nanoparticles is, at least for the cells, mainly independent of their size. Contrariwise, it could also be possible that the velocity and magnetic data gained from eCMs, BMCs and microbubbles follows a normal distribution, but is truncated and only appears as a lognormal distribution due to the close proximity of the peak value to zero. The movement of the lower half of the distribution might not have been recognized as movement or was disposed of as Brownian motion. To investigate the exact correlation, a more detailed analysis with a higher time and space resolution would be necessary.
In the case of microbubbles, especially those incorporating SO-Mag5 nanoparticles, the distribution of the surface magnetization is dominated by a rather slim peak indicating a better correlation between surface and magnetic moment.
Moreover, we can see differences in the magnetic moment of the different cell types and microbubbles. Though ES-CMs display the highest magnetization of the cell types, the magnetization value of BMCs is approximately two thirds of the value of ES-CMs while using only a tenth of the iron amount. Clearly, the intake of the magnetic nanoparticles by the cells is different for each cell type. As already indicated previously, microbubbles have a large magnetic moment. Though the microbubbles have a smaller magnetic moment than the investigated cell types, they have a comparable or larger surface magnetization, while using the least amount of iron per object. Comparing the carrier types, the magnetic microbubbles clearly have the largest surface magnetization. Figure 4.19 shows the magnetic moments of those objects of table 4.2 with SO-Mag5 nanoparticles incorporated as well as the magnetic moment of SO-Mag5 nanoparticles themselves. The values are shown with respect to the used iron amount per object.

Magnetic Moment of Nanoparticles and Complexes

The approach to determine the magnetophoretic mobility of nanoparticles by measuring the optical density of a fluid was already described by Mykhaylyk *et al* [76, 77].

Their approach uses two identical blocks of permanent magnets, positioned on either side of a cuvette and the optical density is measured in the center between both magnets. The velocity of the particles is determined by using the time required until the optical density has decreased to 10 % of the initial value and the mean covered distance in that time. The equilibrium equation 4.6 and the mean magnetic flux density and gradient are used for the resulting magnetic moment.
In contrast to this approach, we have refined the magnetic set-up. Although the magnetic gradient of the set-up is not completely homogeneous, we aimed at an as homogeneous as possible gradient in the limited space around the cuvette. In the upper half of the set-up, the gradient varies rather extensively. However, this region is of no interest for the measurement. In the lower half of the container, the magnetic gradient is much more homogeneous, but still has some variations. Most of those variations are due to boundary effects generated by the limited height of the permanent magnets. The homogeneity could be increased by using higher magnets and possibly additional rings of permanent magnets. However, this would increase the size of the device and the distance between light source and detector. As a result, the light beam would widen, resulting in a wider scattering and intensity losses. Furthermore, we measure the optical density at a location, where the magnetic gradient is not subject to large variations and where the velocity and acceleration of most particles is well established.
The absolute value of the magnetic flux density in the set-up is still comparably small. A higher magnetic flux density would mean nanoparticles with a higher magnetic saturation up to the point where the Langevin behavior could be neglected. Thereby, it would not be necessary to know the magnetization parameter $\mathcal{E}$ of the particle type. Additionally, nanoparticles with a higher magnetic saturation experience a larger magnetic force which would allow us to measure the transmission of not aggregated (e.g. in deionized water) or very small nanoparticles in a reasonable time. With the current set-up, those measurements can take up to several hours. These benefits might outweigh the aforementioned drawbacks and might be worth an investigation in the future.
For the evaluation of the measurements, we use the calibration curve shown in figure 4.11. The curve is created from different concentrations of the nanoparticle type in the fluid. To gain a usable calibration profile, we have to assume that aggregation in the fluid is not dependent on the particle concentration. Aggregated particles mostly yield a smaller transmission, thereby falsifying the curve in figure 4.11. However, all investigated calibration curves show the same linear profile, supporting the assumption that the aggregation behavior does, for small concentrations, not strongly depend on the concentration.
For the extraction of the magnetization of the nanoparticles, we simulate the complete particle movement including random starting positions and diameters according to the size distribution of the complexes in the corresponding fluid. However, as we have seen in chapter 4.3.2, individual nanoparticles aggregate in homogeneous as well as in inhomogeneous magnetic fields. We have seen this effect in figure 4.18 as a part of the measurement. If the particles aggregate when put into the measurement

device, the beforehand acquired and the actual size distribution are not in good agreement. However, we were not able to measure the established size distributions, due to the necessary agitation process. The size measurements after the application of a magnetic field have shown no significant difference compared to measurements before the application of a magnetic field. On the one hand, the only way to avoid this problem would be to use only particles in fluids where no aggregation occurs (e.g. deionized water). However, this brings us back to the previous problem of a small magnetic flux density. On the other hand, this behavior offers us the possibility to further investigate the aggregation behavior. Furthermore, the device could easily be adjusted to create a homogeneous magnetic flux density of approximately 115 mT. This would simply involve a rotation of the individual magnets. Thereby, other particle specific characteristics could be investigated, e.g. chain formation in a homogeneous field [140].
In figure 4.15 and table 4.4 the measurement results for two different particle types are shown. While the results for FluidMag-Strep nanoparticles have comparably large errors, the values are compatible with a constant value within one standard deviation. The values for the SO-Mag5 measurement however, are differing greatly and seem to decline exponentially with increasing concentration. This behavior suggests that the assumption of a constant ratio of magnetic moment to volume is not well justified and that complexes of nanoparticles may very well have a varying particle density or form crystal-like structures under certain conditions.

There are many groups dealing with the description of light scattering at particles of a size comparable to the wavelength of the light [141–144]. Most of those focus on observing, measuring or modeling rain fields with radio signals, compare [107, and references therein]. Approaches may include single or multiple scattering, depending on frequency and particle density. A full description of this matter would exceed the scope of this work. We consider only the main contributions for our expression. However, the differing weights of the scattering cross sections for the different diameters are highly dependent on the input parameters. Most of those are only estimated, especially the refractive indices of the nanoparticles which may vary greatly depending on the particle type.

Tracking Algorithm

As previously mentioned, there are many particle and cell tracking algorithms freely or commercially available [e.g. 122, and references therein]. However, most of those [e.g. 123, 124] have problems with large distances between individual particle locations, since they are meant to track small distances and non-overlapping trajectories, e.g. for the tracking of Brownian motion or morphodynamic behavior. Others are able to track in three dimensions [e.g. 125, 126] or are overly complex for our application. We limit our tracking procedures to gray scale images and are only interested in linearly progressing trajectories. Furthermore, we do not want to evaluate small movements, but large scale movements. Only movements covering many times the

particle radius in distance over relatively short time frames allow for insights into the magnetic behavior.
Usually, a tracking procedure consists of the recognition of the objects for all frames and the subsequent or simultaneous association of those objects over a set of frames. Often used approaches for the recognition and identification of objects, are template matching [145] or watershed transformation [146, 147]. For the template matching technique, an intensity profile describing the objects is provided and the image is scanned for matching intensity features. To use a watershed transformation, the image is considered as a topographic relief and flooded, starting from local minima. The remaining regions are then considered to represent objects.
The simplest approach to associate objects over several frames is to identify the nearest neighbor in the next frame. The definition of the nearest neighbor can refer to spatial distance or, as in our algorithm, to other object specific criteria. This association is often solved by global optimizations [123, 148] or consecutive between every frame [149–152].
A similar method for global movements is particle velocimetry [153]. Particle imaging velocimetry or particle tracking velocimetry is used to observe turbulent flow. Particles are injected into the flow and illuminated by a light source, e.g. a laser. The particles are used as tracers to make the motion of the fluid visible. However, the tracking of those usually monodisperse particles takes often place in three dimensions.

We used a set of basic algorithms and combined them in a novel way to achieve a fast and reliable tracking algorithm. With the exception of the image import, the whole algorithm does not use any internal image processing tools provided by MATLAB. Therefore, it was designed as a platform independent algorithm which can be easily ported to another programing language. Furthermore, the usage of custom and adapted tools for image filtering, particle recognition and evaluation as well as trajectory recognition is accompanied by an acceleration of the whole algorithm compared to the usage of generic internal MATLAB functions.
The location and recognition of the objects is implemented separately from one another. This offers the possibility to expand the scope of recognized shapes, e.g. by pattern matching. Furthermore, by applying the connected-component algorithm on non-binary data, we could separate overlapping objects already in the location step. However, if the objects shapes differ substantially from the circular shape, we would have to extend the evaluation of the data, since on the one hand, the Stokes force in the form of equation 2.18 is only valid for spheres. On the other hand, we would have to consider the object alignment with respect to the direction of flow for very inhomogeneous semiaxes.
The weights for the trajectory reconstruction are given by the user and can thereby be varied or disabled as necessary for the data set. Additionally, the reconstruction step of the algorithm can be easily expanded by additional weights, e.g. shape similarities.
In contrast to the above mentioned cell tracking applications, our algorithm is designed to track homogeneous large distance movement. Since many cell types exhibit

a nearly monodisperse size distribution, the identification solely via the object size and absolute distance is not adequate. Therefore we also consider the relative angle between the individual objects. Since the objects move toward the magnetic ring surrounding them, they move mainly in radial direction and the angle between all objects of a trajectory has to be comparable. Furthermore, we do not only compare the values of size, distance and angle for subsequent objects, but also compare those values over the whole trajectory to exclude a merging or switching of adjacent trajectories.
We do not consider object interactions or dis- and reappearances of objects. If an object is temporarily out of focus or overlaps with another, we simply ignore those steps and start a new trajectory after the incident. This works well as long as disappearances do not happen very often and the trajectories are thereby, not broken into too short fragments. In a similar way, we split trajectories at irregular points like significant changes in size or angle. However, having multiple short trajectories instead of one long trajectory can impair the statistics of the result. Assuming that breaks in the trajectory occur mostly due to changes in the trajectory itself, e.g. due to external influences like vibrations, those disturbances are applied to the whole image. This interrupts all current trajectories in the same way and the fragments contribute equally to the statistic. Thereby, this influence is acceptable.

Particle Aggregation

We have seen that the stability of nanoparticles is highly dependent on the composition of the used solution. As already reported by French *et al* [154], we found a different aggregation behavior for different salts at the same ionic strength, e.g. SO-Mag5 nanoparticles in 25 mM sodium chloride solution show results comparable to 2.5 mM calcium chloride solution. Not only the concentration or ionic strength of the salt solution influences the behavior, but also ionic value or ion sort. Unstable particles aggregate without the influence of an external magnetic field and due to their larger size, sediment relatively fast. In case of the investigated particles, we were able to prevent sedimentation by agitation, but the particle aggregation was not reversible.
Already aggregated particles show an accelerated aggregation behavior in the presence of a homogeneous as well as an inhomogeneous magnetic field. The increase in the measured T_2-values in presence and without the presence of a magnetic field is supposedly a combination of aggregation and sedimentation, while in presence of the magnetic field, the aggregation obviously prevails. The sedimentation velocities calculated above, based on equation 2.32, are to be taken with reservations, since diffusion is not included in the approximation. There definitely occurs sedimentation for the particle suspensions for which high velocities were calculated, but the time frame was larger than the approximation suggests. In no case sedimentation was detectable by the naked eye in the course of one hour. However, after 24 hours the aggregated particles were fully sedimented, while no sedimentation occurred for non-aggregated particles.

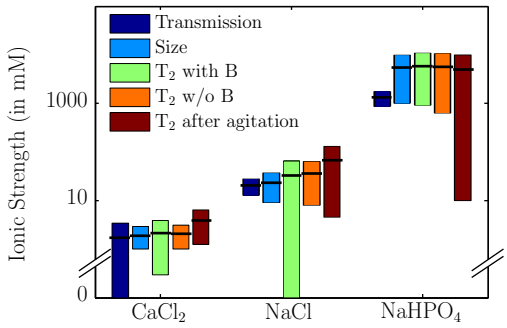

Figure 4.20: Comparison of different measurement methods for particle aggregation; bars denote the lower and upper bounds of the aggregation phase; the black line denotes the center value

The increase of the optical density in the measurements is an indication of further particle aggregation. As already mentioned, larger particles cause a lower light transmission. Thereby, aggregated nanoparticles lead to a lower light transmission as observed in figure 4.18b. The particles start to aggregate as soon as they are placed in the inhomogeneous magnetic field. This takes place even for the previously not aggregated particle states, e.g. for low sodium phosphate solutions. However, at one point during the measurement, the effect of the movement of the nanoparticles dominates the effect of the aggregation. From this time on, only an increase in the light transmission is measured. The aggregation seems to be not as effective or takes more time than directly observable, since the transmission increases noticeably slower than in the case of already aggregated nanoparticles.

The results of the different measurement types lead to comparable aggregation values. Figure 4.20 shows the lower and upper bounds $I_{c_\pm}$ of the aggregation phase as colored bars as well as the center value I_{c_m} between both as black line. All measurements are in good agreement with each other. Compared to the other measurement methods, the T_2 relaxation times show an earlier onset of the aggregation due to superparamagnetic characteristics of the nanoparticles in combination with the magnetic field. The direct measurement of the diameter via the ZetaSizer device tends to often show either aggregated or non-aggregated diameters and thereby offers the least accuracy in the aggregation phase. Additionally, the values for $NaHPO_4$-solutions are very rough, since we were not able to induce a fully aggregated particle state and thereby the model function 4.13 has not enough data values for an appropriate fit.
We deliberately did not adapt the pH values of the salt solutions, since this would include a change in either ionic strength, ion type or both. We wanted to primarily investigate the difference between salt solutions with different valence ions, and buffered solutions. HBSS and DPBS have a comparable total ionic strength and similar ingredients. Nonetheless, SO-Mag5 nanoparticles in HBSS are fully aggregated,

while the same particles in DPBS show nearly no sign of aggregation. Both buffer solutions are often used as is or with other salts in experiments due to their physiological concentration, pH and ionic strength. Their similar biochemical properties do not make buffer solutions universally compatible with nanoparticles. Similar to cell lines, one has to find the optimal buffer combination for each nanoparticle type and application. Keeping *in vivo* applications in mind, one has to pay special attention to the properties and behavior of nanoparticles in physiological fluids and especially blood.

The DLVO theory states that only two types of interaction are responsible for effects as aggregation. Apart from the particle diameter, there are four parameters which potentially influence the DLVO potential introduced by the solution: the permittivity of the fluid ϵ_r, the Hamaker constant A_H, the ionic strength I and the surface potential ψ_0.

- The variation of the **permittivity** in the investigated ionic strength range is very small, e.g. the difference between the permittivity of a 100 mM sodium chloride solution and the one of water is below 2 % [155] and behaves comparable for the other used solutions.

- In the same way, the variation of the **Hamaker constant** A_H is negligible. The constant depends mainly on the optical properties like refraction index and dielectric permittivity of the solution [103]. Based on the assumption that a total DLVO potential in the same order of magnitude as k_BT or smaller allows the individual nanoparticles to aggregate, different values for the Hamaker constant A_H would be necessary to achieve this behavior. Those values would be $A_{H,\mathrm{CaCl_2}} \approx \mathcal{O}(10^{-19})$, $A_{H,\mathrm{NaCl}} \approx \mathcal{O}(10^{-20})$ and $A_{H,\mathrm{NaHPO_4}} \approx \mathcal{O}(10^{-21})$.
  For an ionic strength of 1 M, the optical properties of the salt solutions differ from those of water less than 1 %. While the resulting variation in the Hamaker constant is already up to 6 % for sodium phosphate, this does not change the Hamaker constant by an order of magnitude.

- The **ionic strength** is directly included as the comparison parameter in our results. Therefore, it cannot account for the differences between the different salt solutions.

- The last parameter, the **surface potential**, cannot be measured directly and is only approximated by the zeta potential. Many works [156, 157] approximate the surface potential for every different solution and ionic concentration by the respective zeta potential in that solution. In contrast to this approach, we prefer to use the zeta potential in deionized water. There are two reasons for this approach. The first one is the inability to measure the zeta potential reliably for high salt concentrations. The other and more profound reason is that the surface potential as we understand it, is an inherent particle property and in contrast to the zeta potential not dependent on the solution. Thereby, the

value of the zeta potential in deionized water is the least screened measurable property and closest to the true surface potential. To use the respective zeta potential values for different solutions would imply that the differing values are the cause for the repulsive potential and not the consequence.

The standard derivation of the electrostatic double-layer interaction as used for the DLVO potential in equation 2.38 is subject to many assumptions and approximations. One of those assumptions is the same valence of cations and anions in the electrolyte solution (1:1 solution). This is clearly not the case for our solutions with the exception of water and sodium chloride [e.g. 96, 102, 103]. As already reported [99, 158], the DLVO theory in its approximated form can thereby not explain certain mechanism of colloidal stability. There are several other forces which can influence the colloidal stability and are neglected in the DLVO theory, e.g. solvation, structural and hydration forces. Those forces can be attracting, repulsing or oscillating dependent on different surface properties. For more details on those forces, see e.g. [99, 103, 159].

However, there are estimations originating from the DLVO theory which we can utilize. The Schultz-Hardy rule states that the critical coagulation concentration (c.c.c.) varies with the sixth power off the valence of the counterion. So the ion which has a contrary charge to the particle has a greater influence by shielding the surface potential of the particles. This explains the greater influence of calcium chloride in comparison to sodium chloride and the very small influence of sodium phosphate on the aggregation of SO-Mag5 particles. The particles are negatively charged and the valence of the counterion is 2 (Ca^{2+}) in case of calcium chloride and 1 (Na^{+}) in case of sodium chloride. In case of the positively charged PEI-Mag2 nanoparticles, the effect is inverse: sodium phosphate (HPO_4^{2-}) has the largest influence, while both chlorides have very little influence. However, taking the central ionic strengths I_{c_m}, we find a potency ratio of approximately 4 instead of 6 for SO-Mag5. The Schultz-Hardy rule thereby explains the behavior only qualitatively and not quantitatively.

A comparable effect of the different salts on the stability of proteins is known as the Hofmeister effect [158, 160, 161]. The Hofmeister series or lyotropic series reports a specific order of ions correlated with their ability to enhance or disable the solubility and stability of proteins. However, the exact order of the Hofmeister series may vary depending on the target substance and there is also an inverse Hofmeister effect known [162, 163]. There are several approaches to explain the effects, but despite much research, the exact origin and mechanism of the Hofmeister effect is still not explained.

5

Model and Simulation

In this part of the work, we present the results for different simulations of magnetic nanoparticle accumulation. We start with a simple model with a static fluid and proceed to movement in presence of a dynamic fluid. In either case, the aim is to accumulate a high amount of particles in a certain area. Therefore, we optimized the magnetic set-ups to achieve high magnetic flux density gradients while obtaining certain geometrical patterns. The set-ups were already presented in chapter 3.1 and are discussed only briefly in the following. In this chapter, we focus on the calculation of the according trajectories of the magnetic nanoparticles and the evaluation of the amount of accumulated particles for certain areas.
To verify the results of our simulations, we compare selected simulations with experimental results. Furthermore, we investigate the influence of different parameters e.g. geometry, nanoparticle properties and so forth.

5.1 Trajectory Simulation

For the following models, we calculated the trajectories for $N = 10'000$ individual nanoparticles, complexes or cells. This number of particles yields statistically stable results while keeping the computing time reasonable. The general schematic of the simulation algorithm is shown in figure 5.1 and consists of the following parts:

1. To describe the complete experimental set-up, we build a model object which is composed of several different substructures which in turn describe the physical and spacial boundaries conditions. A geometry object describes the geometric boundaries and the symmetry of the container. Based on the data provided by *Comsol Multiphysics*, there is a structure containing the physical fields, like magnetic field $\vec{B}$, gradient field $\vec{\nabla}B$ and fluid velocity $\vec{u}$. Another structure describes additional fluidic properties, e.g. viscosity and density. Additionally, the model object includes other input parameters, e.g. the number of passages or the initial particle distribution.

2. Subsequently, a number of particle objects is generated. Based on the particle specific characteristics and the fluid properties, the size of the nanoparticles

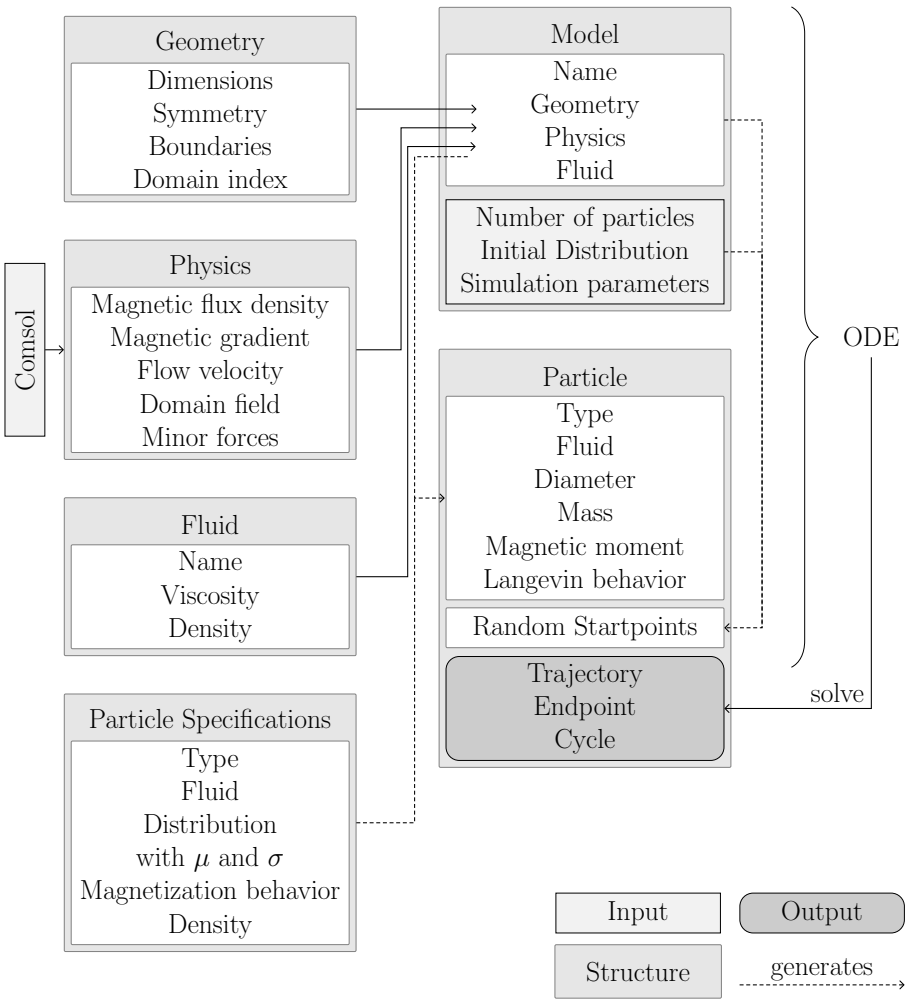

Figure 5.1: Schematic of particle trajectory simulation: relevant information is collected in specific structures from which the model and particle structures are generated; both serve as input to the differential equation and influence the result

is randomly generated according to the provided distributions. The starting positions $\vec{x}_0$ where the particles are released are also randomly generated according to the input parameters. For static *in vitro* models, particles are uniformly distributed over the complete area of interest. For dynamic *ex vivo* models, e.g. vessels, the starting positions are chosen in such a way that the laminar flow profile is already established and the magnetic flux density gradient is still negligible. This means that no boundary effects due to the inlet take effect and no forces apart from a laminar flow act on the particle complexes in the first couple of time steps. Thereby, a stable flow velocity of the particles is achieved. Here, the positions are uniformly distributed in the axial / flow direction and normally distributed in radial direction with the mean value of

the distribution set to the center of the vessel.
Additionally, the particles are provided with initial velocities close to the flow velocity at their position. An initial velocity identical to the flow velocity would lead to numerical instabilities.

3. A set of equations describing the differential equation 2.41 and according terminal conditions are created. While the differential equations mostly depend on the particle properties, the terminal conditions mainly depend on the model geometry. The trajectory for each particle is then calculated individually by solving those equations. If a complex leaves the domain of the fluid, the terminal condition for this complex is fulfilled and the trajectory ends at this position. The complete trajectory and the end positions are stored as particle properties.

4. The final particle positions are then evaluated concerning their locations with respect to their inert properties.

5.2 Static Model

5.2.1 Local Gene Targeting and Cell Positioning

In the following, we compare results of simulation and experiment for gene and cell delivery to confined areas. For this experiment* nanoparticle/lentivirus complexes as well as bone marrow cells in combination with SO-Mag5 nanoparticles were used as described in Kilgus *et al* [109]. The positioning of the complexes and cells was achieved by a large permanent magnet combined with three different soft-iron tips as described in chapter 3.1.2. Those three tip geometries include a 200 µm tip as well as a flat and a rounded 3 mm tip. Figures 5.2a-c show schematic drawings of three different tip shapes with the resulting magnetic gradient. The first tip has the smallest diameter with 200 µm and creates a very focused gradient field (figure 5.2d). Both 3 mm tips create a ring shaped gradient maximum. While the ring generated by the flat tip is rather sharp as shown in figure 5.2e, the shape of the rounded tip gradient is more blurred (see figure 5.2f). The distribution of the nanoparticle complexes was simulated based on their trajectories in the gradient field of the magnet flux density as shown in 5.2. The diameter of nanoparticle/lentivirus complexes and cells was determined by dynamic light scattering and a lognormal distribution with a mean of $m \approx 950\,\text{nm}$ and a standard deviation of $\sigma \approx 320\,\text{nm}$ was obtained. The size of the bone marrow cells was determined by evaluating microscopic images and a normal distribution with a mean diameter of $m = 9.4\,\mu\text{m}$ and standard deviation of $\sigma = 2.5\,\mu\text{m}$ was obtained. For more details on those distributions see chapter A.1.2. The calculation of the trajectories was simplified to a rotational symmetric geometry. The initial positions of the particles were distributed equally in the area of the fluid. In contrast to previously published results in Kilgus *et al* [109], the following simulation results include gravity, Langevin magnetization behavior, slightly differing properties for the cells and the influence of the horizontal shaker. The horizontal shaker is modeled as an additional force in radial direction.
The experimental results were evaluated by measuring the GFP (green fluorescent protein) intensity within shells of 250 µm distance in case of the nanoparticle/virus complexes. Those values were normalized to the area of the respective shell to quantify the amount of accumulated nanoparticles. In case of the bone marrow cells, the amount of accumulated cells was evaluated microscopically and again normalized to the according area. The gained quantity can be seen as an intensity or cell density and associated with the amount of nanoparticles and is thereby directly comparable to the simulated results.

Figures 5.3 and 5.4 show the results for the previously described magnetic tips with a topmost diameter of 200 µm and 3 mm. For the 200 µm tip, the GFP expression was restricted to a central spot (figure 5.3a) of approximately 1 mm diameter. The experimental results yielded approximately 60 % of the GFP intensity within

*Experiments were performed by C. Kilgus and P. Sasse, Institut für Physiologie 1, Universität Bonn

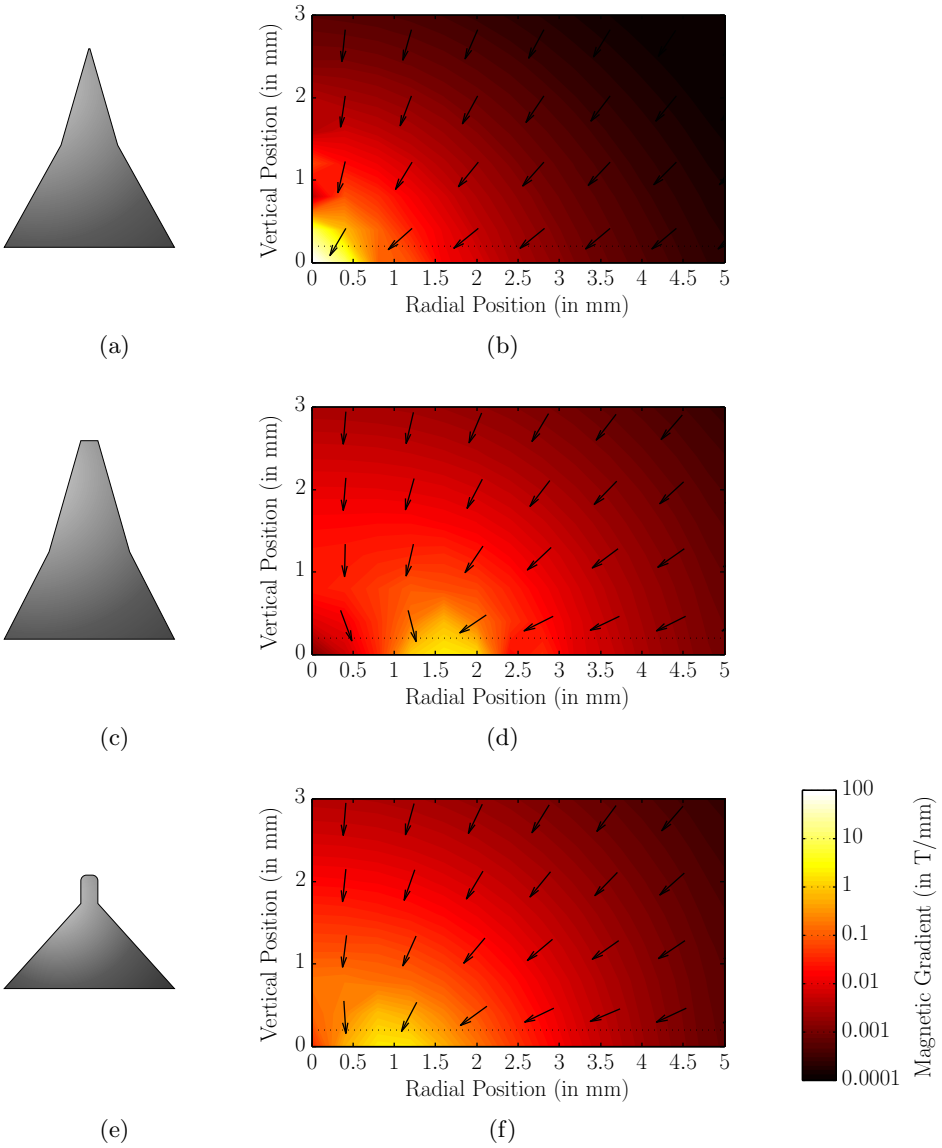

Figure 5.2: Schematic drawing of soft iron tips with different diameters and shapes: 200 µm flat (a), 3 mm flat (b) and 3 mm rounded tip (c); resulting gradient of magnetic flux density for those tips (d-f); the color scale applies to panels (d-f)

the innermost 500 µm area which is in agreement with the simulation, predicting approximately 35 % of the complexes in this range.
Figure 5.3b shows the same results for bone marrow cells. Taking the different physical characteristics as mass, size and hydrodynamic magnetization into account, we nonetheless achieved a similar distribution. The cells were localized in a very confined spot of 500 µm diameter and approximately 90 % cell density was found within 250 µm from the center. This is a much better localization than predicted by the

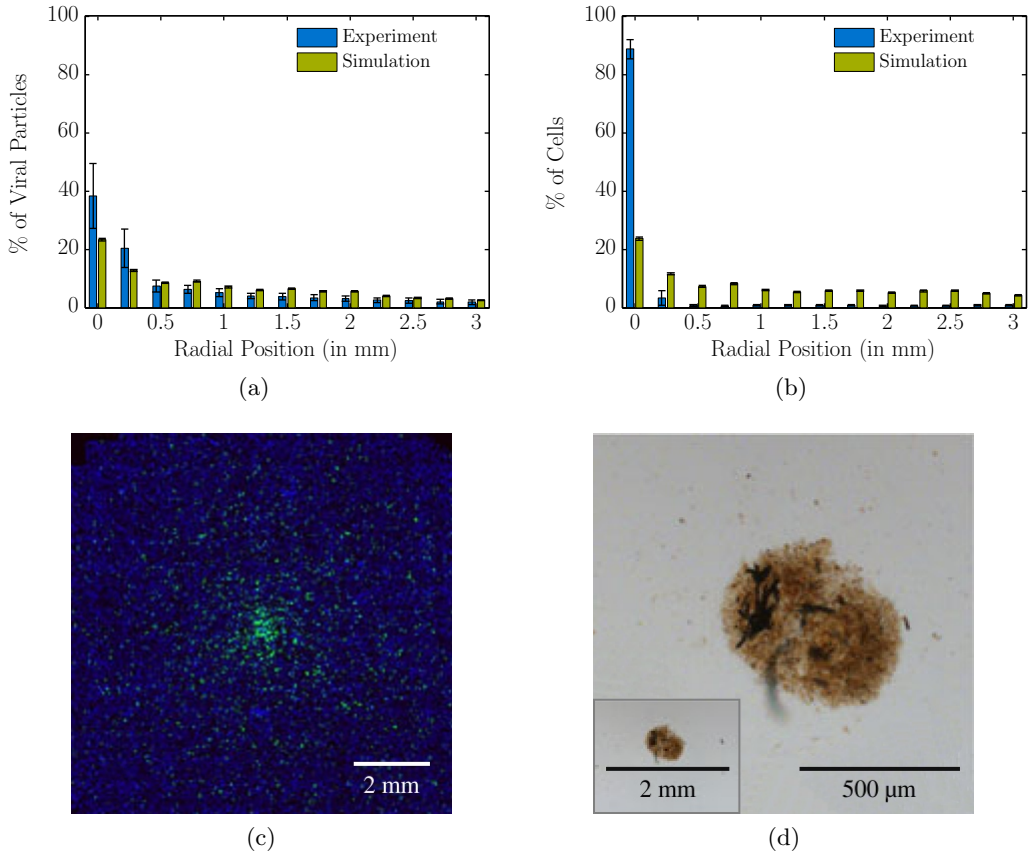

Figure 5.3: Amount of lentiviral particles (a) or bone marrow cells (b) for experiment and simulation for 200 µm magnetic tip and local accumulation of the same for representative experiments (c, d)

simulation which yielded only about 30 % of cell density within this distance. In case of the cells, the simulation yields a much broader distribution than the experiment. Figures 5.3c and d show microscopy images of GFP expression and cell accumulation, respectively, for a representative experiment.

Figure 5.4 shows the results for differently shaped 3 mm tips with bone marrow cells. Due to the shape of the flat tip, a high magnetic field gradient occurs on the edges of the tips leading to a ring shape; compare also figure 5.2b and c. By gradually narrowing the tip through the rounded shape, the gradient of the magnetic flux density is more equally distributed around the topmost area of the tip. The flat tip leads to a circular distribution with a mean diameter of approximately 3 mm and a width of approximately 500 to 700 µm in both experiment and simulation as shown in figure 5.4a. Figure 5.4b shows the simulation results of a rounded tip. This yields a broader circular shaped accumulation of cells with a diameter of approximately 2 mm and a declining cell density in the center. However, the experimental data

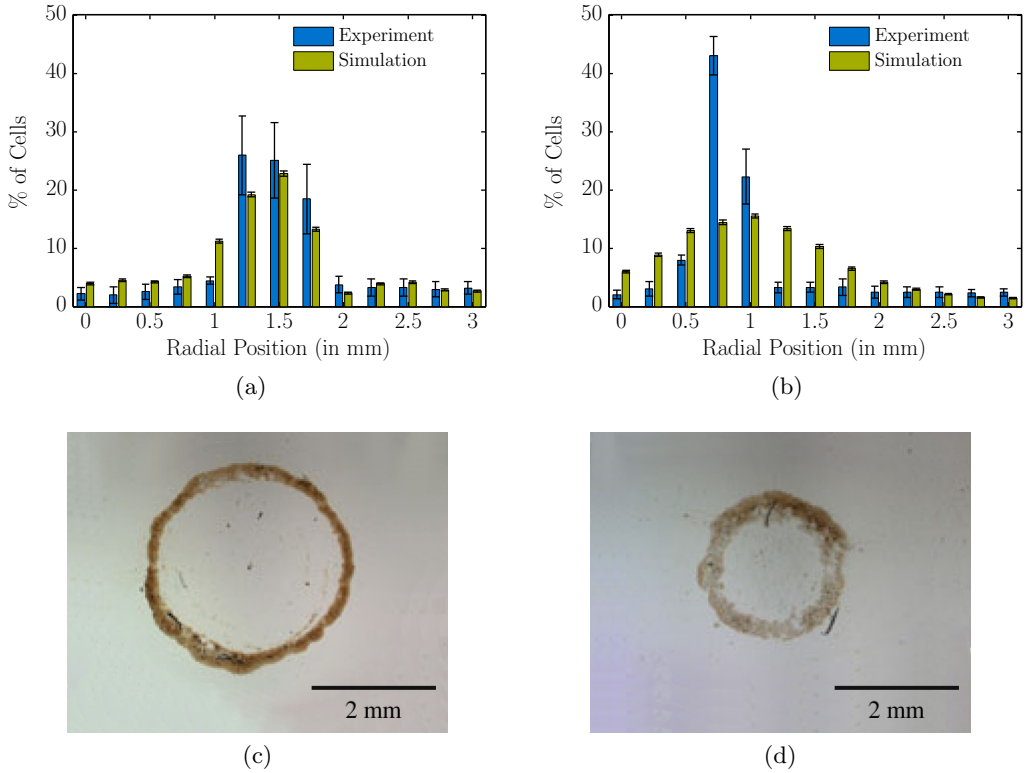

Figure 5.4: Amount of bone marrow cells for experiment and simulation for 3 mm flat (a) and rounded (b) magnetic tip and local accumulation of the same for representative experiments (c,d)

did not reproduce these results and while the cells were localized in a circular shape with a comparable diameter, the center was free of cells.
Figures 5.4c and d show microscopy images of the cell accumulation for a representative experiment.

5.3 Arterial Model

In the following, we investigate the accumulation of nanoparticle/lentivirus complexes in flow. The aim is to distribute nanoparticle complexes as homogeneously as possible along a perfused murine aorta. To compare the result of the simulation with the experimental results[†], we use an *ex vivo* flow-loop system, as described in Heidsieck *et al* [164] which allows us to experimentally determine the amounts of retained particles in a murine aorta.
To achieve a homogeneous and radially symmetric complex deposition during perfusion, we used a magnetic set-up consisting of twelve small magnets, arranged as a quadrupole around the vessel. The magnetic set-up is described in more detail in chapter 3.1.1. With this set-up, a magnetic flux density up to approximately 300 mT at the outer border of the artery as well as a magnetic flux density gradient of approximately 750 $^{\mathrm{T}}/_{\mathrm{m}}$ in the region of the magnets is achieved.
The axial axis along the vessel is henceforth referred to as z-direction. The fluid flows in z-direction into and out of the vessel. The constant flow rate at the inlet of the artery is set to 5 $^{\mathrm{ml}}/_{\mathrm{min}}$, which corresponds to a mean inflow velocity of approximately 0.19 $^{\mathrm{m}}/_{\mathrm{s}}$. This leads to an average Reynolds number of approximately 128 and a maximum value of 500.
The hydrodynamic diameter of the complexes was determined by dynamic light scattering and a lognormal distribution with a mean value of $m \approx 830\,\mathrm{nm}$ and a standard deviation of approximately 190 nm was obtained. The initial distribution of the positions of the magnetic nanoparticles is based on a normal distribution in radial direction and a uniform distribution in flow direction. The mean value of the normal distribution was set to the center of the vessel, while the width was defined so that the vessel radius corresponds to 2 times the standard deviation. This corresponds to 95 % of the particles being inside the vessel by default. The remaining 5 % are then resampled until all particles are inside the vessel. Thereby the probability inside the vessel is homogeneously increased while the probability outside of

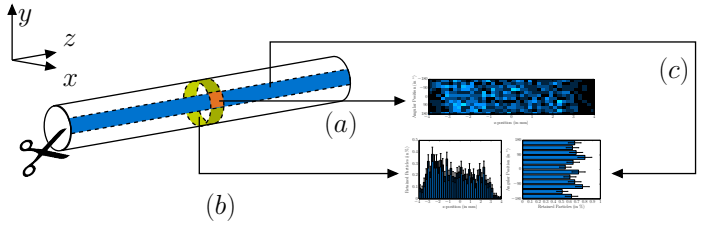

Figure 5.5: Explanatory sketch of the aorta and depicted histogram data in figures 5.6 and 5.12; the surface of the vessel is subdivided into small rectangles: the number of complexes in each rectangle (orange) is displayed in panel (a), while the sum over the rectangles in axial direction (blue) is displayed as a bin in panel (b) and the sum along the circumference (green) is displayed in panel (c)

[†]Experiments were performed by S. Vosen and D. Wenzel, Universität Bonn

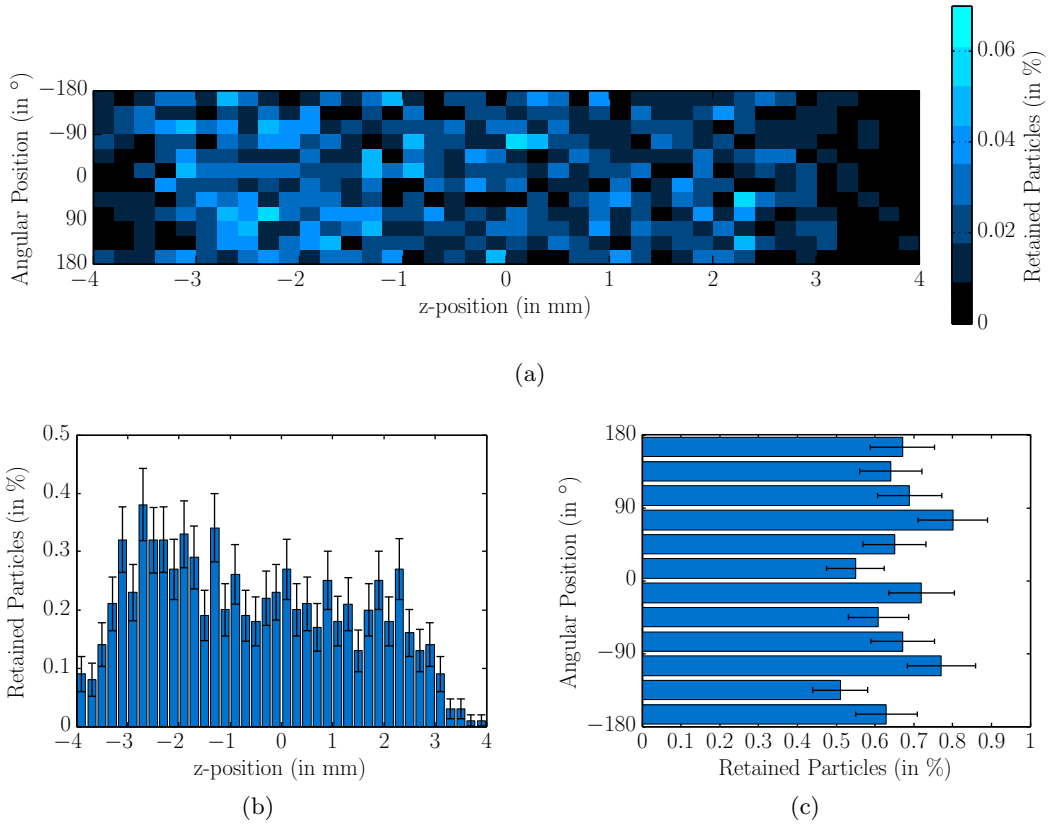

Figure 5.6: Percentage and location of the retained complexes in the target area; model aorta was cut lengthwise and "rolled out" (a): color indicates percent of retained complexes per position, where the sum over each column is shown in panel b and the sum over the rows in panel c

the vessel is set to zero, see also figure 5.9b.
The length of the cylinder was chosen to ensure a long enough chapter to establish the flow profile for the in- and outlet of the fluid flow.

Figure 5.6 shows the results of the three dimensional simulation with the amount and locations of the retained complexes in the target region of the aorta. We display only the region covered by the magnets plus an edge of 1 mm ($-4\,\text{mm} \leq z \leq 4\,\text{mm}$). A few complexes are retained outside of this region before or after the magnets. Those retentions are mainly due to their outward starting position or as a relict to the diversion by the magnetic force. The amount of retained complexes outside the target region is usually in the order of 1-2 % of the amount of particle complexes retained inside the target region.
Figure 5.5 shows the model aorta, cut lengthwise on the lower side as indicated and projected on a two-dimensional surface. The surface is subdivided into small rectangles with a side length of approximately 0.2 mm. The number of complexes

retained in each rectangle in the simulation is counted and the resulting amount of complexes per rectangle is indicated in terms of color in figure 5.6a. The x-axis represents the z-position in mm and thus the length; the y-axis shows the angular position, where an angle φ of zero corresponds to the top and an angle of $\pm 180°$ denotes the bottom of the aorta. The sum of each column in figure 5.6a is depicted in figure 5.6b, therefore displaying the percentage of retained complexes per z-position; the sum over each row of figure 5.6a is shown in 5.6c, showing the percentage of retained complexes per angular position. Integrating any one of those histograms, we obtain a total retention rate of approximately 7.9 % in the studied model.
As expected, the complexes accumulate mainly in the region covered by the magnets. The positions of the individual magnets cannot be distinguished, as was intended by the magnetic configuration. However, the left side shows a slightly higher amount of particles.

5.3.1 Multiple Passages

To increase the amount of deposited complexes in the experiment, the solution can circulate for 30 minutes through the magnets. This corresponds to 15 passages of the particle complexes. To determine the efficacy of such an approach, we calculated 30 passages of the fluid through the magnetic set-up. All complexes which were not retained in the previous passage were injected with new starting positions in the inlet area of the vessel. This was repeated for every passage.
The development of the retention rate as a function of the passages is shown in figure 5.7a and b. Figure 5.7a shows the caption rate in each passage relative to the amount of complexes which have not been retained in the previous passage. This removes the influence of the decreasing amount of complexes from the data; nevertheless the retention rate decreases. The effect can also be seen in figure 5.7b, which shows the summarized retention rate for each passage. The total number of retained complexes shows a saturation behavior below 100 %. Thus, there are complexes which cannot be retained. In figure 5.7c, the diameters of the retained particles complexes are stacked up in different colors for the individual passages in groups of five. This means the lowest bins are for passages one to five, the next for passages six to ten and so on. On top are also the diameters of the particle complexes which could not be retained. It can be seen that the larger complexes have a higher probability of getting retained, while the smaller complexes are mostly carried away.

To confirm the results of the numerical simulations of the complex deposition, perfusion experiments were performed. The magnet configuration was tested in an *ex vivo* flow-loop system [165, 166]. The particle complexes were injected and 15 passages of recirculation were performed. Then the aorta was removed from the flow-loop system and brightfield microscopy pictures showed a homogeneous deposition of nanoparticles along the area where the magnets were placed (see figure 5.8a, b and d). Figure 5.8c shows a reconstruction of a magnetic resonance image

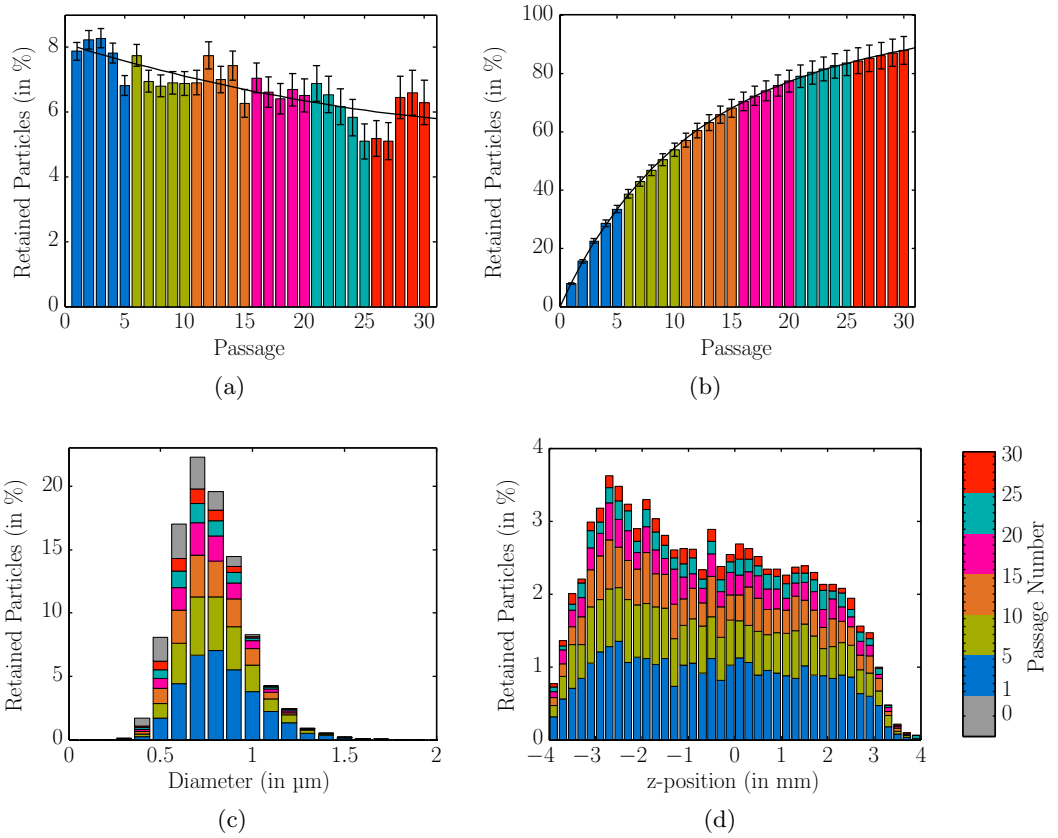

Figure 5.7: Percentage of retained complexes in each passage, relative to the remaining complexes (a) and in total (b); accumulative histograms of size (c) and local (d) distribution of the retained complexes for individual passages

(Bruker Spect, 600 MHz, TE = 6 ms, TR = 500 ms, spin-echo sequence). The vessel is colored red, while the signal due to magnetic nanoparticles is colored blue. However, the blue color does not indicate individual particles but a representation of the change of the T_2 value due to the dipole moments of the nanoparticles and thereby covers a larger area than the particles themselves.

To compare the numerical simulation of retention of complexes with the experimental results, the relative iron amount within the aorta after 15 passages was determined. For more details, see Heidsieck *et al* [164].

The iron amount of the retained particle complexes in the experiment is approximately 60 %, whereas the number of retained complexes in the simulation reaches 68 %. If we approximate the amount of iron to be proportional to the volume of the complexes, we obtain a larger percentage of approximately 77 %.

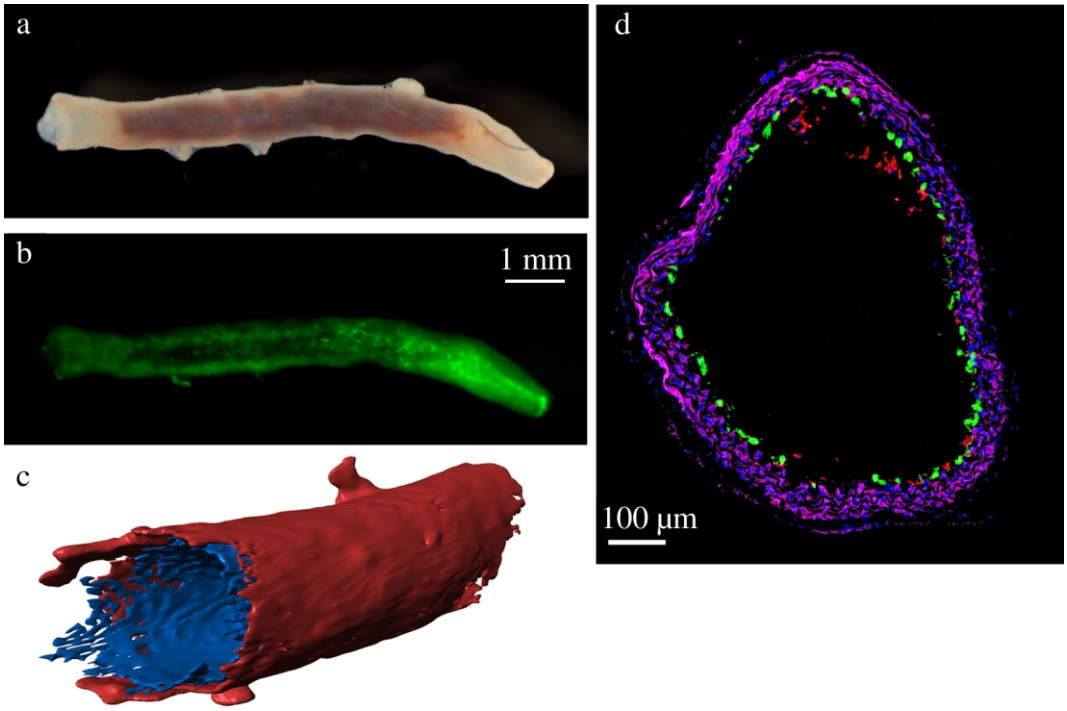

Figure 5.8: Homogeneous deposition of lentivirus/particle complexes in the *ex vivo* flow loop system: bright field microscopy shows homogeneous particle deposition (brown) after perfusion (a); fluorescence microscopy demonstrates bright eGFP expression six days after perfusion (b); immunostaining of aortic cryosections proves the radially symmetric manner of eGFP expression (green = eGFP, red = PECAM, magenta = alpha-smooth muscle actin, blue = DNA) (d) and magnetic resonance image of a rat aorta with vessel indicated by red color and signal due to nanoparticles indicated by blue color (c)

5.3.2 Comparison of Input Parameters

To investigate the impact of inaccuracies in the input parameters, we compared the possible influence of several of those parameters. To this end, we explored the effect of a change in the fluid velocity, as well as the impact of the particle properties, on the retention rate after one passage. All of the following simulations were carried out in two dimensions assuming a rotational symmetry of the geometry.

Geometry and Velocity

Figure 5.9 shows the percentage of the retained particles in panel (a) in dependence on the distribution of the starting positions as shown in panel (b). The first four bins depict the result for normal distributions with the vessel radius corresponding to 1, 1.5, 2 or 3 standard deviations. Based on the fact that 99.7 % of normally distributed points are inside of the interval of $\pm 3\sigma$, the leftmost bin of figure 5.9a represents

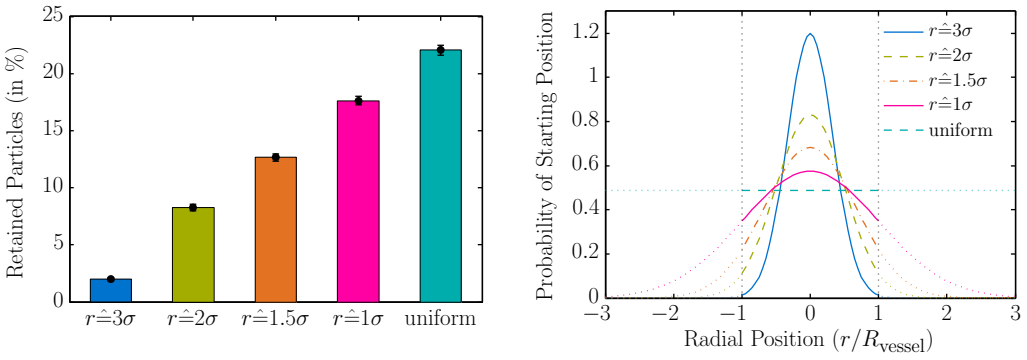

(a) (b)

Figure 5.9: Percentage of retained complexes for different distributions of the starting positions: normal distribution with vessel radius corresponding to 1, 1.5, 2 or 3 σ and uniform distribution

the result for completely normally distributed positions. In case of the broader normal distributions, all particle positions outside of the vessel were resampled with the same distribution, thereby increasing the probability inside the vessel over the complete region while setting the probability outside of the vessel to zero. The retention rate increases with decreasing standard deviation of the distribution. The narrower the starting point distribution, the larger is the mean radial distance a particle has to travel for a successful retention.

Figure 5.10 shows the change of the overall retention rate after one passage for different combinations of fluid velocity, flow rate and vessel diameter. All values are normalized to the values used above; that is a fluid velocity of 0.2 $^{\mathrm{m}}/_{\mathrm{s}}$, a flow rate of 5 $^{\mathrm{ml}}/_{\mathrm{min}}$ and a vessel diameter of 0.75 mm.
Figure 5.10a shows the retention rate for different fluid velocities and the respective flow rates. As expected, the retention rate decreases with increasing flow velocity. For flow rates larger than 3 times the initial flow rate (15 $^{\mathrm{ml}}/_{\mathrm{min}}$), the amount of retained complexes falls below 5 %. For flow rates of 0.5 (2.5 $^{\mathrm{ml}}/_{\mathrm{min}}$) and slower, the retention rate increases rapidly, until most complexes can be retained for very low flow rates (0.3 $^{\mathrm{ml}}/_{\mathrm{min}}$). Discrepancies of ± 10 % in the normal flow rate lead to a change of ∓ 0.6 % in the retention rate.
Figures 5.10c and d show the retention rate for different vessel diameters while holding the fluid velocity (c) or the flow rate (d) constant. When changing the vessel diameter, the magnetic flux density was simply remapped onto the new geometry. Thereby, the magnetic field gradient changes rapidly for the different diameters. Figure 5.10b shows the radial component of the magnetic gradient at the vessel wall in the center of the magnetic set-up for the different diameters. Using those values, we obtain a retention rate decreasing with the vessel diameter while holding the fluid velocity constant. The decrease is even steeper than in figure 5.10a. Here, we

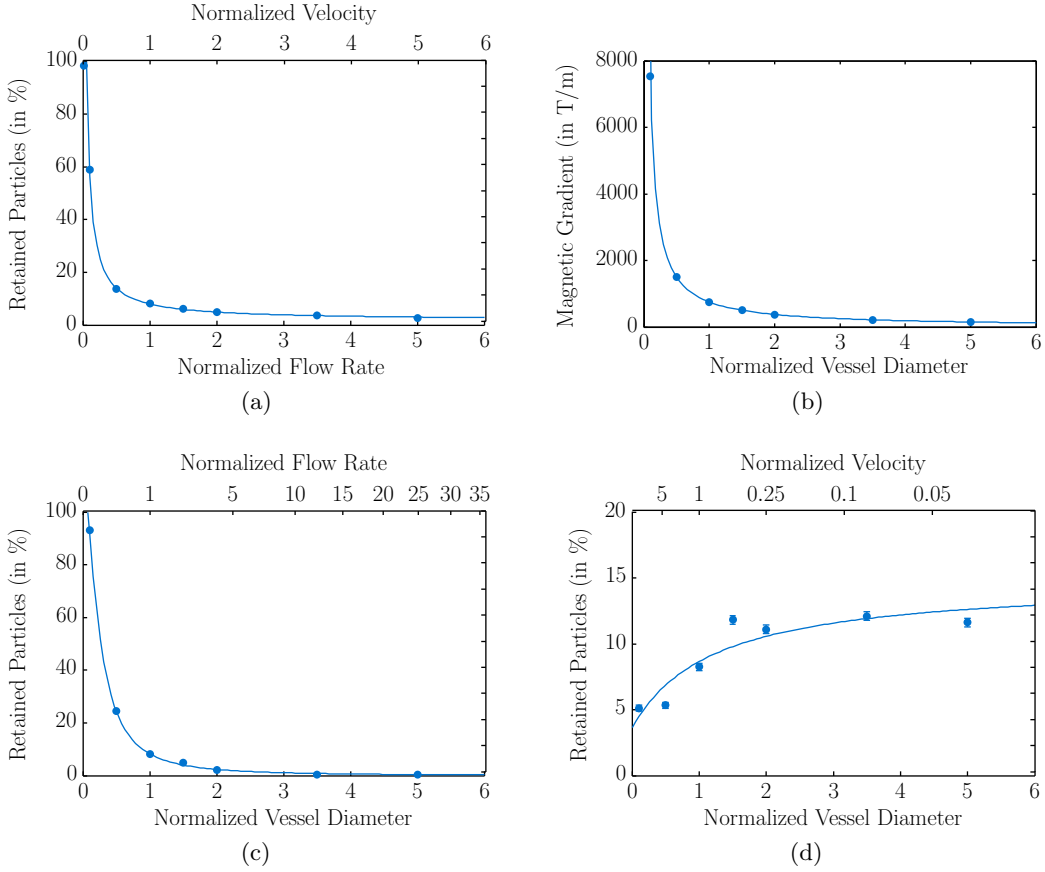

Figure 5.10: Percentage of retained complexes for different fluid velocities, flow rates and vessel diameters; panel (a) depicts the result for different flow velocities and flow rates; panel (b) shows the change of the magnetic gradient field for the different vessel diameters as used for panel (c) and (d), which show the results for different vessel diameters with constant fluid velocity (c) and constant flow rate (d)

achieve a retention rate of 95 % of the particles and higher for very small diameters of 75 µm (normalized value 0.1). This corresponds to a flow rate of (0.05 $^{\mathrm{ml}}/_{\mathrm{min}}$). Note, that not all of the used assumptions are still valid for diameters this small. Discrepancies of ±10 % in the normal vessel diameter lead to changes of −1.6 % to 1.2 % in the retention rate.

Figure 5.10d depicts the retention rate for varying vessel diameters with a constant flow rate. Here, the retention rate is nearly constant over the investigated parameters. This seems obvious due to the scaling of all influential parameters. While the fluid velocity scales with the inverse cross-section of the vessel and thereby decreases proportional to r^2, the magnetic gradient field decreases only proportional to r. Thereby, the fluidic force decreases faster than the magnetic force and the combination nearly compensates for the larger distance the particle has to cover to reach the vessel wall. However, in the region of the used diameter, the variation

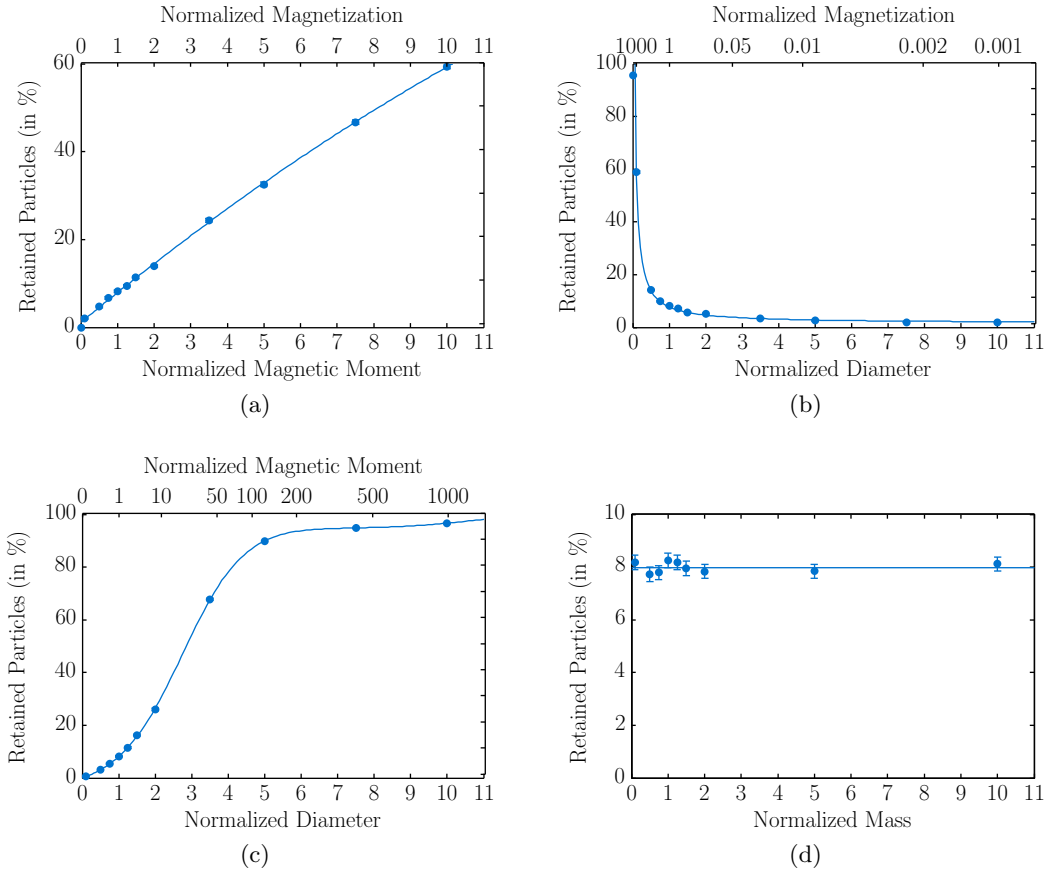

Figure 5.11: Percentage of retained complexes for different magnetic moments or magnetizations at a constant complex size (a); for different diameters or magnetizations at a constant magnetic moment (b); for different diameters and magnetic moments at a constant magnetization (c); for different masses (d)

is comparably large and a discrepancy of ±10 % in the diameter results in ±0.3 % variation of the retention rate.

Particle Properties

The physical properties of the particle complexes are particularly difficult to determine and might be afflicted by substantial inaccuracies. To investigate the influence of such inaccuracies, we compared the simulation results for different magnetic moments, diameters and masses. We vary only one parameter at a time, while all other boundary conditions, like geometry and flow rate, are held constant.
In figure 5.11a, the change of the retention rate for different magnetic moments of the complexes is shown. Here, the size of the complexes does not change, only the magnetic moment of the individual complexes varies linearly. As a result, the hydrodynamic magnetization M_h changes with the magnetic moment μ. The magnetic

moment as well as the magnetization, depicted in figure 5.11a, are normalized to the mean value of the distribution. This means, a magnetization of 1 corresponds to $41\,^{\mathrm{kA}}/_{\mathrm{m}}$. As the magnetic moment becomes larger, the magnetic force increases and finally overcomes the fluidic force. Discrepancies of $\pm 10\,\%$ in the normal magnetic moment of the complexes lead to a change of $\pm 0.7\,\%$ in the retention rate.
Figure 5.11b shows the change of the retention rate for different diameters of the complexes. In contrast to the parameter run over the magnetic moment, the moment now stays constant. We did not change the width of the size distribution, but only displaced it relatively to the original distribution, normalized to the mean value. This means, the magnetization M_h changes with the inverse volume of the complex. The larger the complex, the larger is the fluidic force and thus, the smaller is the influence of the magnetic force. For complexes smaller than a third (approximately 300 nm), the retention rate increases rapidly until the hydrodynamic force is negligible and all particles can be retained. In the same way, particle complexes larger than three times the original diameter (larger than 3 µm), the retention rate decreases nearly constantly. Discrepancies of $\pm 10\,\%$ in the mean diameter of the complex lead to a change of $\mp 0.6\,\%$ in the retention rate. A variation of the hydrodynamic diameter compared to the magnetic moment of the particle complexes could originate in different coatings, different aggregation behavior and/or different composition of the complexes (see also chapter 4).
Figure 5.11c shows the change of the retention rate for the case that diameter as well as magnetic moment are changing while the magnetization is held constant. This parameter run is the most suitable for physical nanoparticles and complexes, since hereby different aggregation characteristics can be approximated. The progression of this result can be qualitatively estimated by combining the results from figure 5.11a and figure 5.11b. However, we are not able to predict the coefficients of this combination. The most interesting part about this parameter run is the saturation of the retention rate. For particle complexes larger than approximately 5 times the normal diameter (which corresponds to a diameter of approximately 5 µm), further increase of the size does not result in a higher retention rate. Discrepancies of $\pm 10\,\%$ in the mean diameter lead to a change of $\pm 1.2\,\%$ in the retention rate. Thereby, this is the largest influence on the retention rate in terms of particle properties.
Figure 5.11d shows the change of the retention rate for different masses or densities of the complexes. The retention rate changes only marginally and all data points are consistent with a constant value over the studied range.

Influence of Minor Forces

In order to investigate the influence of the minor forces described in chapter 2.2.3, we repeated the three dimensional simulation described in the beginning of chapter 5.3 and included gravity and lift force as well as Brownian motion according to equations 2.23, 2.25 and 2.28. Figure 5.12 shows the results of this simulation with the amount and locations of the retained complexes in the target region of the aorta. Again, we display only the region covered by the magnets plus an edge of

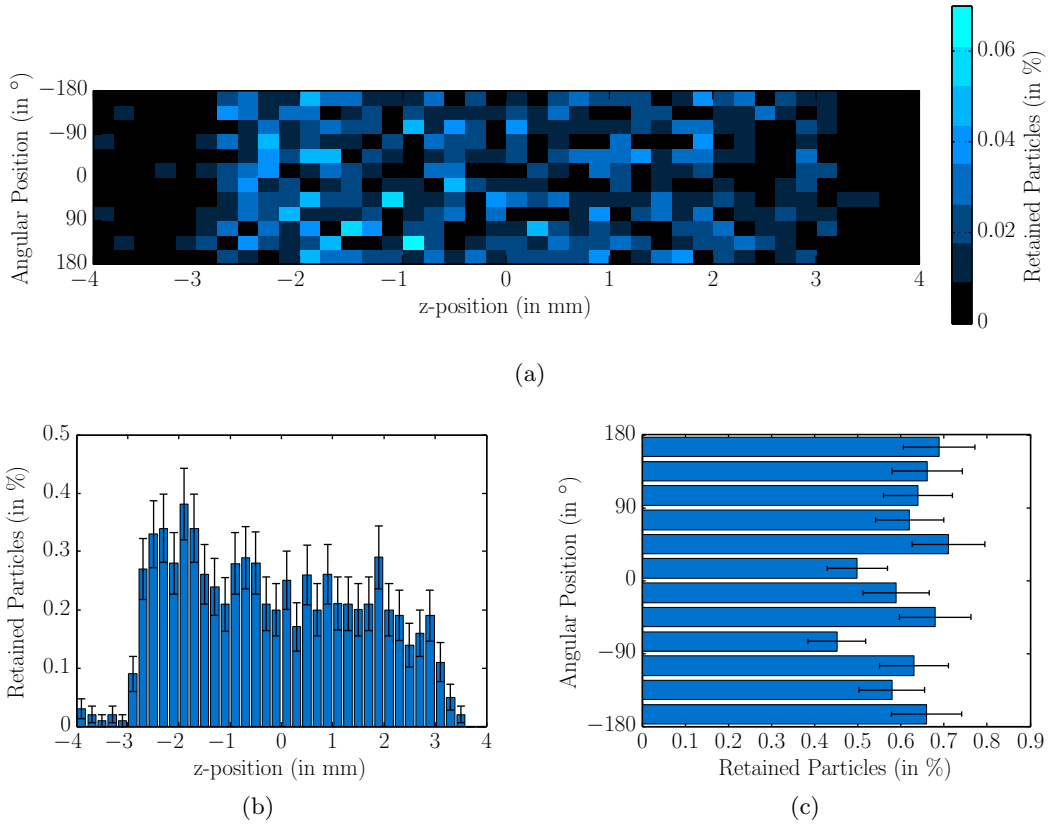

Figure 5.12: Percentage and location of the retained complexes in the target area with inclusion of minor forces; model aorta was cut lengthwise and "rolled out" (a): color indicates percent of retained complexes per position, where the sum over each column is shown in panel b and the sum over the rows in panel c

1 mm ($-4\,\text{mm} \leq z \leq 4\,\text{mm}$). The panels of figure 5.12 are arranged similar to figure 5.6. Panel (a) shows the model aorta, cut lengthwise on the lower side, rolled out and projected on a two-dimensional surface. The surface is subdivided into small rectangles with a side length of approximately 0.2 mm. The number of complexes retained in each rectangle in the simulation is counted and the resulting amount of complexes per rectangle is indicated in terms of color. The x-axis represents the z-position in mm and thus the length of the vessel; the y-axis shows the angular position, where an angle φ of zero corresponds to the upper side and an angle of $\pm 180°$ denotes the lower side. The sum of each column in figure 5.12a is depicted in figure 5.12b, therefore displaying the percentage of retained complexes per z-position; the sum over each row of figure 5.12a is shown in 5.12c, showing the percentage of retained complexes per angular position.
The total retention rate in the target region is approximately 7.4 % and thereby 0.5 % lower than without the inclusion of the minor forces considered here. Furthermore, the standard deviation of the total retention rate of 0.27 % is comparable to the results described above of 0.28 %. However, we can see that the accumulation is

more localized than before. While in the results presented above, 90 % of the retained particles were distributed over a length of 5.9 mm, here, they are distributed over only 5.3 mm. Especially on the left side of the target area, the retention rate is significantly lower. In fact, the low retention rate in the first millimeter of the target area is mainly responsible for the difference of 0.5 %.

5.4 Discussion

In this part of this work, we successfully developed several set-ups of permanent magnets in order to accumulate different lentivirus/nanoparticle complexes or nanoparticle-loaded cells. By calculating the trajectories of the nanoparticles, we obtained the localized particle distributions in the corresponding target areas. For our calculations, we took the different physical properties of the nanoparticle complexes or cells into account. We used the magnetic drug targeting model described in chapter 2.2 to determine the local accumulation of magnetic nanoparticles in a magnetic flux density field. In contrast to other works in this field [53, 54] where such problems were solved analytically or as non-accelerated models, we included physical particle and cell properties and approximated the experiments by simulating a high number of particles to reduce statistical fluctuations. Thereby, we were also able to include the whole size distribution of nanoparticle complexes and cells, instead of using only a mean diameter. Although, we only partly included contributions of minor forces and no interactions between particles or cells in our simulations, the results of the simulation are in good agreement with the experimental results.
We divided the simulations into a *static* and *dynamic model*, corresponding to the applied fluid dynamics. The calculation of particle trajectories in the *static model* is on the one hand a somewhat simplified version since flow related effects on the trajectory do not exist. On the other hand, several minor forces are, in comparison to the total force on the particle, more dominant. Apart from the frictional Stokes forces which always oppose the magnetic force, gravity may play a more important role. In a *dynamic model*, the fluidic forces usually dominate the movement and minor forces are negligible as shown in chapter 5.3.2.

Static Model

In contrast to the previously published results [109], the results presented here include gravity, Langevin magnetization behavior and influences of the horizontal shaker. Thereby, we took several minor forces into account which could have been responsible for the discrepancies between simulation and experiment.
However, in case of the cell targeting with the 200 µm tip described above, those considerations enlarge the discrepancy between simulation and experiment. Most likely, this discrepancy is founded in inaccuracies concerning the mass of the cells, the assumption of adhesion or further effects of the shaker. While we took the influence of the shaker while the cells were floating into account, we assumed that the cells adhere when they come in touch with the bottom of the cell culture dish. If the cells do not adhere instantaneously, they could further move along the bottom of the cell dish. The influence of additional lateral movement of the cells caused by the shaker could additionally influence the final attachment of cells, especially in regions with low magnetic forces. This effect could increase the amount of cells in regions with high magnetic gradients. Additionally, the influence of already adherent cells was not taken into account, because the trajectories and final positions were calculated for each cell individually. Attached cells could obstruct the movement of

other cells by building a "wall" of cells preventing additional cells from reaching the center of the magnetic tip.
Though the description of the horizontal shaker as a radial force is not fully representative, it is adequate description. The movement of the shaker is not rotational symmetric at every time step. The movement of the shaker is periodic and thereby, the asymmetry is equivalent to a temporal offset. Since starting positions are random and we are investigating a large time frame in contrast to the period, this description is valid.

Dynamic Model

In chapter 5.3, we developed a model to predict the number and position of particle complexes which can be retained by an external magnetic field. To compare the simulation with experimental results, we also calculated 30 passages of the fluid through the magnetic set-up. It can be seen in figure 5.7 that not all complexes can be retained. This behavior can be explained by the fact that the complexes for subsequent passages are the same ones as for previous passages with different starting positions. Those complexes with larger size and magnetic moment are likely to be retained in an early passage, leaving only the small complexes for the later passages. This effect can be seen particularly well in figure 5.7c where the larger complexes have a higher probability of getting retained, while the smaller complexes are mostly carried away.
Comparing the amount of retained complexes in experiment and simulation, we find a very good agreement. However, one has to keep in mind that the fraction of retained particles is determined in different ways for experiment and simulation. The experimental result represents the amount of iron, whereas in the simulation, the result refers to the number of particles. Those values are not directly comparable, since very large or very small particles are weighted differently in those methods. If we compare the experiment to the percentage of the volume of the particle complexes, we get a higher retention efficiency in the simulation. This discrepancy most likely originates in inaccuracies of the measured particle properties. It might also hint at a problem based on the assumption of a constant magnetic moment to volume rate, as is also indicated by the measurement result of chapter 4.2. This assumption is valid for individual particles, but the proportion might vary for particle complexes, due to the particle density in the complex. This variation in turn influences the mass as an input parameter.
However, we have also investigated the influences of the individual parameters and have given approximation for the resulting variation. On the one hand, this allows us to estimate the impact of potential inaccuracies for every parameter. For this purpose, we have given an individual discrepancy for a variation in the interval of $\pm 10\,\%$ around the value used in the non-parametric calculations. On the other hand, we are able to roughly predict the result for changed parameter sets.

On the point of the **particle parameters**, the largest influence is, predictably, the change of the particle diameter at a constant magnetization (figure 5.11c). This

occurs if the aggregation behavior of the nanoparticles changes, e.g. for different fluids / salt solutions (see also chapter 4.3.1) or the addition or viral particles. Another large influence is the variation of the magnetic moment / magnetization for a constant particle diameter (figure 5.11a). This effect can be achieved, e.g. by changing the core material. Overall, the parametric evaluation can help with the decision, whether a certain particle type is suitable for the experiment. In contrast to the previously published results in Heidsieck *et al* [164], the results include Langevin magnetization behavior and are not based on the assumption of magnetically saturated nanoparticles. While the overall retention rate varies only slightly in comparison to the previous results, it can be seen that variations in the particle parameters have a larger impact if the magnetization behavior is considered, e.g. a 7.5 times larger magnetic moment previously yielded a nearly 100 % retention rate, while now the retention rate is below 50 %. Additionally, we can now see another saturation behavior in figure 5.11c which was previously not noticeable. However, this behavior is not as prominent as it seems since we have to keep in mind that we are only looking at a certain part of the vessel. The amount of particles retained outside of the target area increases with large retention rates since more particles are retained sooner in their journey and thereby possibly before entering the target area. However, a saturation of approximately 96 % in the target area shows a retention rate of approximately 98 % in the whole area of the vessel. Nonetheless, not all of the particles are retained for the maximum investigated parameter. The constant value of the retention rate for variations of the nanoparticle mass (see figure 5.11d) can be explained as follows. If we rearrange the equation of motion (equation 2.41) into

$$\dot{\vec{v}} = \frac{1}{m}\vec{F}_{\mathrm{mag}} + \frac{1}{m}\vec{F}_{\mathrm{hydro}}\,, \tag{5.1}$$

as it is effectively done for solving the differential equation, it can be seen that each force gains the term of the inverse mass. By changing the mass, both forces are changed in the same way; hence, the influence of the mass is very small, resulting in a small change in the retention rate.

The results in this work also include the variation of the vessel diameter as a **geometric parameter**, thereby enabling the estimation of the retention rate for other small animals, e.g. in rat aortae. A targeting with the same particle type in a rat aorta (2.5 times the above used diameter) and a comparable flow velocity would achieve only a fifth of the above retention rate. However, for vessels of this size we would be able to improve the magnetic set-up and achieve a higher gradient than we assumed for the parametric investigation in figure 5.10. This would gain us approximately a factor two, so the retention rate would still be significantly smaller in a rat than in a mouse. To achieve a comparable retention rate a five times larger magnetic gradient would be necessary. Apart from those estimations, we have to keep in mind, that in case of very small vessels, e.g. capillaries, we can no longer use approach of calculating each trajectory individually. If the vessel diameter is no longer a great deal larger than the nanoparticles, already accumulated particles

influence the fluid flow to the point where they might block the vessel completely. Additionally, the local change of the magnetic flux density field due the magnetic dipole moment of the particles has a larger influence due to the smaller distances between the particles. However, the calculations can give us a valid starting point for further estimations. Additionally, we investigated the influence of the initial particle distribution, which is the overall largest influence on the retention rate. Since the magnetic moment and thereby the force on the complexes in this case strongly depends on their position, the influence of the distribution is very strong. While the velocity distribution of particles in flow converges to the flow velocity, the localized distribution of the particles is mostly unknown. Due to inertia forces, nanoparticles should accumulate in the center of the vessel. This is opposed by collisions between nanoparticles which is of course dependent on the particle concentration. However, for particles of the used order of magnitude, the inertia forces are too small to achieve any significant change in the particle distribution for realistic distances, for exemplary data see appendix A.2.1. Nonetheless, the experimental data shows that the retention rate is reproducible and thereby not susceptible to slight variation in the injection process, e.g. position or angle of the needle.

Additionally, we included a simulation including several **minor forces** (Brownian motion, inertia and gravity) and have seen that the result is comparable to the result without minor forces. We chose those three minor forces and continued to neglect other forces, since those three were comparably simple to implement into our algorithm. The simulation of e.g. diffusion, dipole interaction or collisions cannot be included in the current approach. At the moment, every particle trajectory is calculated individually and independently from the other particles. Forces based on the interaction of nanoparticles with each other would need a different approach. However, we have seen that the results with and without Brownian motion, inertia and gravity are consistent with each other within over 90 %. At the same time, the implementation of Brownian motion increases the computing time approximately by a factor 10. Due to the random movement at each time step, the ODE solver has problems with the adaption of its step size. We already reduced this influence by basing the seed for the random number generation is regenerated in each step on the current position and thereby making the random number sequence deterministic for each position.

In contrast to other groups [50, 52, 53], we were able to calculate trajectories for the purpose of a fully three dimensional analysis. We performed a three-dimensional simulation as shown in figure 5.6. To cut down on the computing time, we took advantage of the near symmetry of the set-up for the parameter runs and performed those as two dimensional simulations.
The assumption of particle complexes adhering at the vessel wall is valid in the area of the magnets as the magnetic force slightly exceeds the hydrodynamic force at the wall in this region. Furthermore, a real artery comes with a roughness of the surface which additionally holds the complex back.

We have successfully calculated the retention and accumulation of nanoparticles and found a good agreement with the experimental *in vitro* results. However, the presented results are not fully comparable to the targeting efficacy in biological flows *in vivo*. For those applications, several other aspects, like vessel dilatation or non-Newtonian flow properties have to be taken into account [27]. The dynamic viscosity which is inherent in blood flow, changes the hydrodynamic drag force in dependence of the vessel diameter. Additionally, the physical properties of the nanoparticles in blood might differ significantly from those in other fluids. Furthermore, a biological system introduces a time-dependency to the model via the varying flow rate and the motion of the tissue itself; thereby adding a fourth dimension to the equation of motion and complicating the calculation of the trajectories. Those aspects would have to be implemented into our simulations to achieve an accurate description of magnetic targeting in an *in vivo* environment of the cardiovascular system. Particularly regarding the magnetic targeting in the cardiovascular system, those factors are of great influence. In contrast to, e.g. models of tumors, aortae have comparably strong fluidic conditions. Blood flow in tumors tends to be slower than in the cardiovascular system and tumors commonly have small, but irregular vessel diameters. Additionally, an *in vivo* approach has some limitations as to accessibility and efficiency. Foremost, there are physical restrictions on the magnitude of the magnetic gradient *in vivo* because the magnetic flux density and thus the magnetic gradient declines rapidly with the distance between magnet and target. Furthermore, it is not possible with common magnetic set-ups to achieve a gradient maximum and thereby an efficient accumulation of nanoparticles at a distance from the magnet. This distance limitation makes magnetic targeting only feasible in applications close to the body surface or requires the usage of magnetizable implants, which generate high and local field gradients [35–38]. To overcome this limitation, imaging gradients of magnetic resonance imaging systems can be used for magnetic targeting inside the body [167].

Furthermore, the feasibility of targeting in a beating human heart is problematic from the technical point of view. Due to the high flow rates and the occurring eddies and vortices, a large magnetic force is necessary to retain the nanoparticles. At the current state of particle properties and magnetic field generators, such a targeting approach is on the edge between success and failure.

One way to increase the magnetic force would be to increase the magnetic gradient. However, this possibility is again limited due to the thickness of the heart tissue. The other way is to increase the magnetic moment of the nanoparticles. The magnetic moment of the nanoparticles depends on both, the material of the core and the core diameter. Hence, the use of core materials with higher intrinsic magnetic moments increases the magnetic moment of the nanoparticles. Among superparamagnetic compounds, magnetite already has the highest intrinsic magnetic moment ($4.1\mu_B$). Materials with higher intrinsic moments, like Gadolinium ($7\mu_B$) are usually paramagnetic at body temperature [13, 82]. However, the higher intrinsic magnetic moment does not necessarily lead to a better targeting efficacy, since paramagnetic materials usually have a smaller magnetization at the field strengths used for magnetic targeting than most superparamagnetic materials. For the same reasons, the

core diameter of the nanoparticles should only be increased up to a critical threshold diameter, compare also figure 2.1. Above the threshold, the particles start to show a more ferromagnetic than superparamagnetic behavior.
The magnetic moment of complexes or cells depends additionally on the number of incorporated nanoparticles. Increasing the size of the nanoparticle complexes reduces their ability to pass the capillary bed and leads to thrombosis [41–43]. Similarly, cells can intake only a certain and particle dependent amount of nanoparticles before a toxic amount is reached [168–170], i.e. *bovine pulmonary arterial endothelial cells (bPAECs)* can tolerate 200 $\mathrm{pg\ Fe/cell}$ of SO-Mag5 nanoparticles, while 100 $\mathrm{pg\ Fe/cell}$ of PEI-Mag2 triggers a significant decrease in cell viability[‡]. Despite those potential problems, a greater size of the complex is more likely to being retained and correlates with a larger amount of bound material. A possible enhancement could be the use of microbubbles containing magnetic nanoparticles [15] due their large number of incorporated nanoparticles and their flexibility which allows them to squeeze even through capillaries. Thereby a higher magnetic moment can be achieved while the risk for thrombosis is minimized.

Algorithm

Our numerical algorithm was created to be as generic as possible and does not depend on the actual geometry. The geometric boundaries can be defined as spline interpolations or analytic expressions in dependence on the coordinate system which can be cartesian or cylindrical for rotational symmetry. Thereby, we are able to utilize different and complex geometries. In the same way, the physical fields can be specified as spline interpolations or analytic expressions (e.g. Poiseuille flow). The geometry can also be defined as a function, returning an index which corresponds to different geometry domains.
However, the complexity and thereby the computing time of the trajectory calculation is highly dependent on the mathematical expression of the fields. The evaluation of a spline function at one point in space is directly dependent on the order of the spline and the corresponding number of knot points. More simple, analytic functions are usually much faster to calculate than splines. Additionally, with each dimension is not only the spline function more complex, but more splines have to be evaluated, e.g. one spline each for flow velocity in x, y and z direction. Thereby, the computing time increases drastically simply by adding an additional dimension.
The inclusion of time-dependent problems presents no problem in general. However, a time-dependent analysis would rapidly increase the computing time by adding additional complexity in the definition of the field and domain functions as well as introducing an additional dimension. An extension of the algorithm to include time-dependent magnetic fields is not problematic and only poses the challenge of a longer computing time. While the inclusion of a time-dependent geometry, e.g. the expansion and contraction of the aorta with the due to the changing flow caused by the heart rate, is generally also possible, it enhances the complexity of the fields

[‡]S. Rieck, Universität Bonn (personal communications)

drastically. A time-dependency has to be added to the domain field and the fluidic field. While the time dependency of a magnetic field is usually rather simple (e.g. often follows sinusoidal functions), the fluidic field has to include the additional radial forces at expansion and contraction of the aorta. Additionally, the solution of the differential equation and the interaction of fluid and geometry have to be finely tuned, so that no illogical situations appear, e.g. the particle "jumps" from the inside of the vessel to the outside during the contraction phase.
However, the algorithm enables us to perform simulations of nanoparticle trajectories on more complex geometries, like branched vessels or tumors, as long as we are able to produce satisfying results for magnetic flux density and fluid flow with Comsol Multiphysics.

6

Conclusion and Outlook

In this work, we studied the behavior and several characteristic properties of magnetic nanoparticles in different environments for the purpose of targeting them in vessels via an external magnetic field. We designed several magnetic set-ups for different applications, including measurement set-ups for the characterization of the magnetic moment of nanoparticles as well as experimental set-ups for specific particle accumulations *in vitro*.
We developed functional prototypes for the measurement of the magnetic moment of magnetically labeled objects of different size ranges. Larger objects like cells and microbubbles were observed directly with a microscope and their movement was evaluated with a custom tracking algorithm. Smaller objects like nanoparticles and their complexes, were observed indirectly via light transmission. The results were evaluated by matching simulated to experimental results.
Additionally, we investigated the stability and aggregation behavior of two particle types for different salt solutions and typically used buffered solutions.
For the purpose of *in vitro* experiments, we successfully developed several set-ups of permanent magnets in order to accumulate different lentivirus / nanoparticle complexes or nanoparticle-loaded cells. By calculating the trajectories of the nanoparticles, we obtained the localized particle distributions in the corresponding target areas. For our calculations, we took the measured physical properties of the nanoparticle complexes or cells into account. By simulating a high number of particles, we approximated the experiment and reduced statistical fluctuations. In contrast to other works in this field [53, 54], we included the whole size distribution of nanoparticle complexes and cells, instead of using only a mean diameter. Furthermore, we included gravitational forces and conducted three dimensional analyses where appropriate. We were able to predict the amount and location of the accumulated particles and verified our model by comparing those simulations with the respective experiments. In the course of those simulations, we also analyzed the influence of different particle properties on the accumulation result.

Gene and drug targeting of the vasculature offers numerous therapeutic possibilities. By associating therapeutic viruses, DNA or drugs to magnetic nanoparticles and retaining them at a specific site using external magnetic fields, the systemic side effects of the therapy can be reduced and efficiency enhanced. While the specific

procedures and bound agents may vary, the overall goal of the magnetic drug targeting approach, from the medical point of view, is to deliver drugs or genetic material to a specific location and accumulate it there. To achieve this goal, a knowledge and understanding of the underlying processes, as the local conditions, the required magnetic set-ups as well as the particle properties is essential.
With the help of the calculated trajectories of the nanoparticle complexes, the influencing parameters were investigated and the process of constructing and optimizing targeting magnets was simplified. With this approach, fewer prototypes and experiments are necessary to optimize a set-up for a specific goal. Additionally, the simulations can help to decide if a particle type is suitable for a certain application or how a particle has to be composed, in terms of core size and material as well as hydrodynamic size, for an efficient targeting. For the calculation of the trajectories of the nanoparticles and therefore for the estimation of the accumulation, it is necessary to know the physical and magnetic properties of the corresponding particles or particle complexes.
To enhance the magnetic drug targeting efficacy and predictability, the primary point should therefore be to improve the nanoparticle stability, characterization and consistency. The benefit of an accurate description and simulation of the targeting process is only of limited use, if the behavior and inherent properties of the employed nanoparticles are not well-known. As we have seen in our simulations, the accumulation result can be unstable against variations of certain input parameters; thereby reducing the reproducibility of the results, if the particle properties vary too strongly.
However, there is often a lack of information concerning the magnetic properties of the nanoparticles. Many manufacturers do not include such information about their products. Frequently, only chemical properties, like surface coating, iron concentration, etc are given. Those properties are certainly important, but depending on the application, a complete description of the nanoparticles is necessary. Moreover, the different properties of the nanoparticles can vary from batch to batch. Our experiences have shown that this is the case even for commercially available nanoparticles. Depending on what the "characteristic" properties of the particles are, those properties are comparably stable, while other properties are neglected and can vary strongly.
Furthermore, there is a lack of systematically investigated influences on the particle behavior. Most examinations focus on different applications, e.g. the dissolution and sedimentation of nanoparticles in the ground water [154, 157]. Even though those effects follow the same mechanism, the specific influences might not be critical or even of interest for other applications. While often only the influence of certain salts is of geological or environmental interest, medical and biological applications may focus on a broader range of ions and combinations thereof. Especially the behavior of nanoparticles in physiological buffers and solutions needs to be investigated, as we have seen that the stability of nanoparticles is highly dependent on the composition of the used solution. The formation of complexes in the studied solutions and the changes in the behavior of the nanoparticle complexes have to be investigated.

To approach this problem, we developed two devices to measure the magnetic moment of cells, microbubbles, nanoparticles and their complexes. Even though we gain no high precision results with those devices, we achieve a comparability between different particle and carrier types. Furthermore, we can characterize the particle behavior in a magnetic field in dependency of the fluid.

With the right type of nanoparticle, the magnetic targeting of drugs and genes offers numerous therapeutic possibilities and has, within its limitations, many potential applications. By employing trajectory calculations, it is possible to assess the feasibility of targeting experiments in dependence on the particle and carrier type and enhance their success rate.
However, to make the magnetic drug targeting approach truly feasible, the quality, stability and reproducibility of the nanoparticles needs to be improved. The measurement devices, which have been presented in this work, can help to characterize nanoparticles and their carriers with regard to their magnetic properties. Using this information, simulations can aid in developing successful targeting techniques while minimizing the risk for setbacks.

A

Appendix

A.1 Fitting Functions and Parameters

A.1.1 Magnetization Curves

To fit magnetization curves on experimental data, we use either an inverse tangent function which is suitable for hysteresis, or a hyperbolic cotangent function known as Langevin function for superparamagnetic behavior

$$f(x) = a_f \cdot \operatorname{atan}\left(b_f x\right) + c_f \cdot x\,, \tag{A.1}$$

$$g(x) = a_g \cdot \left(\coth\left(b_g x\right) - \frac{1}{b_g x}\right) + c_g \cdot x\,. \tag{A.2}$$

Both functions include an additional linear term to allow for paramagnetic contributions. To estimate the initial parameters, we proceed similar to Perez-Rojas [171]. Based on the slope m and coordinates x, y of the data at small values (indicated by the subscript 0) and near saturation (indicated by sat), we gain the coordinates of the intersection point (is) of both slopes. Figure A.1 shows the construction of the auxiliary parameters $m_0, x_{\mathrm{is}}, y_{\mathrm{is}}, m_{\mathrm{sat}}, x_{\mathrm{sat}}, y_{\mathrm{sat}}$ and the resulting curve of $f(x)$ with and without linear contribution. Taking those values as scaling factors and taking

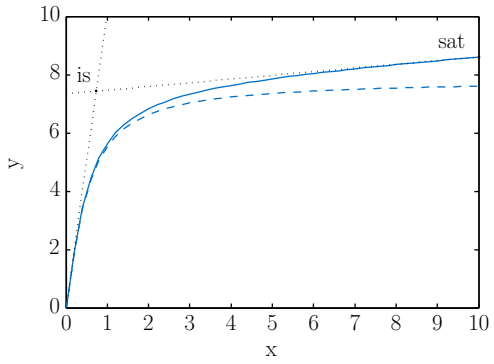

Figure A.1: Fit of a magnetization curve on an inverse tangent function based on slopes; continuous line denotes the fully fitted function and dashed line shows the result without linear contribution.

the limits of the function and its derivative at zero and for x going to infinity into account, we gain

$$a_f = \frac{2}{\pi} y_{\text{is}} \qquad a_g = y_{\text{is}} \tag{A.3}$$

$$b_f = \frac{\pi}{2} \frac{m_0}{y_{\text{is}}} \qquad b_g = 3\frac{m_0}{y_{\text{is}}} \tag{A.4}$$

$$c_f = \frac{y_{\text{sat}} - a_f \cdot \operatorname{atan}\left(b_f x_{\text{sat}}\right)}{x_{\text{sat}}} \qquad c_g = \frac{y_{\text{sat}} - a_g \left(\coth\left(b_g x_{\text{sat}}\right) - 1/b_g x_{\text{sat}}\right)}{x_{\text{sat}}} \tag{A.5}$$

In contrast to Perez-Rojas, we adjust the value for b by replacing y_{sat} with y_{is}. Otherwise, this would suggest that any slope at saturation is based purely on the linear term. This may hold true, if we have measurement data for very large values of x and/or the linear term is dominant, but those assumptions do not apply in our measurements.
Based on those initial parameters, we can refine the fitting results with MATLAB.

A.1.2 Distributions

Normal Distribution We use the following formulation for the probability density function of normal distributions

$$f(x) = \frac{1}{\sqrt{2\pi}\sigma} \exp\left(- \frac{(x-m)^2}{2\sigma^2} \right) , \tag{A.6}$$

where m and σ denote the mean value and standard deviation of the distribution, respectively.

Lognormal Distribution For the probability density function of lognormal distributions, we use the following formulation

$$f(x>0) = \frac{1}{\sqrt{2\pi}\varsigma x} \exp\left(- \frac{(\ln(x) - \mu)^2}{2\varsigma^2} \right) , \tag{A.7}$$

where μ and ς are the parameters of the distribution which relate to the mean m, the standard deviation σ and the peak value x_{peak} by

$$m = \exp\left(\mu + \frac{\varsigma^2}{2} \right) , \tag{A.8a}$$

$$\sigma^2 = \exp\left(2\mu + \varsigma^2\right) \left(\exp\left(\varsigma^2\right) - 1 \right) , \tag{A.8b}$$

$$x_{\text{peak}} = \exp\left(\mu - \varsigma^2\right) . \tag{A.8c}$$

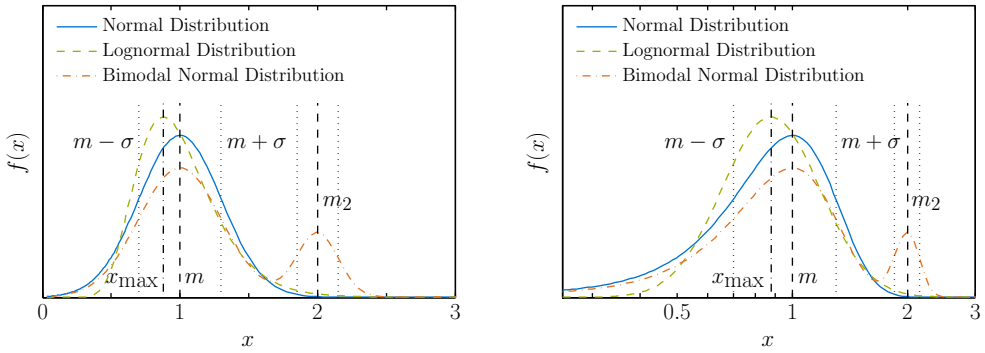

(a) (b)

Interval		Fraction of set
normal	lognormal	
$m \pm \sigma$	$\exp(\mu \pm \varsigma)$	68.27 %
$m \pm 2\sigma$	$\exp(\mu \pm 2\varsigma)$	95.45 %
$m \pm 3\sigma$	$\exp(\mu \pm 3\varsigma)$	99.73 %

(c)

Figure A.2: Exemplary normal and lognormal distributions with the same mean value and standard deviation, as well as bimodal normal distribution with a second peak in linear (a) and logarithmic scaling (b); approximate amount of the set found in intervals around the mean value (c)

Multimodal Distributions For distributions with more than one mode, we use the following formulation [172]

$$f(x > 0) = \sum_{i=1}^{n} w_i f_i(x)\,, \tag{A.9a}$$

$$\sum_{i=1}^{n} w_i = 1\,, \tag{A.9b}$$

which describes a mixture of either normal or lognormal probability density functions $f_i(x)$ weighted by w_i. The different modes appear as distinguishable peaks in the probability density function.

Fitting Procedure To gain a good fit result for lognormal distributions with MATLAB, we transform the coordinates in the following way

$$f' = f \cdot x\,, \tag{A.10a}$$

$$x' = \ln(x)\,, \tag{A.10b}$$

and thereby can redefine equation A.7 to

$$f' = \frac{1}{\sqrt{2\pi}\varsigma}\exp\left(-\frac{(x'-\mu)^2}{2\varsigma^2}\right), \tag{A.11}$$

instead of equation A.7. Equation A.11 has again the general shape of a normal distribution and is more suitable for typical fitting algorithms. Furthermore, the MATLAB fit routine often prefers x values of order 10^0 to 10^1. Thereby, it is often helpful to additionally rescale the coordinates to smaller values and accordingly larger f values for a good fit result. Subsequently, the calculated parameters have to be transformed accordingly.

Exemplary distributions Figure A.2 exemplarily shows a normal and a lognormal distribution as well as bimodal normal distribution in linear and logarithmic scaling. We chose a mean value $m = 1$ and a standard deviation $\sigma = 0.3$ for both monomodal distributions. The bimodal distribution has one peak with the same parameters as the monomodal distributions and another peak with a mean value $m = 2$ and a standard deviation $\sigma = 0.15$. The peaks are weighted with 0.8 and 0.2, respectively. Mean value and standard deviation are denoted as black dashed and dotted lines, respectively. Additionally, the peak value $x_{\text{peak}} \approx 0.88$ of the lognormal distribution is indicated by a dash-dotted line.
While the normal distribution is symmetric when displayed in linear scaling and mean and peak value coincide, the lognormal distribution shows asymmetric behavior. When displayed in logarithmic scaling, the lognormal distribution presents the same shape as the normal distribution on linearly scaled axes. However, the peak and mean value do not agree. The peak value is always smaller than the mean value. Statistically, 99.73 % of the set of the normal distribution are inside the interval of $m \pm 3\sigma$. For a lognormal distribution this interval changes to $\exp\left(\mu \pm 3\varsigma\right)$ which is also asymmetric.

A.1.3 Chi-Square Fitting

To estimate N physical observables $a_{j=1,\ldots,N}$ based on a set of data points x_i, y_i, we can use a χ^2 fitting procedure by minimizing [133]

$$\chi^2 = \sum_i \left(\frac{y_i - \mathcal{M}(x_i, a_{1,\ldots,N})}{\sigma_i}\right)^2, \tag{A.12}$$

where we fit the data points to a model function $\mathcal{M}(x, a_{1,\ldots,N})$. Hereby, the parameter χ^2 is a measure for the goodness of the fit and is minimized with respect to the parameters a_j

$$\frac{d\chi^2}{da_j} = 0\,. \tag{A.13}$$

A.2 Additional Numerical Results

A.2.1 Influence of Inertia Forces

Figure A.3 exemplarily shows the distribution of nanoparticles under the influence of inertia forces in flow. Figure A.3a shows the development of the particle distribution for initially uniformly distributed particles, while in figure A.3b, the particles were normally distributed with the vessel radius corresponding to 2σ. Both figures display the changed distribution resulting after a certain distance under the influence of inertia forces. We used fluid properties identical to chapter 5.3 ($u_{\text{in}} = 5\,{}^{\text{ml}}/_{\text{min}}$, $d_{\text{vessel}} = 0.75\,\text{mm}$). However, to better demonstrate the effect, we used a monodisperse particle distribution with a diameter of $100\,\mu\text{m}$. For smaller particles, much longer distances are needed to achieve a change in the radial distribution, and for very small particles ($d \lesssim 100\,\text{nm}$), the effect disappears in the numerical rounding.

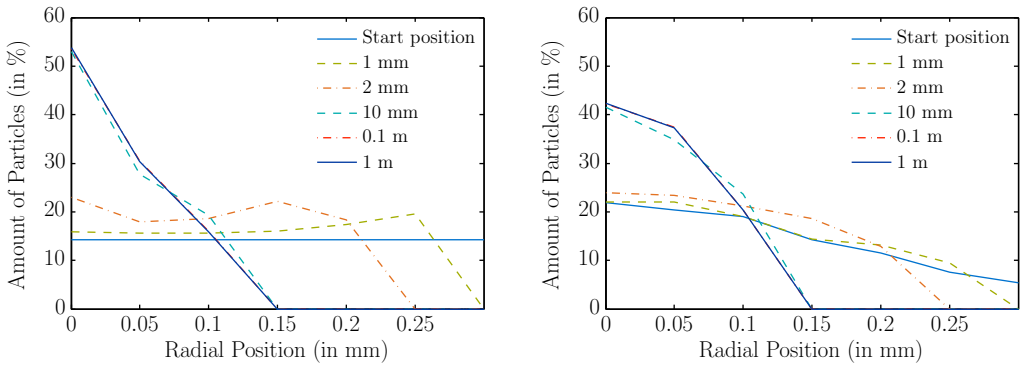

(a) (b)

Figure A.3: Development of particle distribution under the influence of inertia forces in flow at different covered distances for initial uniform (a) and normal (b) distribution

A.2.2 Disregard of Acceleration

Figure A.4 shows the covered distance and velocity for exemplary particle complexes or cells in a magnetic field comparable to the field of the cell culture dish set-up shown in figure 4.1. The object has a diameter of $10\,\mu\text{m}$, a magnetic moment of $500\,\text{fAm}^2$ and has its initial position at a distance of $1\,\text{mm}$ from the center. Figure A.4a shows the distance covered by the objects for different set-ups of the differential equation. The blue and green line indicate the distance if the acceleration of the particles is disregarded, while the pink and orange line show the same in case the acceleration is taken into account. In the same way, the dashed lines show saturated objects, while the Langevin behavior is considered with $\mathcal{E} = 70$ for the continuous lines.
Figure A.4c shows the magnetic moment calculated without taking the acceleration

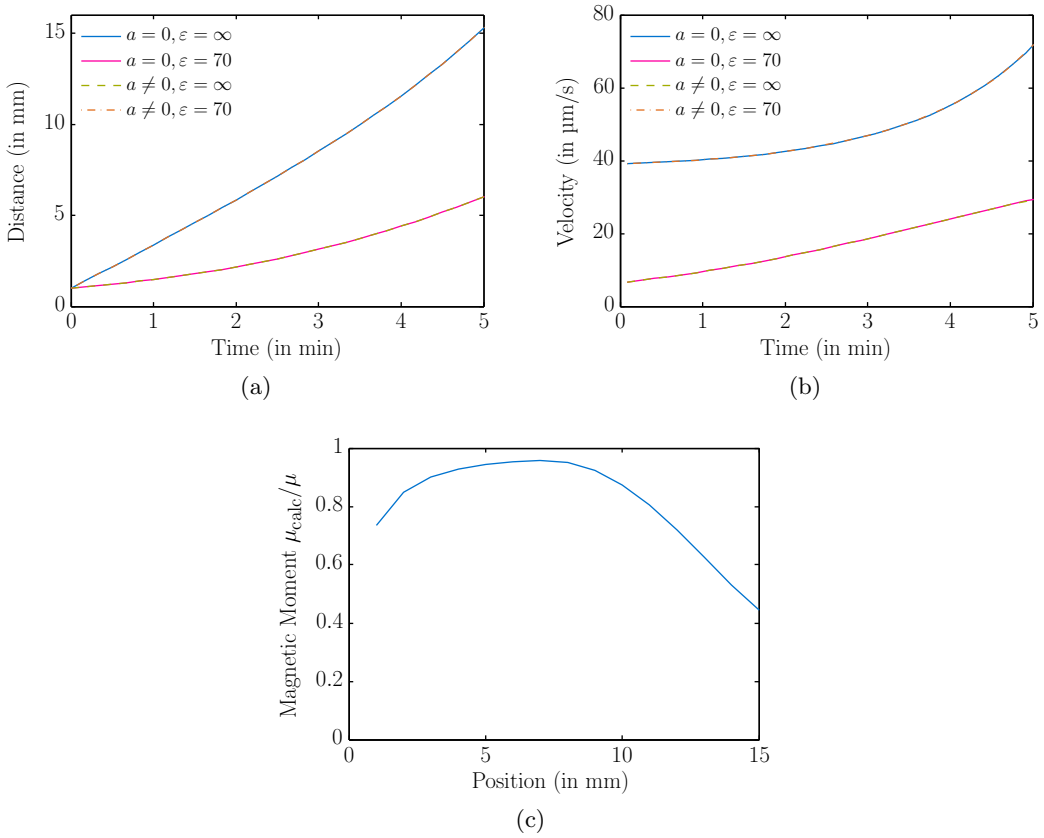

Figure A.4: Comparison of covered particle distance (a) and velocity (b) with and without acceleration and with saturated and-non saturated particles and magnetic moment calculated from data

into account, but based on the accelerated curve. The result is shown relative to the originally used magnetic moment. While velocity and thereby distance vary greatly, the magnetic moment shows better results in the region between 4 and 9 mm.

A.3 Reference Lists

A.3.1 Orders of Magnitude for Biological Components

Component	Size Range
Proteins	5–10 nm
Genes	10–100 nm
Viruses	20–450 nm
Cells	5–100 µm
Red blood cells (spherical)	6–8 µm
White blood cells	10–20 µm
Platelets	2–3 µm

Table A.1: Orders of magnitude for biological components [31]

A.3.2 Grades of Permanent Magnets

In this work, we used only rare-earth magnets made of NdFeB. Those are commonly classified by a combination of letters and numbers, e.g. *N50, 40M, 35SH* etc. While the letters refer to maximum working temperature and other properties, the number denotes the inner remanent flux density. The remanent flux densities for the different grades listed below [hkc].

Grade	Mean remanent flux density (in T)
35	1.195
38	1.235
40	1.265
42	1.30
45	1.345
48	1.40
50	1.425
52	1.455

Table A.2: Magnetic grades for NdFeB permanent magnets

A.3.3 Properties of Salt and Buffered Solutions

The following table lists the relevant properties of different solutions for exemplary concentrations. The listed viscosities and refractive indices were determined by the

ZetaSizer Software based on their components and are shown for a temperature ranging between 18 and 26 °C in figure A.5. pH values are measured or, in case of water, literature values.

Fluid	I (in mM)	pH†	pH‡	η (in mPa·s)	n
Water	0	(7)	6.2	0.954	1.330
DPBS	166.37	7.4	7.4	0.969	1.332
HBSS modified	155.9	7.2	7.3	0.924	1.332
NaCl (I =100 mM)	100	6.2	6.5	0.964	1.331
$CaCl_2$ (I =100 mM)	100	6.1	5.9	0.974	1.331
$NaHPO_4$ (I =100 mM)	100	7.2	7.2	1.012	1.330
10 % Glycerol	–	4.1	–	1.235	1.341

Table A.3: Properties of different solutions; values are given at 22 °C; pH values are given without nanoparticles† and with an iron content of 25 $\mu g\ Fe/ml$ SO-Mag5 nanoparticles‡; viscosity and refractive index according to ZetaSizer Software [zet]

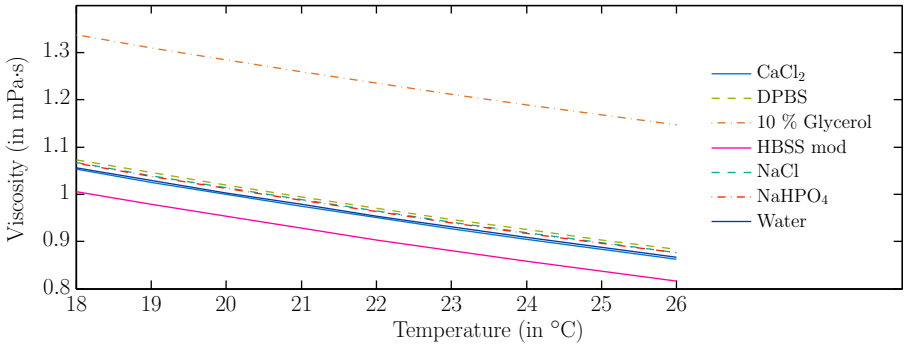

Figure A.5: Viscosities of different solutions

A.3.4 Lists of Symbols and Abbreviations

Abbreviations

BMC	bone marrow cell
bPAEC	bovine pulmonary arterial endothelial cell
DLS	dynamic light scattering
DPBS	Dulbecco phosphate buffered saline
eCM	embryonic cardiomyocyte
ES-CM	embryonic stem cell-derived cardiomyocyte
FEM	finite element method
HBSS	Hanks balanced salt solution
LED	light-emitting-diode
MC	Monte-Carlo
MDT	magnetic drug targeting
MMB	magnetic microbubbles
MNP	magnetic nanoparticles
MRI	magnetic resonance imaging
PEI	polyethyleneimine
PMMA	polymethyl methacrylate
PS	polystyrene
SO	silicon oxide

Symbols and Nomenclature

Nomenclature

$\vec{X}$	vectorial parameter
$\lvert\vec{X}\rvert$, X	absolute value of $\vec{X}$
$\hat{X}$	unity vector in direction of $\vec{X}$
$\bar{X}$	mean value of X
$\dot{X}$	time derivative of X
ΔX	difference between different values of X

Functions and Operators

∇	Nabla differential operator
f	arbitrary function
H	histogram of a set
h_m	spherical Hankel function with index m
$\mathcal{H}$	Heaviside function
j_m	spherical Bessel function with index m
J	Saffman expression
$\mathcal{L}$	Langevin function
$\mathfrak{R}$	real component
$\mathcal{M}$	Model function

Subscripts

A	area / surface
core	core
cyl	cylinder
crit	critical
c_-, c_+, c_m	lower, upper and medium critical value
h, hydro	hydrodynamic
edl	electric double layer
k	pixel index
mag	magnetic
m	expansion order of Bessel / Hankel function
m	image index
n	object index
p	object index
prt	particle
φ	angular
r	radial component
rem	remanent
sol	solvent
sat	saturation
t	trajectory index
V	volume
vdW	van der Waals
x, y, z	concerning the coordinate x, y, z
0	inital value

Constants

k_B	Boltzmann constant
μ_0	permeability of vacuum
ε_0	permittivity of vacuum
$\vec{g}$	acceleration in the gravity field of the earth
e	elementary charge
N_A	Avogadro constant

Parameters

a, b, c	arbitrary constants
A	area / surface
$\vec{A}$	magnetic vector potential
A_H	Hamaker constant
$\mathcal{A}$	absorption
a_m	Mie coefficient
α	absorption coefficient
$\vec{B}$, B	magnetic flux density
$\mathcal{B}$	image
b_m	Mie coefficient
β	power law index
C	concentration
$\vec{c}$	coordinates of centroid
$\dot{\gamma}$	shear rate
χ	minimization parameter
D	diffusion coefficient
$\vec{D}$	electric displacement field
$\Delta_{A,C,I}$	peak parameters
d	diameter
δ	aperture
$\vec{E}$	electric field
$\mathcal{E}, \mathcal{E}'$	Langevin parameter
ε	dielectric permittivity
ϵ	extinction coefficient
η	dynamic viscosity of fluid
$\vec{F}$	force
$\mathcal{F}$	filter
f	frame rate
f	normalization factors
G	weight of edge
$\vec{H}$	magnetic field
ϑ	Saffman parameter
I	ionic strength
$\mathcal{I}$	intensity
$\vec{j}$	current density
k	Halbach index
k	flow consistency index
κ	inverse Debye length
L	boundaries
Λ	relaxation time constant
λ	wave length
$\vec{M}$, M	magnetization
m	mean value
m	slope
m	mass
$\vec{\mu}$, μ	magnetic moment
μ	Casson rheological constant
μ	permeability
μ	lognormal parameter
N	number of objects
$\mathcal{N}$	noise level
$\vec{n}$	normal vector
n	refractive index
ν	kinematic viscosity of fluid
ν_e	electronic absorption frequency
Ω	rotational angular speed
p	pressure
$p_{1,2,3}$	arbitrary constants
Pe	Peclet number
$\mathcal{P}_n$	pixel set of object n
φ	angle
ψ_0	surface potential
Φ	overall angle
r, R	radius, radial position
Re	Reynolds number
ρ	charge density
ϱ	density of fluid
$\mathcal{S}$	sobel filtered image
s	distance
σ	standard deviation
σ_E	extinction cross section
ς	lognormal parameter
T	temperature
$\mathcal{T}$	transmission
t	time
τ	yield stress
$\vec{u}$	flow velocity
V	volume
$\vec{v}$	velocity
$\Delta\vec{v}$	relative velocity
W	potential
$\mathcal{W}$	width
w	weight
$\vec{x}$	position
ζ	zeta potential

List of Figures

List of Tables

List of Manufacturers

[aks] AK Steel GmbH. Köln, Germany.

[bay] Bayer Schering Pharma AG. Berlin, Germany.

[bio] Biochrom AG. Berlin, Germany.

[bra] BRAND GmbH & Co KG. Wertheim, Germany.

[che] Chemicell GmbH. Berlin, Germany.

[com] Comsol Multiphysics GmbH. Göttingen, Germany.

[gue] Guerbet. Villepinte, France.

[ham] Hamamatsu Photonics K K. Hamamatsu-shi, Shizuoka, Japan.

[hkc] HKCM Engineering. Eckernförde, Germany.

[m4u] magnets4you GmbH. Lohr a. Main, Germany.

[mag] MagForce AG, The Nanomedicine Company. Berlin, Germany.

[mat] MathWorks. Natick, MA, USA.

[oce] Ocean Nanotech. Springdale, AR, USA.

[pur] Pure Devices GmbH. Würzburg, Germany.

[qua] Quantum Design, Inc. San Diego, CA, USA.

[si] SI Analytics GmbH. Mainz, Germany.

[sie] Siemens Water Technologies. Barsbüttel, Germany.

[sig] Sigma-Aldrich Co LLC. St. Louis, MO, USA.

[spe] Analytik Jena. Jena, Germany.

[the] Thermo Fisher Scientific Inc. Waltham, MA, USA.

[tpp] TPP Techno Plastic Products AG. Trasadingen, Switzerland.

[zei] Carl Zeiss AG. Oberkochen, Germany.

[zet] Malvern Instruments Ltd. Malvern, UK.

Bibliography

[1] Y. A. Garbovskiy and A. V. Glushchenko. Liquid Crystalline Colloids of Nanoparticles: Preparation, Properties, and Applications. In R. E. Camley and R. L. Stamps, editors, *Solid State Physics*, volume 62 of *Solid State Physics*, pages 1–74. Academic Press, 2010. doi: 10.1016/B978-0-12-374293-3.00001-8.

[2] B. Wu, Y. Kuang, X. Zhang, and J. Chen. Noble Metal Nanoparticles/Carbon Nanotubes Nanohybrids: Synthesis and Applications. *Nano Today*, 6(1):75–90, 2011. ISSN 1748-0132. doi: 10.1016/j.nantod.2010.12.008.

[3] B. Nowack and T. D. Bucheli. Occurrence, Behavior and Effects of Nanoparticles in the Environment. *Environ Pollut*, 150(1), 2007. doi: 10.1016/j.envpol.2007.06.006.

[4] W.-T. Liu. Nanoparticles and Their Biological and Environmental Applications. *J Biosci Bioeng*, 102(1):1–7, 2006. doi: 10.1263/jbb.102.1.

[5] S. J. Klaine, P. J. Alvarez, G. E. Batley, T. F. Fernandes, R. D. Handy, D. J. Lyon, M. J. McLaughlin, and J. R. Lead. Nanomaterials in the Environment: Behavior, Fate, Bioavailability and Effects. *Environ Toxicol Chem*, 27:1825–1851, 2008. doi: 10.1897/08-090.1.

[6] L. R. Khot, S. Sankaran, J. M. Maja, R. Ehsani, and E. W. Schuster. Applications of Nanomaterials in Agricultural Production and Crop Protection: A Review. *Crop Prot*, 35:64–70, 2012. doi: 10.1016/j.cropro.2012.01.007.

[7] F. E. Kruis, H. Fissan, and A. Peled. Synthesis of Nanoparticles in the Gas Phase for Electronic, Optical and Magnetic Applications – A Review. *J Aerosol Sci*, 29(5–6):511–535, 1998. doi: 10.1016/S0021-8502(97)10032-5.

[8] I. Matsui. Nanoparticles for Electronic Device Applications: A Brief Review. *J Chem Eng Japan*, 38(8):535–546, 2005.

[9] J. Liqiang, S. Xiaojun, S. Jing, C. Weimin, X. Zili, D. Yaoguo, and F. Honggang. Review of Surface Photovoltage Spectra of Nano-Sized Semiconductor and its Applications in Heterogeneous Photocatalysis. *Sol Energ Mat Sol C*, 79(2): 133–151, 2003. doi: 10.1016/S0927-0248(02)00393-8.

[10] S. M. Gupta and M. Tripathi. A Review of TiO_2 Nanoparticles. *Chinese Sci Bull*, 56(16):1639–1657, 2011. doi: 10.1007/s11434-011-4476-1.

[11] J. Pardeike, A. Hommoss, and R. H. Müller. Lipid Nanoparticles (SLN, NLC) in cosmetic and pharmaceutical dermal products. *Int J Pharm*, 366(1–2):170–184, 2009. doi: 10.1016/j.ijpharm.2008.10.003.

[12] Q. A. Pankhurst, N. K. T. Thanh, S. K. Jones, and J. Dobson. Progress in Applications of Magnetic Nanoparticles in Biomedicine. *J Phys D Appl Phys*, 42, 2009. doi: 10.1088/0022-3727/42/22/224001.

[13] S. P. Gubin. *Magnetic Nanoparticles*. Wiley-VCH, 2009. ISBN 3527407901.

[14] Q. A. Pankhurst, J. Connolly, S. K. Jones, and J. Dobson. Applications of Magnetic Nanoparticles in Biomedicine. *J Phys D Appl Phys*, 36(13):167, 2003.

[15] H. Mannell, J. Pircher, T. Rathel, K. Schilberg, K. Zimmermann, A. Pfeifer, O. Mykhaylyk, B. Gleich, U. Pohl, and F. Krotz. Targeted Endothelial Gene Delivery by Ultrasonic Destruction of Magnetic Microbubbles Carrying Lentiviral Vectors. *Pharm Res*, 29, 2012. doi: 10.1007/s11095-012-0678-8.

[16] Y. Sanchez-Antequera, O. Mykhaylyk, N. P. van Til, A. Cengizeroglu, J. H. de Jong, M. W. Huston, M. Anton, I. C. Johnston, Z. Pojda, G. Wagemaker, and C. Plank. Magselectofection: An Integrated Method of Nanomagnetic Separation and Genetic Modification of Target Cells. *Blood*, 117:e171–e181, 2011. doi: 10.1182/blood-2010-08-302646.

[17] C. Plank, U. Schillinger, F. Scherer, C. Bergemann, J.-S. Remy, F. Krötz, M. Anton, J. Lausier, and J. Rosenecker. The Magnetofection Method: Using Magnetic Force to Enhance Gene Delivery. *Biol Chem*, 384(5):737–747, 2003. doi: 10.1515/BC.2003.082.

[18] C. Plank, O. Zelphati, and O. Mykhaylyk. Magnetically Enhanced Nucleic Acid Delivery. Ten Years of Magnetofection – Progress and Prospects. *Adv Drug Deliver Rev*, 63(14-15):1300–1331, 2011. doi: 10.1016/j.addr.2011.08.002.

[19] R. E. Rosensweig. *Ferrohydrodynamics*. Dover Publications, 1997. ISBN 0486678342.

[20] J. T. Kemshead and J. Ugelstad. Magnetic Separation Techniques: Their Application to Medicine. *Mol Cell Biochem*, 67(1):11–18, 1985. doi: 10.1007/BF00220980.

[21] A. Ebner, J. Ritter, and H. Ploehn. Feasibility and Limitations of Nanolevel High Gradient Magnetic Separation. *Sep Purif Technol*, 11(3):199–210, 1997. doi: 10.1016/S1383-5866(97)00021-X.

[22] M. Arruebo, M. Valladares, and A. Gonzalez-Fernandez. Antibody-Conjugated Nanoparticles for Biomedical Applications. *J of Nanomater*, 2009, 2009. doi: 10.1155/2009/439389.

[23] K. E. Scarberry, E. B. Dickerson, J. F. McDonald, and Z. J. Zhang. Magnetic Nanoparticle-Peptide Conjugates for *in Vitro* and *in Vivo* Targeting and Extraction of Cancer Cells. *J Am Chem Soc*, 130(31):10258–10262, 2008. doi: 10.1021/ja801969b.

[24] M. Hosokawa, K. Nogi, M. Naito, and T. Yokoyama. *Nanoparticle Technology Handbook*. Elsevier, Amsterdam, 2007. ISBN 978-0-444-53122-3.

[25] C. Alexiou, R. Jurgons, R. J. Schmid, A. Hilpert, C. Bergemann, G. Parak Fritz, and H. Iro. In vitro and *in vivo* Investigations of Targeted Chemotherapy with Magnetic Nanoparticles. *J Magn Magn Mater*, 293:389–393, 2005.

[26] C. Alexiou, W. Arnold, R. J. Klein, G. Parak Fritz, P. Hulin, C. Bergemann, W. Erhardt, S. Wagenpfeil, and S. Luebbe Andreas. Locoregional Cancer Treatment with Magnetic Drug Targeting. *Cancer Res*, 60:6641–6648, 2000.

[27] B. Gleich, T. Weyh, and B. Wolf. Magnetic Drug Targeting: an Analytical Model for the Influence of Blood Properties on Particle Trajectories. *Appl Rheol*, 18(5):52023, 2008. doi: 10.3933/ApplRheol-18-52023.

[28] P. Dames, B. Gleich, A. Flemmer, K. Hajek, N. Seidl, F. Wiekhorst, D. Eberbeck, I. Bittmann, C. Bergemann, T. Weyh, L. Trahms, J. Rosenecker, and C. Rudolph. Targeted Delivery of Magnetic Aerosol Droplets to the Lung. *Nat Nanotechnol*, 2:495–499, 2007. doi: 10.1038/nnano.2007.217.

[29] K. Maier-Hauff, R. Rothe, R. Scholz, U. Gneveckow, P. Wust, B. Thiesen, A. Feussner, A. V. Deimling, R. Felix, and A. Jordan. Intracranial Thermotherapy Using Magnetic Nanoparticles Combined with External Beam Radiotherapy: Results of a Feasibility Study on Patients with Glioblastoma Multiforme. *J Neuro Oncology*, 81:53–60, 2007.

[30] Q. Wang and J. Liu. Nanoparticles Enhanced Hyperthermia. In *Intracellular Delivery*, volume 5 of *Fundamental Biomedical Technologies*, pages 567–598. Springer Netherlands, 2011. ISBN 978-94-007-1247-8. doi: 10.1007/978-94-007-1248-5-20.

[31] K. M. Krishnan. Biomedical Nanomagnetics: A Spin Through Possibilities in Imaging, Diagnostics, and Therapy. *IEEE Trans Magn*, 46(7):2523–2558, 2010. doi: 10.1109/TMAG.2010.2046907.

[32] C. Rümenapp, B. Gleich, and A. Haase. Magnetic Nanoparticles in Magnetic Resonance Imaging and Diagnostics. *Pharm Res*, 29:1165–1179, 2012. doi: 10.1007/s11095-012-0711-y.

[33] M. S. K. Nanoparticles in Modern Medicine: State of the Art and Future Challenges. *Int J Nanomedicine*, 2:129–41, 2007.

[34] H. An and B. Jin. Prospects of Nanoparticle-DNA Binding and its Implications in Medical Biotechnology. *Biotechnol Adv*, 30(6):1721–1732, 2012. doi: 10.1016/j.biotechadv.2012.03.007.

[35] M. O. Aviles, H. Chen, A. D. Ebner, A. J. Rosengart, M. D. Kaminski, and J. A. Ritter. In Vitro Study of Ferromagnetic Stents for Implant Assisted-Magnetic Drug Targeting. *J Magn Magn Mater*, 311:306–311, 2007.

[36] H. Chen, A. D. Ebner, A. J. Rosengart, M. D. Kaminski, and R. J. A. Analysis of Magnetic Drug Carrier Particle Capture by a Magnetizable Intravascular Stent: 1. Parametric Study with Single Wire Correlation. *J Magn Magn Mater*, 284(0):181–194, 2004. ISSN 0304-8853. doi: 10.1016/j.jmmm.2004.06.036.

[37] H. Chen, A. D. Ebner, A. J. Rosengart, M. D. Kaminski, and R. J. A. Analysis of Magnetic Drug Carrier Particle Capture by a Magnetizable Intravascular Stent: 2. Parametric Study with Multi-Wire Two-Dimensional Model. *J Magn Magn Mater*, 293(1):616–632, 2005. ISSN 0304-8853. doi: 10.1016/j.jmmm.2005.01.080.

[38] M. Chorny, I. Fishbein, B. B. Yellen, I. S. Alferiev, M. Bakay, S. Ganta, R. Adamo, M. Amiji, G. Friedman, and R. J. Levy. Targeting Stents with Local Delivery of Paclitaxel-Loaded Magnetic Nanoparticles Using Uniform Fields. *Proc Natl Acad Sci USA*, 107(18):8346–8351, 2010. doi: 10.1073/pnas.0909506107.

[39] B. Gleich, N. Hellwig, H. Bridell, R. Jurgons, C. Seliger, C. Alexiou, B. Wolf, and T. Weyh. Design and Evaluation of Magnetic Fields for Nanoparticle Drug Targeting in Cancer. *IEEE T Nanotechnol*, 6(2):164–170, 2007. doi: 10.1109/TNANO.2007.891829.

[40] A. Grief and G. Richardson. Mathematical Modeling of Magnetically Targeted Drug Delivery. *J Magn Magn Mater*, 293:455–463, 2005. doi: 10.1016/j.jmmm.2005.02.040.

[41] U. Albrechtsson, G. A. Hansson, and T. Olin. Vascular Occlusion with a Ferromagnetic Particle Suspension. An Experimental Investigation in Rabbits. *Acta Radiol Diagn*, 18(3):279–291, 1977.

[42] H. L. Liu, M. Y. Hua, H. W. Yang, C. Y. Huang, P. C. Chu, J. S. Wu., I. C. Tseng, J. J. Wang, T. C. Y. P. Y., Chen, and K. C. Wei. Magnetic Resonance Monitoring of Focused Ultrasound / Magnetic Nanoparticle Targeting Delivery of Therapeutic Agents to the Brain. *Proc. Natl. Acad. Sci. U. S. A.*, 107:15205–15210, 2010.

[43] A. Radomski, P. Jurasz, D. Alonso-Escolano, M. Drews, M. Morandi, T. Malinski, and M. W. Radomski. Nanoparticle-Induced Platelet Aggregation and Vascular Thrombosis. *Brit J Pharm*, 146(6):882–893, 2005. doi: 10.1038/sj.bjp.0706386.

[44] M. Mahmoudi, K. Azadmanesh, M. A. Shokrgozar, W. S. Journeay, and S. Laurent. Effect of Nanoparticles on the Cell Life Cycle. *Chem Rev*, 111(5):3407–3432, 2011. doi: 10.1021/cr1003166.

[45] M. Mahmoudi, A. Simchi, M. Imani, M. A. Shokrgozar, A. S. Milani, U. O. Häfeli, and P. Stroeve. A New Approach for the *in Vitro* Identification of the Cytotoxicity of Superparamagnetic Iron Oxide Nanoparticles. *Colloid Surfaces B*, 75(1):300–309, 2010. doi: 10.1016/j.colsurfb.2009.08.044.

[46] A. Garcia, R. Espinosa, L. Delgado, E. Casals, E. Gonzalez, V. Puntes, C. Barata, X. Font, and A. Sanchez. Acute Toxicity of Cerium Oxide, Titanium Oxide and Iron Oxide Nanoparticles Using Standardized Tests. *Desalination*, 269(1-3):136–141, 2011. doi: 10.1016/j.desal.2010.10.052.

[47] R. Weissleder, D. D. Stark, B. L. Engelstad, B. R. Bacon, C. C. Compton, D. L. White, P. Jacobs, and J. Lewis. Superparamagnetic Iron Oxide: Pharmacokinetics and Toxicity. *Am J Roentgenol*, 152:167–173, 1989.

[48] M. Levy, N. Luciani, D. Alloyeau, D. Elgrabli, V. Deveaux, C. Pechoux, S. Chat, G. Wang, N. Vats, F. Gendron, C. Factor, S. Lotersztajn, A. Luciani, C. Wilhelm, and F. Gazeau. Long Term *in Vivo* Biotransformation of Iron Oxide Nanoparticles. *Biomaterials*, 32(16):3988–3999, 2011. doi: 10.1016/j.biomaterials.2011.02.031.

[49] A. Nacev, C. Beni, O. Bruno, and B. Shapiro. Magnetic Nanoparticle Transport within Flowing Blood and into Surrounding Tissue. *Nanomedicine*, 5(9):1459–1466, 2010. doi: 10.2217/nnm.10.104.

[50] A. Nacev, C. Beni, O. Bruno, and B. Shapiro. The Behaviors of Ferromagnetic Nanoparticles in and around Blood Vessels under Applied Magnetic Fields. *J Magn Magn Mater*, 323(6):651–668, 2011. doi: 10.1016/j.jmmm.2010.09.008.

[51] C. Alexiou, R. Tietze, E. Schreiber, R. Jurgons, H. Richter, L. Trahms, H. Rahn, S. Odenbach, and S. Lyer. Cancer Therapy with Drug Loaded Magnetic Nanoparticles – Magnetic Drug Targeting. *J Magn Magn Mater*, 323:1404–1407, 2011. doi: 10.1016/j.jmmm.2010.11.059.

[52] K. Gitter and S. Odenbach. Experimental Investigations on a Branched Tube Model in Magnetic Drug Targeting. *J Magn Magn Mater*, 2010. doi: 10.1016/j.jmmm.2010.11.061.

[53] E. J.Furlani and E. P. Furlani. A Model for Predicting Magnetic Targeting of Multifunctional Particles in the Microvasculature. *J Magn Magn Mater*, 312 (1):187–193, 2007. doi: 10.1016/j.jmmm.2006.09.026.

[54] A. E. David, A. J. Cole, B. Chertok, Y. S. Park, and V. C. Yang. A Combined Theoretical and *in Vitro* Modeling Approach for Predicting the Magnetic Capture and Retention of Magnetic Nanoparticles *in Vivo*. *J Controll Release*, 152, 2011. doi: 10.1016/j.jconrel.2011.01.033.

[55] E. M. Cherry, P. G. Maxim, and J. K. Eaton. Particle Size, Magnetic Field, and Blood Velocity Effects on Particle Retention in Magnetic Drug Targeting. *Med Phys*, 37(1):175–182, 2010.

[56] M. Zborowski and J. Chalmers. *Magnetic Cell Separation*. Elsevier, 2007. ISBN 9780444527547.

[57] O. Mykhaylyk, T. Sobisch, I. Almstätter, Y. Sanchez-Antequera, S. Brandt, M. Anton, M. Döblinger, D. Eberbeck, M. Settles, R. Braren, D. Lerche, and C. Plank. Silica-Iron Magnetic Nanoparticles Modified for Gene Delivery; A Search for Optimum and Quantitative Criteria. *Pharm Res*, 29:1344–1365, 2012. doi: 10.1007/s11095-011-0661-9.

[58] D. A. Bazylinski, C. T. Lefevre, and D. Schüler. Magnetotactic Bacteria. In E. Rosenberg, E. F. De Long, S. Lory, E. Stackebrandt, and F. Thompson, editors, *The Prokaryotes*, pages 453–494. Springer Berlin Heidelberg, 2013. ISBN 9783642301407. doi: 10.1007/978-3-642-30141-474.

[59] J. Sun, M. Guan, T. Shang, C. Gao, Z. Xu, and J. Zhu. Selective Synthesis of Gold Cuboid and Decahedral Nanoparticles Regulated and Controlled by Cu2+ Ions. *Cryst Growth Des*, 8(3):906–910, 2008. doi: 10.1021/cg070635a.

[60] J. E. Smith and M. L. Jordan. Mathematical and Graphical Interpretation of the Log-Normal Law for Particle Size Distribution Analysis. *J Coll Sci Imp U Tok*, 19(6):549–559, 1964. doi: 10.1016/0095-8522(64)90069-8.

[61] J. Heintzenberg. Properties of the Log-Normal Particle Size Distribution. *Aerosol Sci Tech*, 21(1):46–48, 1994. doi: 10.1080/02786829408959695.

[62] *Dynamic Light Scattering: An Introduction in 30 Minutes*. Zetasizer Nano Series Technical Note, .

[63] V. Maurice, T. Georgelin, J.-M. Siaugue, and V. Cabuil. Synthesis and Characterization of Functionalized Core-Shell γFe_2O_3-SiO_2 Nanoparticles. *J Magn Magn Mater*, 321(10):1408–1413, 2009. doi: 10.1016/j.jmmm.2009.02.051.

[64] U. O. Haefeli, M. Lobedann, J. Steingroewer, L. Moore, and J. Riffle. Optical Method for Measurement of Magnetophoretic Mobility of Individual Magnetic Microspheres in Defined Magnetic Field. *J Magn Magn Mater*, 293:224–239, 2005. doi: 10.1016/j.jmmm.2005.02.001.

[65] J. J. Chalmers, Y. Zhao, M. Nakamura, K. Melnik, L. Lasky, L. Moore, and M. Zborowski. An Instrument to Determine the Magnetophoretic Mobility of Labeled, Biological Cells and Paramagnetic Particles. *J Magn Magn Mater*, 194:231–241, 1999. doi: 10.1016/S0304-8853(98)00557-5.

[66] M. Godin, A. K. Bryan, T. P. Burg, K. Babcock, and S. R. Manalis. Measuring the Mass, Density, and Size of Particles and Cells Using a Suspended Microchannel Resonator. *Appl Phys Lett*, 91:3121, 2007. doi: 10.1063/1.2789694.

[67] A. K. Bryan, A. Goranov, A. Amon, and S. R. Manalis. Measurement of Mass, Density, and Volume during the Cell Cycle of Yeast. *Proc Natl Acad Sci USA*, 107(3):999–1004, 2010. doi: 10.1073/pnas.0901851107.

[68] W. H. Grover, A. K. Bryan, M. Diez-Silva, S. Suresh, J. M. Higgins, and S. R. Manalis. Measuring Single-Cell Density. *Proc Natl Acad Sci USA*, 108(27): 10992–10996, 2011. doi: 10.1073/pnas.1104651108.

[69] *Zeta Potential: An Introduction in 30 Minutes*. Zetasizer Nano Series Technical Note, .

[70] V. Kose and F. Melchert. *Quantenmasse in der Elektrischen Messtechnik: Josephson-Effekt, Quanten-Hall-Effekt, Fundamentalkonstanten, Masse der klassischen Physik*. VCH, Weinheim, 1991. ISBN 3527283803.

[71] J.-W. Park, I. S. Yoo, W.-S. Chang, E.-C. Lee, H. Ju, B. H. Chung, and B. S. Kim. Magnetic Moment Measurement of Magnetic Nanoparticles using Atomic Force Microscopy. *Meas Sci Technol*, 19:7005, 2008. doi: 10.1088/0957-0233/19/1/017005.

[72] A. Saunderson. A Permanent Magnet Gouy Balance. *Physics Education*, 3(5): 272, 1968. doi: 10.1088/0031-9120/3/5/007.

[73] B. L. Morris and A. Wold. Faraday Balance for Measuring Magnetic Susceptibility. *Rev Sci Instrum*, 39(12):1937–1941, 1968. doi: 10.1063/1.1683276.

[74] T. Weyh. Nanomagnetische Arzneistoffträger und eine integrierte Technologie für die therapeutische Anwendung: Teilvorhaben: Zell-Transfektion, Targeting und Positionierung von Nanopartikelmarkierten Wirkstoffen durch statische und dynamische Magnetfelder. Schlussbericht BMBF Förderkennzeichen 13N9184, Technische Universität München, 2011.

[75] H. L. de Barros and D. Acosta-Avalos. A Simple Method to Estimate the Magnetic Moment of Magnetic Micro-Particles. *J Magn Magn Mater*, 320(14): 215, 2008. doi: 10.1016/j.jmmm.2008.02.144.

[76] O. Mykhaylyk, O. Zelphati, J. Rosenecker, and C. Plank. siRNA Delivery by Magnetofection. *Curr Opin Mol Ther*, 10(5):493, 2008.

[77] O. Mykhaylyk, A. Steingotter, H. Perea, J. Aigner, R. Botnar, and C. Plank. Nucleic acid delivery to magnetically-labeled cells in a 2d array and at the luminal surface of cell culture tube and their detection by mri. *J Biomed Nanotechnol*, 5(6):692–706, 2009.

[78] V. R. S. Patil, C. J. Campbell, Y. H. Yun, S. M. Slack, and D. J. Goetz. Particle Diameter Influences Adhesion under Flow. *Biophys J*, 80(4):1733–1743, 2001. doi: 10.1016/S0006-3495(01)76144-9.

[79] J. D. Jackson. *Klassische Elektrodynamik*. De Gruyter, Berlin, 1985. ISBN 3110095793.

[80] D. Eberbeck, F. Wiekhorst, U. Steinhoff, and L. Trahms. Messtechnik zur Qualitätssicherung magnetischer Nanoteilchen für Anwendungen in Medizin und Bioanalytik (QuaNTAMed) - SQUID-basierte Magnetorelaxometrie an magnetischen Nanopartikeln als Referenzmethode für die Fluxgate-MRX. Schlussbericht BMBF Förderkennzeichen 13N9149, Physikalisch-Technische Bundesanstalt, 2010.

[81] D. J. Acheson. *Elementary Fluid Dynamics (Oxford Applied Mathematics & Computing Science Series)*. Oxford University Press, USA, 1990. ISBN 0198596790.

[82] H. Stöcker. *Taschenbuch der Physik*. Harri Deutsch, 2000. ISBN 3817116276.

[83] K. T. Trinh. On The Critical Reynolds Number For Transition From Laminar To Turbulent Flow. 2010.

[84] S. S. Shibeshi and E. W. Collins. The Rheology of Blood Flow in a Branched Arterial System. *Appl Rheol*, 6:398–405, 2005.

[85] I. M. Cohen and P. K. Kundu. *Fluid Mechanics, Fourth Edition*. Academic Press, 2007. ISBN 0123737354.

[86] W. Ostwald. Üeber die Rechnerische Darstellung des Strukturgebietes der Viskosität. *Kolloid Z*, 47(2):176–187, 1929. doi: 10.1007/BF01496959.

[87] R. B. Bird and P. J. Carreau. A Nonlinear Viscoelastic Model for Polymer Solutions and Melts-I. *Chem Eng Sci*, 23(5):427–434, 1968. doi: 10.1016/0009-2509(68)87018-6.

[88] K. Yasuda, R. C. Armstrong, and R. E. Cohen. Shear Flow Properties of Concentrated Solutions of Linear and Star Branched Polystyrenes. *Rhel Acta*, 20:163–178, 1981. doi: 10.1007/BF01513059.

[89] S. P. Williams, F. Carpino, and M. Zborowski. Magnetic Nanoparticle Drug Carriers and Their Study by Quadrupole Magnetic Field-Flow Fractionation. *Mol Pharm*, 6(5):1290–1306, 2009. doi: 10.1021/mp900018v.

[90] P. A. Voltairas, D. I. Fotiadis, and L. K. Michalis. Hydrodynamics of Magnetic Drug Targeting. *J Biomech*, 35:813–821, 2002.

[91] G. P. Saffman. The Lift on a Small Sphere in a Slow Shear Flow. *J Fluid Mech*, 22(02):385–400, 1965. doi: 10.1017/S0022112065000824.

[92] J. B. McLaughlin. Inertial Migration of a Small Sphere in Linear Shear Flows. *J Fluid Mech*, 224:261–274, 1991. doi: 10.1017/S0022112091001751.

[93] P. Cherukat. A Computational Study of the Inertial Lift on a Sphere in a Linear Shear Flow Field. *Int J Multiphas Flow*, 25(1):15–33, 1999. doi: 10.1016/S0301-9322(98)00034-2.

[94] R. Kurose, R. Misumi, and S. Komori. Drag and Lift Forces Acting on a Spherical Bubble in a Linear Shear Flow. *Int J Multiphas Flow*, 27(7):1247–1258, 2001. doi: 10.1016/S0301-9322(00)00073-2.

[95] A. Einstein. Über die von der Molekularkinetischen Theorie der Wärme geforderte Bewegung von in Ruhenden Flüssigkeiten Suspendierten Teilchen. *Ann Phys*, 517:182–193, 2005. doi: 10.1002/andp.200590005.

[96] P. C. Hiemenz and R. Rajagopalan. *Principles of Colloid and Surface Chemistry*. Dekker, New York, 1987. ISBN 0824793978.

[97] D.-X. Chen, G. via, F.-J. Xu, C. Navau, A. Sanchez, H.-C. Gu, J. S. Andreu, C. Calero, J. Camacho, and J. Faraudo. Waiting Time Dependence on T2 of Protons in Water Suspensions of Iron-Oxide Nanoparticles: Measurements and Simulations. *J Appl Phys*, 110:3917, 2011. doi: 10.1063/1.3646457.

[98] E. P. Furlani. *Permanent Magnet and Electromechanical Devices: Materials, Analysis, and Applications (Electromagnetism)*. Academic Press, 2001. ISBN 0122699513.

[99] D. Grasso, K. Subramaniam, M. Butkus, K. Strevett, and J. Bergendahl. A review of Non-DLVO Interactions in Environmental Colloidal Systems. *Rev Env Sci Biotechnol*, 1(1):17–38, 2002. doi: 10.1023/A:1015146710500.

[100] H. H. M. Rijnaarts, W. Norde, J. Lyklema, and A. J. B. Zehnder. DLVO and Steric Contributions to Bacterial Deposition in Media of Different Ionic Strengths. *Colloid Surface B*, 14(1):179–195, 1999. doi: 0.1016/S0927-7765(99)00035-1.

[101] B. Derjaguin and L. Landau. Theory of the Stability of Strongly Charged Lyophobic Sols and of the Adhesion of Strongly Charged Particles in Solutions of Electrolytes. *AP URSS*, 14, 1941.

[102] R. J. Hunter. *Foundations of Colloid Science*. Oxford Univ Press, 2001. ISBN 0198505027.

[103] J. N. Israelachvili. *Intermolecular and Surface Forces.* Academic Press, 2003. ISBN 9780123919274.

[104] H. C. van de Hulst. *Light Scattering by Small Particles.* Dover Publications, New York, 1981. ISBN 0-486-64228-3.

[105] M. Born and E. Wolf. *Principles of Optics: Electromagnetic Theory of Propagation, Interference and Diffraction of Light.* Cambridge Univ Pr, 2006. ISBN 9780521642224.

[106] C. F. Bohren and D. R. Huffman. *Absorption and Scattering of Light by Small Particles.* Wiley-VCH, Weinheim, Germany, 2004. ISBN 9780471293408.

[107] S. Hipp. *Electromagnetic Drop Scale Scattering Modelling for Dynamic Statistical Rain Fields.* PhD thesis, Technische Universität München, 2013. and personal communications.

[108] K. Halbach. Design of Permanent Multipole Magnets with Oriented Rare Earth Cobalt Material. *Nucl Instrum Methods*, 169(1):1, 1980. doi: 10.1016/0029-554X(80)90094-4.

[109] C. Kilgus, A. Heidsieck, A. Ottersbach, W. Roell, C. Trueck, B. K. Fleischmann, B. Gleich, and P. Sasse. Local Gene Targeting and Cell Positioning Using Magnetic Nanoparticles and Magnetic Tips: Comparison of Mathematical Simulations with Experiments. *Pharm Res*, 29:1380–1391, 2012. doi: 10.1007/s11095-011-0647-7.

[110] D. S. Burnett. *Finite Element Analysis: From Concepts to Applications.* Addison-Wesley Pub. Co, Reading, Mass, 1987. ISBN 0-201-10806-2.

[111] G. L. Trigg. *Mathematical Tools for Physicists.* Wiley-VCH, 2005. ISBN 3527405488.

[112] E. F. D'Azevedo. Are Bilinear Quadrilaterals Better Than Linear Triangles? *SIAM J Sci Comput*, 22:198–217, 2000. doi: 10.1137/S106482759630406X.

[113] C. Reinsch. Smoothing by Spline Functions. *Numer Math*, 10:177–183, 1967. doi: 10.1007/BF02162161.

[114] D. Garcia. Robust Smoothing of Gridded Data in One and Higher Dimensions with Missing Values. *Comput Stat Data An*, 54(4):1167–1178, 2010.

[115] D. Garcia. Fast and Robust Smoothing of One-Dimensional and Multidimensional Data. `http://www.biomecardio.com/matlab/smoothn.html`.

[116] M. E. Hosea and L. F. Shampine. Analysis and Implementation of TR-BDF2. *Applied Numerical Mathematics*, 20(1):21–37, 1996. doi: 10.1016/0168-9274(95)00115-8.

[117] M. Matsumoto and T. Nishimura. Mersenne Twister: A 623-Dimensionally Equidistributed Uniform Pseudo-Random Number Generator. *ACM Trans Model Comput Simul*, 8:3–30, 1998. doi: 10.1145/272991.272995.

[118] G. D'Agostini. *Bayesian Reasoning in High-Energy Physics: Principles and Applications*. CERN, Geneva, 1999. ISBN 9290831456.

[119] B. Efron. Bootstrap Methods: Another Look at the Jackknife. *Ann Math Stat*, 7(1):1–26, 1979. doi: 10.1214/aos/1176344552.

[120] O. Mykhaylyk, Y. S. Antequera, D. Vlaskou, and C. Plank. Generation of Magnetic Nonviral Gene Transfer Agents and Magnetofection *in Vitro*. *Nat Protocols*, pages 2391–2411, 2007. doi: 10.1038/nprot.2007.352.

[121] R. M. Cornell and U. Schwertmann. *The Iron Oxides*. VCH Publishing Group, 1996. ISBN 3527285768.

[122] E. Meijering, O. Dzyubachyk, and I. Smal. Methods for Cell and Particle Tracking. In *Imaging and Spectroscopic Analysis of Living Cells*, volume 504 of *Methods in Enzymology*, chapter 9, pages 183–200. Elsevier/Academic Press, 2012. ISBN 9780123918574.

[123] K. Jaqaman, D. Loerke, M. Mettlen, H. Kuwata, S. Grinstein, S. L. Schmid, and G. Danuser. Robust Single-Particle Tracking in Live-Cell Time-Lapse Sequences. *Nat Meth*, 5:695–702, 2008. doi: 10.1038/nmeth.1237.

[124] J. Huth, M. Buchholz, J. M. Kraus, K. Molhave, C. Gradinaru, G. v Wichert, T. M. Gress, H. Neumann, and H. A. Kestler. TimeLapseAnalyzer: Multi-target Analysis for Live-Cell Imaging and Time-Lapse Microscopy. *Comput Meth Prog Bio*, 104(2):227–234, 2011. doi: 10.1016/j.cmpb.2011.06.002.

[125] M. Leocmach and H. Tanaka. A Novel Particle Tracking Method with individual Particle Size Measurement and its Application to Ordering in Glassy Hard Sphere Colloids. *Soft Matter*, 9(5):1447–1457, 2013. doi: 10.1209/0295-5075/89/38006.

[126] O. Dzyubachyk, W. A. van Cappellen, J. Essers, W. J. Niessen, and E. Meijering. Advanced level-set-based cell tracking in time-lapse fluorescence microscopy. *IEEE T Med Imaging*, 29(3):852–867, 2010. doi: 10.1109/TMI.2009.2038693.

[127] J. C. Crocker and D. G. Grier. Methods of Digital Video Microscopy for Colloidal Studies. *J Colloid Interface Sci*, 179, 1996.

[128] J. C. Crocker and E. R. Weeks. Particle Tracking Using IDL, 1996. `http://www.physics.emory.edu/~weeks/idl/`.

[129] D. Blair and E. Dufresne. Matlab Particle Tracking Code. `http://physics.georgetown.edu/matlab/`.

[130] E. Davies. *Machine Vision: Theory, Algorithms, Practicalities*. Academic Press, London, 1997. ISBN 012206092X.

[131] T. H. Cormen, C. E. Leiserson, and R. L. Rivest. *Introduction to Algorithms*. MIT Press, Cambridge Mass, 2001. ISBN 0262032937.

[132] G. T. Heineman, G. Pollice, and S. Selkow. *Algorithms in a Nutshell*. O'Reilly, 2009. ISBN 9780596-51624-6.

[133] W. H. Press, S. A. Teukolsky, W. T. Vetterling, and B. P. Flannery. *Numerical Recipes: the Art of Scientific Computing*. Cambridge University Press, Cambridge, UK, 2007. ISBN 0521880688.

[134] S. H. Maron, P. E. Pierce, and I. N. Ulevitch. Determination of Latex Particle Size by Light Scattering. IV. Transmission Measurements. *J Colloid Sci*, 18(5): 470–482, 1963. doi: 10.1016/0095-8522(63)90039-4.

[135] G. Mie. Beiträge zur Optik Trüber Medien, Speziell Kolloidaler Metallösungen. *Ann Phys*, 330:377–445, 1969. doi: 10.1002/andp.19083300302.

[136] J. M. Perez, L. Josephson, T. O'Loughlin, D. Högemann, and R. Weissleder. Magnetic Relaxation Switches Capable of Sensing Molecular Interactions. *Nat Biotechnol*, 20(8):816–820, 2002.

[137] A. Roch, Y. Gossuin, R. N. Muller, and P. Gillis. Superparamagnetic Colloid Suspensions: Water Magnetic Relaxation and Clustering. *J Magn Magn Mater*, 293(1):532–539, 2005. doi: 10.1016/j.jmmm.2005.01.070.

[138] Q. L. Vuong, P. Gillis, and Y. Gossuin. Monte Carlo Simulation and Theory of Proton NMR Transverse Relaxation Induced by Aggregation of Magnetic Particles Used as MRI Contrast Agents. *J Magn Reson*, 212(1):139–148, 2011. doi: 10.1016/j.jmr.2011.06.024.

[139] C. Wilhelm, F. Gazeau, and J.-C. Bacri. Magnetophoresis and Ferromagnetic Resonance of Magnetically Labeled Cells. *Eur Biophys J*, 31(2):118–125, 2002. doi: 10.1007/s00249-001-0200-4.

[140] C. Rablau, P. Vaishnava, C. Sudakar, R. Tackett, G. Lawes, and R. Naik. Nanoparticle Aggregation and Relaxation Effects in Ferrofluids: Studied through Anisotropic Light Scattering. In *NanoScience Engineering*, pages 70320Z–70320Z. International Society for Optics and Photonics, 2008. doi: 10.1117/12.791987.

[141] M. J. Berg, C. M. Sorensen, and A. Chakrabarti. Extinction and the Optical Theorem. Part I. Single Particles. *J Opt Soc Am A*, 25(7):1504–1513, 2008. doi: 10.1364/JOSAA.25.001504.

[142] M. J. Berg, C. M. Sorensen, and A. Chakrabarti. Extinction and the Optical Theorem. Part II. Multiple Particles. *J Opt Soc Am A*, 25(7):1514–1520, 2008. doi: 10.1364/JOSAA.25.001514.

[143] M. I. Mishchenko, L. Liu, D. W. Mackowski, B. Cairns, and G. Videen. Multiple Scattering by Random Particulate Media: Exact 3D Results. *Opt Express*, 15(6):2822–2836, 2007. doi: 10.1364/OE.15.002822.

[144] E. Setijadi, A. Matsushima, N. Tanaka, and G. Hendrantoro. Effect of Temperature and Multiple Scattering on Rain Attenuation of Electromagnetic Waves by a Simple Spherical Model. *Prog Electromagn Res*, 99:339–354, 2009. doi: 10.2528/PIER09102609.

[145] R. Brunelli. *Template Matching in Computer Vision: Theory and Practice*. Wiley-Blackwell, Oxford, 2009. ISBN 978-0-470-51706-2.

[146] L. Vincent and P. Soille. Watersheds in Digital Spaces: An Efficient Algorithm Based on Immersion Simulations. *IEEE T Pattern Anal*, 13(6):583–598, 1991. doi: 10.1109/34.87344.

[147] J. B. Roerdink and A. Meijster. The Watershed Transform: Definitions, Algorithms and Parallelization Strategies. *Fund Inform*, 41(1):187–228, 2000. doi: 10.3233/FI-2000-411207.

[148] I. F. Sbalzarini and P. Koumoutsakos. Feature Point Tracking and Trajectory Analysis for Video Imaging in Cell Biology. *J Struct Biol*, 151(2):182–195, 2005. doi: 10.1016/j.jsb.2005.06.002.

[149] S. J. Baek and S. J. Lee. A New Two-Frame Particle Tracking Algorithm Using Match Probability. *Exp Fluids*, 22(1):23–32, 1996. doi: 10.1007/BF01893303.

[150] H.-T. Chen, H.-H. Lin, and T.-L. Liu. Multi-Object Tracking Using Dynamical Graph Matching. In *Proceedings of the 2001 IEEE Computer Society Conference on Computer Vision and Pattern Recognition*, volume 2, pages 210–217, 2001. doi: 10.1109/CVPR.2001.990962.

[151] M. Taj, E. Maggio, and A. Cavallaro. Multi-feature graph-based object tracking. In *Proceedings of the 1st international evaluation conference on Classification of events, activities and relationships*, CLEAR06, pages 190–199, 2007. ISBN 978-3-540-69567-7.

[152] A. S. Chowdhury, R. Chatterjee, M. Ghosh, and N. Ray. Cell Tracking in Video Microscopy Using Bipartite Graph Matching. In *20th International Conference on Pattern Recognition (ICPR)*, pages 2456–2459, 2010. doi: 10.1109/ICPR.2010.601.

[153] R. Adrian. Twenty Years of Particle Image Velocimetry. *Exp Fluids*, 39(2):159–169, 2005. ISSN 0723-4864. doi: 10.1007/s00348-005-0991-7.

[154] R. A. French, A. R. Jacobson, B. Kim, S. L. Isley, R. L. Penn, and P. C. Baveye. Influence of Ionic Strength, pH, and Cation Valence on Aggregation Kinetics of Titanium Dioxide Nanoparticles. *Environ Sci Technol*, 43(5):1354–1359, 2009. doi: 10.1021/es802628n.

[155] A. Levy, D. Andelman, and H. Orland. Dielectric Constant of Ionic Solutions: A Field-Theory Approach. *Phys Rev Lett*, 108:227801, 2012. doi: 10.1103/PhysRevLett.108.227801.

[156] X. Liu, M. Wazne, C. Christodoulatos, and K. L. Jasinkiewicz. Aggregation and Deposition Behavior of Boron Nanoparticles in Porous Media. *J Colloid Interf Sci*, 330(1):90–96, 2009. doi: 10.1016/j.jcis.2008.10.028.

[157] S. W. Bian, I. A. Mudunkotuwa, T. Rupasinghe, and V. H. Grassian. Aggregation and Dissolution of 4 nm ZnO Nanoparticles in Aqueous Environments: Influence of pH, Ionic Strength, Size, and Adsorption of Humic Acid. *Langmuir*, 27(10):6059–6068, 2011. doi: 10.1021/la200570n.

[158] W. Kunz, P. Lo Nostro, and B. W. Ninham. The Present State of Affairs with Hofmeister Effects. *Curr Opin Colloid In*, 9(1–2), 2004. doi: 10.1016/j.cocis.2004.05.004.

[159] V. Dahirel and M. Jardat. Effective Interactions Between Charged Nanoparticles in Water: What is Left From the DLVO Theory? *Curr Opin Colloid In*, 15(1–2):2–7, 2010. doi: 10.1016/j.cocis.2009.05.006.

[160] W. Kunz, J. Henle, and B. W. Ninham. Zur Lehre von der Wirkung der Salze (About the Science of the Effect of Salts): Franz Hofmeisters Historical Papers. *Curr Opin Colloid In*, 9(1–2):19–37, 2004. doi: 10.1016/j.cocis.2004.05.005.

[161] E. Leontidis. Hofmeister Anion Effects on Surfactant Self-Assembly and the Formation of Mesoporous Solids. *Curr Opin Colloid In*, 7(1–2):81–91, 2002. doi: 10.1016/S1359-0294(02)00010-9.

[162] J. Lyklema. Simple Hofmeister series. *Chem Phys Lett*, 467(4):217–222, 2009. doi: 10.1016/j.cplett.2008.11.013.

[163] N. Schwierz, D. Horinek, and R. R. Netz. Reversed Anionic Hofmeister Series: the Interplay of Surface Charge and Surface Polarity. *Langmuir*, 26(10):7370–7379, 2010. doi: 10.1021/la904397v.

[164] A. Heidsieck, S. Vosen, K. Zimmermann, D. Wenzel, and B. Gleich. Analysis of Trajectories for Targeting of Magnetic Nanoparticles in Blood Vessels. *Mol Pharm*, 9(7):2029–2038, 2012. doi: 10.1021/mp3001155.

[165] A. Hofmann, D. Wenzel, U. M. Becher, D. F. Freitag, A. M. Klein, D. Eberbeck, M. Schulte, K. Zimmermann, C. Bergemann, B. Gleich, and et al. Combined Targeting of Lentiviral Vectors and Positioning of Transduced Cells by Magnetic Nanoparticles. *Proc Natl Acad Sci USA*, 106(1):44–49, 2009.

[166] D. Wenzel, S. Rieck, S. Vosen, O. Mykhaylyk, C. Trueck, D. Eberbeck, L. Trahms, K. Zimmermann, A. Pfeifer, and B. K. Fleischmann. Identification of Magnetic Nanoparticles for Combined Positioning and Lentiviral Transduction of Endothelial Cells. *Pharm Res*, 29:1242–1254, 2012. doi: 10.1007/s11095-011-0657-5.

[167] J. Riegler, J. A. Wells, P. G. Kyrtatos, A. N. Price, Q. A. Pankhurst, and M. F. Lythgoe. Targeted Magnetic Delivery and Tracking of Cells Using a Magnetic Resonance Imaging System. *Biomaterials*, 31(20):5366–5371, 2010. doi: 10.1016/j.biomaterials.2010.03.032.

[168] M. Arsianti, M. Lim, C. P. Marquis, and R. Amal. Polyethylenimine Based Magnetic Iron-Oxide Vector: The Effect of Vector Component Assembly on Cellular Entry Mechanism, Intracellular Localization, and Cellular Viability. *Biomacromolecules*, 11(9):2521–2531, 2010. doi: 10.1021/bm100748p.

[169] C. Trueck, K. Zimmermann, O. Mykhaylyk, M. Anton, S. Vosen, D. Wenzel, B. K. Fleischmann, and A. Pfeifer. Optimization of Magnetic Nanoparticle-Assisted Lentiviral Gene Transfer. *Pharm Res*, 29(5):1255–1269, 2012. doi: 10.1007/s11095-011-0660-x.

[170] U. O. Häfeli, J. S. Riffle, L. Harris-Shekhawat, A. Carmichael-Baranauskas, F. Mark, J. P. Dailey, and D. Bardenstein. Cell Uptake and in Vitro Toxicity of Magnetic Nanoparticles Suitable for Drug Delivery. *Molecular pharmaceutics*, 6(5):1417–1428, 2009. doi: 10.1021/mp900083m.

[171] C. Perez-Rojas. Fitting Saturation and Hysteresis via Arctangent Functions. *IEEE Power Eng Rev*, 20(11):55–57, 2000. doi: 10.1109/39.883282.

[172] P. V. Hlinomaz. *Study of Multi-Modal and Non-Gaussian Probability Density Functions in Target Tracking with Applications to Dim Target Tracking.* PhD thesis, Wright State University, 2008.

List of Publications

Peer-Reviewed Articles

- D. Vlaskou, O. Mykhaylyk, F. Krötz, N. Hellwig, R. Renner, U. Schillinger, B. Gleich, **A. Heidsieck**, G. Schmitz, K. Hensel and C. Plank, *Magnetic and Acoustically Active Lipospheres for Magnetically Targeted Nucleic Acid Delivery*, Advanced Functional Materials 20(22):3881–3894, 2010
- C. Kilgus*, **A. Heidsieck***, A. Ottersbach, W. Röll, C. Trück, B. Fleischmann, B. Gleich and P. Sasse, *Local Gene Targeting and Cell Positioning Using Magnetic Nanoparticles and Magnetic Tips: Comparison of Mathematical Simulations with Experiments*, Pharmaceutical Research 29(5):1380–1391, 2011
- G. Hasenpusch, J. Geiger, K. Wagner, O. Mykhaylyk, F. Wiekhorst, L. Trahms, **A. Heidsieck**, B. Gleich, C. Bergemann, M. K. Aneja and C. Rudolph, *Magnetized Aerosols Comprising Superparamagnetic Iron Oxide Nanoparticles Improve Targeted Drug and Gene Delivery to the Lung*, Pharmaceutical Research 29(5):1308–1318, 2012
- **A. Heidsieck**, S. Vosen, K. Zimmermann, D. Wenzel, B. Gleich, *Analysis of Trajectories for Targeting of Magnetic Nanoparticles in Blood Vessels*, Molecular Pharmaceutics 9(7):2029–2038, 2012

Articles in Preparation

- S. Vosen, S. Rieck, **A. Heidsieck**, K. Zimmermann, O. Mykhaylyk, C. Plank, A. Pfeifer, B. Gleich, B. Fleischmann and D. Wenzel, *Improvement of Vascular Function by Magnetic Nanoparticle-Assisted Gene and Endothelial Cell Transfer in Vessels*
- **A. Heidsieck**, A. Joos, C. Rümenapp and B. Gleich, *The Influence of Physiological Buffer Solutions on the Aggregation of Iron Oxide Nanoparticles*
- **A. Heidsieck**, A. Ottersbach, Y. Stampnik, D. Eberbeck, W. Röll, B. Fleischmann, H. Mannell and B. Gleich, *Optical Tracking of Magnetic Carriers for the Measurement of the Magnetic Moment*

*contributed equally

Conference Proceedings

- **A. Rüger** and B. Gleich, *Magnetic Field Design for efficient 3D-targeting of MNP Complexes*, IFMBE Proceedings, World Congress on Medical Physics and Biomedical Engineering 2009, 2010
- **A. Heidsieck** and B. Gleich, *Analysis of Particle Trajectories for Magnetic Drug Targeting*, Comsol Conference 2010 Paris, 2010

Acknowledgments

This work is in parts based on the publications Kilgus *et al* [109] and Heidsieck *et al* [164]. Also partly included are works accomplished by the students Alexander Joos and Daniel Schmid in the course of their diploma and bachelor thesis, respectively. The latter was supervised by Norbert Gattinger.

I would like to thank all those who have supported, helped, and contributed along the way:

- Bernhard Gleich for his support as a mentor and advisor, the discussions, his scientific stimulations; also for proof-reading this work and feeding all of us with barbecue and ice cream;
- Thorsten Hugel for agreeing to supervise this work and the examination board for their effort and time
- my colleagues at the institute and all the various students who worked in our group over the time; foremost Norbert Gattinger, Christine Rümenapp and Thomas Gaaß for assisting with biological, chemical, electronic, mathematical and all other problems and who have made my time at the institute very enjoyable;
- my colleagues of the DFG unit for the very friendly and fruitful collaboration and the arising results which contributed to this work, especially
  - Olga Mykhaylyk for providing nanoparticles
  - Hanna Mannell and Yvonn Stampnik for providing and preparing microbubbles
  - Wilhelm Röll and Annika Ottersbach for providing and preparing the different cell types
  - Philipp Sasse and Carsten Kilgus for the collaboration on the static model of the magnetic tips
  - Daniela Wenzel and Sarah Vosen for the collaboration on the dynamic arterial model

- Marianne Hanzlik of the Department of Chemistry for providing electron microscopy images of particles
- Andreas Bauer and Michael Stanger of the Physics Department for magnetization measurements and the manufacturing of the corresponding glass tubes
- my former fellow student and friend Susanne Hipp for her assistance with her particular subject
- my mother in law for harboring me and offering a quiet workplace
- and most of all my husband, for many topic related discussions, proof-reading this work, his support and patience as well as providing the hot beverage of choice and simply just being who he is.